UNIVERSITY OF CALIFORNIA
RIVERSIDE

A New GalWeight-Derived SDSS Galaxy Cluster Catalog and Cosmological Constraints on Ω_m and σ_8

A Dissertation submitted in partial satisfaction
of the requirements for the degree of

Doctor of Philosophy

in

Physics

by

Mohamed H El Hashash

December 2020

Dissertation Committee:

Prof. Gillian Wilson, Chairperson
Prof. Brian Siana
Prof. George Becker

The Dissertation of Mohamed H El Hashash is approved:

Committee Chairperson

University of California, Riverside

Acknowledgments

Foremost, I would like to thank Allah (God) for His grace and support, then many thanks to my parents and wife for their encouragement, assistant, and support. I would like to express my sincere gratitude to my advisor Prof. Gillian Wilson for her continuous support of my Ph.D. study and research, her patience, motivation, enthusiasm, and immense knowledge.

I would like to thank my committee members, Prof. Brian Siana and Prof. George Becker for their encouragement, useful discussion and insightful comments. I owe my deepest gratitude to the many people who have contributed to making this scientific work. My great sincere thanks are for Prof. Anatoly Klypin, Prof. Elizabeth Praton, Prof. Laura Sales, and Dr. Lyndsay Old. I also would like to thank Prof. Gary Mamon, Prof. Stefano Andreon and Dr. Steven Murray for their useful discussions and comments.

Special thanks are for my former advisor, Prof. Gamal Ali (Astronomy Dept., NRIAG, Egypt), how passed away three years ago, for his enthusiastic support and guidance, and for generously providing his time and ideas.

The dissertation contains three published/in press papers listed as follows.

1. Mohamed H. Abdullah[1], Anatoly Klypin, Gillian Wilson, 2020b , Cosmological Constraints on Ω_m and σ_8 from Cluster Abundances using the `GalWCat19` Optical-Spectroscopic SDSS Catalog, (accepted for publication in the ApJ in July 2020), Abdullah et al. (2020a)

2. Mohamed H. Abdullah, Gillian Wilson, Anatoly Klypin, Lyndsay Old, Elizabeth Praton, Gamal B. Ali, 2020a, GalWeight Application: A publicly-available catalog of dynamical parameters of 1800 galaxy clusters from SDSS-DR13, (GalWCat19), ApJS, 246, 2, Abdullah

[1] https://iopscience.iop.org/article/10.3847/1538-4357/aac5db)

et al. (2020b)

3. Mohamed H. Abdullah, Gillian Wilson, Anatoly Klypin, 2018, GalWeight: A New and Effective Weighting Technique for Determining Galaxy Cluster and Group Membership, ApJ, 861, 22, Abdullah et al. (2018)

To my parents, wife, and kids.

ABSTRACT OF THE DISSERTATION

A New GalWeight-Derived SDSS Galaxy Cluster Catalog and Cosmological Constraints on Ω_m and σ_8

by

Mohamed H El Hashash

Doctor of Philosophy, Graduate Program in Physics
University of California, Riverside, December 2020
Prof. Gillian Wilson, Chairperson

The dissertation includes three manuscripts. Firstly, we introduce the GalWeight technique, a new technique for assigning galaxy cluster membership. GalWeight is designed to simultaneously maximize the number of *bona fide* cluster members while minimizing the number of interlopers. GalWeight can be applied to both massive and poor galaxy groups and is effective in identifying members in both the virial and infall regions with high efficiency. We apply GalWeight to MDPL2 & Bolshoi N-body simulations, and find that it is $> 98\%$ accurate in correctly assigning cluster membership. We apply GalWeight to a sample of twelve Abell clusters using observations from the Sloan Digital Sky Survey.

Secondly, we apply GalWeight to the SDSS-DR13 spectroscopic data set to create a new publicly-available catalog of 1800 galaxy clusters (`GalWCat19`) and a corresponding catalog of 34471 identified member galaxies. The clusters are identified from overdensities in redshift-phase space. The cluster masses are calculated using the virial theorem and NFW model. The `GalWCat19` clusters range in redshift between $0.01 - 0.2$ and in mass between $(0.4-14)\times10^{14}h^{-1}M_{\odot}$. The cluster catalog provides position, redshift, membership, velocity

dispersion, and mass at overdensities $\Delta = 500, 200, 100, 5.5$ for each cluster. The 34471 member galaxies are identified within the radius at overdensity of $\Delta = 200$. The galaxy catalog provides the coordinates of each galaxy and the ID of the cluster that the galaxy belongs to.

Thirdly, we derive cosmological constraints on the matter density, Ω_m, and the amplitude of fluctuations, σ_8, using `GalWCat19`. We investigate the volume and mass incompleteness of `GalWCat19` to obtain a complete local subsample of 756 clusters (`SelFMC`) in a redshift range of $0.045 \leq z \leq 0.125$ and virial masses of $M \geq 0.8 \times 10^{14}\ h^{-1}\ M_{\odot}$used to constrain Ω_m and σ_8. Utilizing `SelFMC`, we obtain $\Omega_m = 0.310^{+0.023}_{-0.027} \pm 0.041$ (systematic) and $\sigma_8 = 0.810^{+0.031}_{-0.036} \pm 0.035$ (systematic). Our constraints on Ω_m and σ_8 are consistent and very competitive with those obtained from other cosmological probes of Cosmic Microwave Background (CMB), Baryonic Acoustic Oscillation (BAO), and supernovae (SNe). The joint analysis of our cluster data with Planck18+BAO+Pantheon gives $\Omega_m = 0.315^{+0.013}_{-0.011}$ and $\sigma_8 = 0.810^{+0.011}_{-0.010}$.

Contents

List of Figures xi

List of Tables xvii

1 Introduction 1
- 1.1 Galaxy Clusters . . . 3
  - 1.1.1 Components of Galaxy Clusters . . . 3
  - 1.1.2 Observations of Galaxy Clusters . . . 4
  - 1.1.3 Galaxy Cluster Finding . . . 5
  - 1.1.4 Dynamics of Galaxy Clusters . . . 6
- 1.2 Outline . . . 9

2 GalWeight: A New and Effective Weighting Technique for Determining Galaxy Cluster and Group Membership 12
- 2.1 Introduction . . . 13
- 2.2 Simulations . . . 16
- 2.3 The Galaxy Weighting Function Technique (GalWeight) . . . 18
  - 2.3.1 Galaxy Weighting Functions . . . 22
  - 2.3.2 Membership Determination . . . 29
  - 2.3.3 Why do we use total weight rather than dynamical or phase-space weights? . . . 33
  - 2.3.4 Testing the Efficiency of GalWeight on MDPL & Bolshoi Simulations 35
- 2.4 A comparison of membership techniques . . . 40
- 2.5 Observations - Application to a Sample of 12 Abell Clusters . . . 43
- 2.6 Discussion and Conclusion . . . 53

3 GalWeight Application: A publicly-available catalog of dynamical parameters of 1,800 galaxy clusters from SDSS-DR13, (`GalWCat19` 55
- 3.1 Introduction . . . 56
- 3.2 Data and clusters identification . . . 60
  - 3.2.1 SDSS sample . . . 60
  - 3.2.2 Identification of a galaxy cluster . . . 61

3.2.3 Membership identification: GALWEIGHT . . . 63
3.3 Dynamics of galaxy clusters . . . 66
3.4 Application to Simulations . . . 69
3.4.1 Catlaog Completeness as a Function of Cluster Mass and Redshift . . . 69
3.4.2 Effectiveness of Cluster Mass Estimation . . . 75
3.5 GalWeight cluster catalog, `GalWCat19` . . . 78
3.5.1 Dynamical Parameters . . . 78
3.5.2 GalWeight Catalog Matching . . . 82
3.5.3 Velocity dispersion vs. Mass relation . . . 87
3.6 Conclusion . . . 91

4 Cosmological Constraints on Ω_m and σ_8 from Cluster Abundances using the `GalWCat19` Optical-Spectroscopic SDSS Catalog **97**
4.1 Introduction . . . 98
4.2 The `GalWCat19` Cluster Catalog . . . 102
4.3 Cluster mass function . . . 106
4.3.1 `GalWCat19` Completeness . . . 107
4.3.2 Estimating the Mass Function . . . 110
4.4 Implications for Cosmological Models . . . 114
4.4.1 Prediction of Halo Mass Function . . . 114
4.4.2 Constraining Ω_m and σ_8 . . . 118
4.5 Discussion and Conclusion . . . 120
4.5.1 Systematics . . . 121
4.5.2 Comparison with external data from cluster abundance . . . 125
4.5.3 Comparison with external data from non-cluster cosmological probes 129
4.5.4 Conclusion . . . 131

5 Conclusions and Future Work **137**
5.1 Conclusions . . . 137
5.2 Ongoing Work . . . 138
5.2.1 Cluster Richness-Mass Relation . . . 138
5.2.2 Galaxy Stellar Mass Function of numerical simulations . . . 139
5.3 Future Work . . . 139
5.3.1 Connection between Galaxies and Hosting Clusters . . . 139
5.3.2 Velocity Bias between Galaxies and Dark Matter . . . 140

List of Figures

1.1 The flowchart summarizes the pathway to construct cluster catalogs from galaxy surveys and their different astrophysical and cosmological applications. 2

1.2 Nested spherical shells in the field of a simulated cluster. The left panel shows the shells in real space and the right panels show the shells in the redshift spaces. The FoG effect is shown clearly (blue and red shells) in the redshift space. 7

2.1 Line-of-sight velocity v_z as a function of projected radius R_p in the extended region around a simulated cluster of mass $9.37 \times 10^{14}\ h^{-1}\ \mathrm{M}_{\odot}$ selected from the Bolshoi simulation. The Finger-of-God is clearly seen in the main body of the cluster within $R_p \lesssim 1$ Mpc h^{-1}. The effect of the mass concentration in and around the cluster is manifested as a concentration of galaxies around $v_z = 0$ line well outside the cluster itself. Interlopers are mostly galaxies at large projected distances and large peculiar velocities. In § 2.3 and in Figures 2.2, 2.3 & 2.4 we show in detail how GalWeight can be applied to this cluster to distinguish between interlopers and cluster members (Figure 2.5). 19

2.2 Weighting function along projected radius R_p for the simulated cluster of mass $9.37{\times}10^{14}\ h^{-1}\ \mathrm{M}_{\odot}$ selected from Bolshoi (see § 2.3.1 A.1). The left panel (a) shows the function $\mathcal{D}_{R_p}$ derived from the data (black points, Equation (2.1)), normalized by Equation (2.2), and fitted by $\mathcal{W}_{R_p}$ (red curve, Equation (2.4)). The right panel (b) presents its corresponding probability density function in phase-space diagram. As shown in (a & b), the weighting is greatest at $R_p = 0$ and decreases outwards. 20

2.3 Weighting function along line-of-sight velocity v_z for the simulated cluster selected from Bolshoi. The left panel (a) shows the function $\mathcal{D}_{v_z}$ calculated from the data (black points, Equation (2.5)), normalized by Equation (2.6), and fitted by $\mathcal{W}_{v_z}$ (blue curve, Equation (2.7)). The right panel (b) presents its corresponding probability density function in phase-space. As shown in (a & b), the applied weight is greatest at $v_z = 0$ and decreases as the absolute line-of-sight velocity increases. 21

2.4 Weights to be applied as a function of position in line-of-sight velocity/projected radius phase-space for the simulated cluster selected from the Bolshoi simulation. Panel (a) shows the dynamical weight $\mathcal{W}_{dy}$ (The product of the weights shown in Figures 2.2b and 2.3b). Panel (b) presents the phase-space weight $\mathcal{W}_{ph}$ calculated from the 2DAKM. The total weight $\mathcal{W}_{tot} = \mathcal{W}_{dy} \times \mathcal{W}_{ph}$ is shown in panel (c) with explicitly drawing three contour weights. The weight $\mathcal{W}_{dy}$ is maximum at the origin (0,0) and decreases along both the R_p and v_z axes and $\mathcal{W}_{ph}$ gives higher weight for galaxy clumping around the center and substructures as well. Note that the scaling for each panel is independent, with magenta representing maximum values. 26

2.5 Identification of the simulated cluster membership from weighted galaxies. Panel (a) shows the weight of each galaxy in line-of-sight velocity/projected radius phase-space (magenta color indicates higher weight). Panel (b) shows a histogram or PDF of the weight applied to each galaxy, $\mathcal{W}_{tot}(R_{p,i}, v_{z,i})$. 1DAKM fitting returns a bimodal PDF in this example of the simulated cluster. We choose to use the number density method (NDM, Abdullah et al., 2013) to identify the contour weight value which separates cluster members from interlopers. This is shown by the solid red vertical line in panel (c) and solid red line in panel (a). 1σ confidence intervals are shown by the two red dashed lines. The two vertical dashed-black lines represent the virial and turnaround radii, where the cluster members are those enclosed by the best contour line and within the turnaround radius. We impose one additional cut, shown by the black solid lines in panel (a), cutting the red contour line in the very inner radius by the maximum v_z of the enclosed members. . . . 28

2.6 Application of dynamical, phase-space, and total weights (green, blue, and black lines, respectively) to three simulated clusters taken from the Bolshoi simulation (§ 2.2). The red points show true members within $3r_v$. Applying the dynamical weight alone (green) results in the inclusion of many galaxies within $R \sim 1$ Mpc h^{-1} with very high line-of-sight velocities. Applying the phase-space weight alone (blue), fails to recover some members in the core while simultaneously incorrectly including some interlopers at large distances due to the presence of nearby clusterings and clumps. The total weight (black), the product of the dynamical and phase-space weights, recovers true members effectively in both the core and infall regions (see Table 2.1). . . . 30

2.7 Application of the GalWeight technique (solid black lines) to twelve simulated clusters selected from the MDPL simulation (§ 2.2). Red points show fiducial members within $3r_v$. The virial mass ($\log \mathrm{M}_v\ h^{-1}\ \mathrm{M}_\odot$) and number of members within r_v is shown for each cluster. Clearly, GalWeight does well in effectively identifying members with high accuracy in both the virialized and infall regions for structures ranging in mass from rich clusters to poor groups. 37

2.8 Example of four well-known membership techniques applied to two simulated clusters with mass of $10.92 \times 10^{14}\ h^{-1}\ \mathrm{M}_{\odot}$ (top panles) & $4.24 \times 10^{14}\ h^{-1}\ \mathrm{M}_{\odot}$ (bottom) from the Bolshoi simulation (§ 2.2). In each panel, the red points represent fiducial cluster members within $3r_v$, and the solid black lines show the demarcation contour enclosing cluster members, identified by applying our new technique (GalWeight). The open blue circles in panels (a, b, e & f) show members identified by the shifting gapper technique using $N_{bin} = 10$ and $N_{bin} = 15$, respectively. Panel (c & g) shows the caustic technique employing rescale parameters of q=25 (cyan lines), and q=35 (pink lines) and also the Den Hartog technique (dotted black lines). The Yahil SIM (dark green lines) and Regős SIM (light green lines) techniques are presented in panel (d & h). GalWeight recovers fiducial members with high accuracy, improving upon the shifting gapper and den Hartog techniques simultaneously at small and large projected radii, the caustic techniques at small projected radius and the SIM technique at large projected radius ($\sim 3r_v$) 38

2.9 Application of the GalWeight technique to twelve Abell clusters from SDSS-DR12 (see also Table 2.2). The solid black lines shows the optimal contour line and the two dashed vertical lines show the virial and turnaround radii respectively. The red points show galaxies identified as clusters members - those enclosed by optimal contour line and r_t. Also shown in each panel is the cluster virial mass ($\log \mathrm{M}_v\ h^{-1}\ \mathrm{M}_{\odot}$) and number of galaxies within r_v. 46

2.10 Example of four well-known membership techniques applied to the cluster. The blue open symbols and solid lines are as in Figure 2.8. Clearly GalWeight (solid black lines) appears to identify cluster members well both in the virialized and infall regions of phase-space. 51

3.1 Completeness and purity of the FG algorithm. (a): completeness of FG applied to the Bolshoi clusters as a function of cluster mass for at least eight galaxies in a cylinder of radius $R_{cy} = 0.5\ h^{-1}$ Mpc and height 3000 km s^{-1} (see §3.2.2). (b): completeness of FG as a function of richness (number of galaxies in the cylinder). (c): purity of FG as a function of richness. The blue lines represent the rates per bin, and the red lines represent the cumulative rates. 73

3.2 Completeness of GalWeight catalog. (a): the abundance of clusters as a function of mass for `GalWCat19` (red area) compared to the abundance of clusters predicted by Tinker et al. (2008) model (blue area). (b): cluster number density as a function of comoving distance for `GalWCat19`. The solid black line shows the number density the sample and the dashed black horizontal line represents the number density of $5.6 \times 10^{-5}\ h^3\ \mathrm{Mpc}^{-3}$ averaged for the overall sample within distance $D \leq 225\ h^{-1}$. (c): number of clusters as a function of comoving distance. The dashed black line shows the expectation for a completed volume-limited sample with a density of $5.6 \times 10^{-5}\ h^3\ \mathrm{Mpc}^{-3}$ for $\Omega_m = 0.3$ and $\Omega_\Lambda = 0.7$. 73

3.3 Recovered versus true cluster mass applied to the HOD2 (left) and the SAM2 (right) catalogs. The blue dashed lines represent the one-to-one relation. The solid black lines show the linear relationship between the recovered and true log mass. NR in the legend represents the number of missing clusters out of 1000 simulated clusters. 77
3.4 Top panel: Aitoff projection in celestial coordinates. Bottom panel: light cone diagram. The black points represent the distribution of all galaxies in the sample, while the blue and red points represent the distribution of 1,800 clusters members identified by GalWeight which are within r_{200} and $r_{5.5}$, respectively (see §3.3). 79
3.5 Matching `GalWCat19` (blue histograms) with six optical catalogs (red histograms). The histograms of Yoon, GMBCG, WHL, redMaPPer, and Tempel are derived from spectroscopic redshifts provided by each catalog, while the histogram of AMF is derived from photometric redshift that does not provide spectroscopic data. 83
3.6 Top left panel: Velocity dispersion σ_{200} vs. virial mass M_{200} for 1,800 clusters in the `GalWCat19` catalog. The gray points show the `GalWCat19` clusters and the solid black line represents the best-fit relation from Equation 3.27. The blue, purple, green, and red dashed lines show the relations for Evrard et al. (2008), Munari et al. (2013) Saro et al. (2013), and Armitage et al. (2018) derived from cosmological simulations, respectively. As shown, the GalWeight relation matches the models remarkably well, indicating the accuracy of the GalWeight to constrain cluster membership, and consequently determine cluster masses. Bottom left panel: best-fit relations relative to the Evrard et al. (2008) result. Right panel: The distribution of residual of velocity dispersion of clusters from the best-fit line, along with best-fit the Gaussian curve. The inner right panel shows the best-fit parameters of Equation 3.27 with $1, 2, 3\sigma$ confidence intervals. 88

4.1 `GalWCat19` completeness. **Left**: The black line shows the integrated abundance of clusters as a function of redshift for the `GalWCat19` catalog. The dashed color lines present the expectation of complete samples estimated by Tinker08 for five different cosmologies as shown in the legend. **Right**: The black line shows the integrated abundance of clusters as a function of cluster mass. The dashed color lines present the expectation of complete samples estimated by Tinker08 for five different cosmologies as shown in the legend. The fractional error $(N(<z)_{obs} - N(<z)_{model})/N(<z)_{model}$ is shown in the lower panels. The gray shaded areas represent the expected Poisson noise. . 105
4.2 Selection function of `GalWCat19` cluster sample. Colored points show the normalized number density of the five mass bins described in Figure 4.1. The black line shows an exponential form describing the selection function $\mathcal{S}(D)$ which is fitted with the data. The scatter of data relative to the exponential form is presented in the lower panel. 111

4.3 The cumulative CMF derived from the GalWCat19 cluster sample. The black line shows the mass function computed from the MDPL2 simulation (for the snapshot hlist_0.91520.list at $z \sim 0.9$ or $D \sim 260$) (Klypin et al., 2016). The blue points present the CMF for the volume-complete subsample with $D \leq 265\ h^{-1}$ Mpc ($z \sim 0.09$) without the correction of $\mathcal{S}(D)$ (NoSelFVC). The red points show the CMF corrected by $\mathcal{S}(D)$ for $D \leq 365\ h^{-1}$ Mpc($z \sim 0.125$, SelFMC). The vertical dashed line shows the low-mass limit ($\log(M) = 13.9$ $h^{-1}\ M_{\odot}$) used to constrain Ω_m and σ_8. The error bars on the vertical axis are calculated by Poisson statistics. The fractional errors between the CMF of MDPL2 and both NoSelFVC and SelFMC are shown in the lower panels. The gray shaded areas represent the expected Poisson noise. 112
4.4 Likelihood contour map of χ^2 in σ_8-Ω_m plane derived from the SelFMC cluster catalog. The black star represents the best-fit point for Ω_m and σ_8 which minimizes χ^2 value. Ellipses show 1σ, 2σ, and 3σ confidence levels, respectively. The dashed yellow line represents the best-fit σ_8-Ω_m relation as shown in the legend. 115
4.5 Effect of varying Ω_m and σ_8 on the HMF. The left panel shows the HMF calculated from Tinker08 for five different values of Ω_m= [0.1 0.2 0.3 0.4 0.5] while fixing σ_8= 0.3 (solid colored lines as shown in the legend). The right panel shows the HMF calculated from Tinker08 for five different values of σ_8= [0.6 0.7 0.8 0.9 1.0] while fixing Ω_m= 0.3 (solid colored lines as shown in the legend). Our derived CMF corrected by $\mathcal{S}(D)$ for $D \leq 365\ h^{-1}$ Mpc($z \sim 0.125$) is shown by black points. 116
4.6 Effects of cluster mass uncertainty (left), mass threshold (middle), and selection function (right) on our constraints on Ω_m and σ_8. **Left**: the 68% CLs of our fiducial sample (black), fractional mass uncertainty (blue), and intrinsic scatter of 0.23 (red). **Middle**: the 68% CLs (green) for varying mass threshold $\log M$ from 13.8 to 14 $h^{-1}\ M_{\odot}$. **Right**: the 68% CLs (magenta) due to systematic of the selection function. 120
4.7 Constraints on Ω_m and σ_8 obtained from cluster abundance studies (cluster mass function; CMF). Left: 68% confidence levels (CLs) derived from SelFMC (magenta) plus select other optical, X-ray or SZ-detected cluster catalogs as shown in the legend and summarized in the first three sections of Table 4.2. The two dashed lines show the best-fit values derived in this work. Right: Uncertainties on Ω_m and σ_8 for each of the cluster abundance studies listed in Table 4.2 (Note: For clarity, not all studies in Table 4.2 are shown in the left panel). While in agreement with the other cluster abundance studies within 1σ uncertainties, the value of Ω_m determined from our work is slightly higher and the value of σ_8 slightly lower than most of the other studies. As shown in Fig 4.8 and discussed in § 4.5.3, we note that our values are in better agreement with Ω_m and σ_8 obtained from non-cluster determinations as shown in Fig 4.8. 123

4.8 Constraints on Ω_m and σ_8 obtained from cluster abundance (`SelFMC`; magenta) and non-cluster cosmological constraint methods. Left: 68% confidence levels (CLs) derived from `SelFMC`, WMAP9 (CMB; Hinshaw et al., 2013), Planck18 (CMB; Planck Collaboration et al., 2018), BAO data (Beutler et al., 2011; Ross et al., 2015; Alam et al., 2017), Pantheon sample (SNe; Scolnic et al., 2018), and the surveys KiDS+GAMA (van Uitert et al., 2018) and DES Y1 (Abbott et al., 2018b) which both use the cosmological probes of cosmic shear, galaxy-galaxy lensing, and angular clustering. As in Figure 4.7, the two dashed lines show the best-fit values derived in this work. The constraints on Ω_m and σ_8 derived from `SelFMC` are consistent with those derived from the non-cluster methods. Joint analysis between our constraints and the results of Planck18+BAO+Pantheon is represented by the red contour line. Right: uncertainties of Ω_m and σ_8 estimated for the aforementioned probes except for the BAO and SNe probes which constrain Ω_m only. 128

4.9 The effect of cluster number density evolution. **Left**: Tinker08 HMF times M^2/ρ_c at different redshifts as well as the average HMF for $0.0 \leq z \leq 0.125$ (brawn) and $0.045 \leq z \leq 0.125$ (red) as shown in the legend. **Right**: The scatter of each HMF relative to that at $z = 0.085$ (the mean redshift of the sample). 134

4.10 The effect of adopting the redshift threshold. **Left**: 68% CLs for three subsamples with fixing the upper redshift threshold to 0.125 and decreasing the lower redshift threshold from 0.075 to 0.045. The dashed brown ellipse represents the 68% CL of the `NoSelFVC` sample. **Right**: 68% CLs for three subsamples with fixing the lower redshift threshold to 0.045 and increasing the upper redshift threshold from 0.125 to 0.16. 135

List of Tables

2.1 Efficiency of the GalWeight technique determined by calculating f_c and f_i at r_v, $2r_v$ and $3r_v$ for a sample of ~ 3000 clusters from the MDPL2 & Bolshoi simulations. 34
2.2 Dynamical parameters derived for the sample of twelve Abell galaxy clusters 48
2.3 GalWeight-determined ratios of radii and mass for each of the twelve Abell clusters compared to previously-published values 50

3.1 Coordinates, dynamical parameters at R_{200}, and NFW parameters for the first 15 clusters in the `GalWCat19` catalog (see Appendix 3.6). 80
3.2 Matches with other catalogs. 84

4.1 The cluster average number density for different mass bins. 110
4.2 Comparison of constraints on cosmological parameters Ω_m and σ_8 derived from Clusters Abundances (CMF) and from Other Cosmological Probes, including cosmic shear, galaxy-galaxy lensing, angular clustering, BAO, supernovae, and CMB 124

Chapter 1

Introduction

Large ongoing and future wide and deep-field surveys of galaxies [e.g., DES (Abbott et al., 2018a), DESI (Levi et al., 2019), Euclid (Euclid Collaboration et al., 2019), eBOSS (Raichoor et al., 2017), eROSITA (Merloni et al., 2012), LSST (LSST Science Collaboration et al., 2009), and WFIRST (Akeson et al., 2019)] are our unique tools for studying galaxy clusters, cosmology, and galaxy formation and evolution. These galaxy surveys are used to construct galaxy cluster catalogs which provide an exquisite data source for a wide range of cosmological and astrophysical applications. In particular, the statistical study of the abundance of galaxy clusters as a function of mass and redshift (Wang & Steinhardt, 1998; Haiman et al., 2001; Reiprich & Böhringer, 2002; Battye & Weller, 2003; Dahle, 2006; Lima & Hu, 2007; Wen et al., 2010b) is a powerful tool for constraining the cosmological parameters, specifically the normalization of the power spectrum, σ_8, and the matter density parameter, Ω_m. Catalogs of galaxy clusters are also interesting laboratories to investigate galaxy evolution under the influence of extreme environments (Butcher & Oemler, 1978;

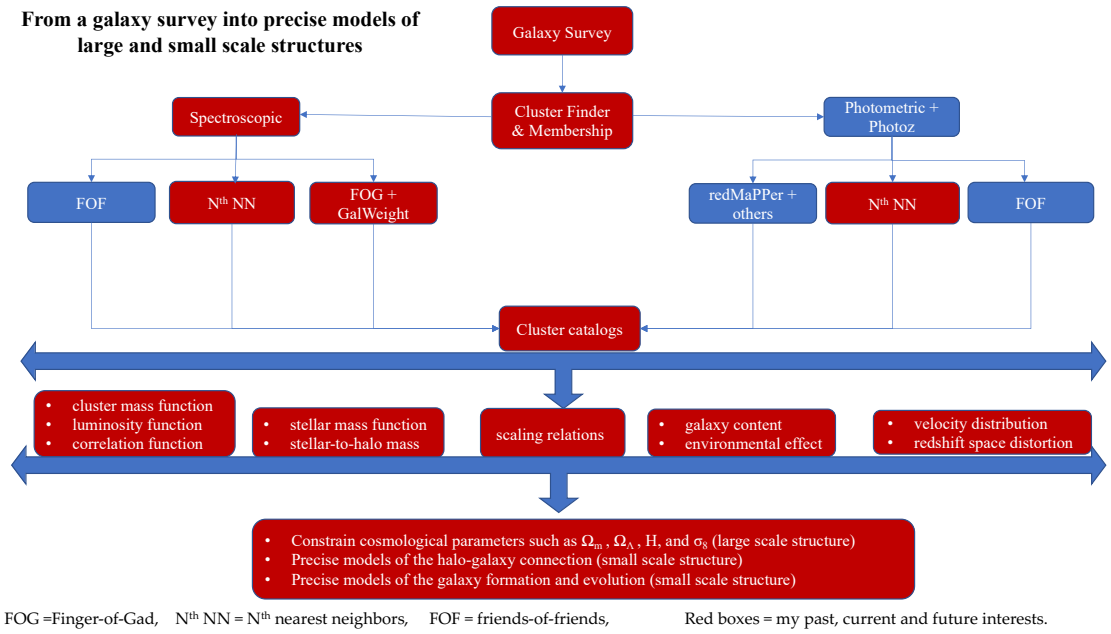

Figure 1.1: The flowchart summarizes the pathway to construct cluster catalogs from galaxy surveys and their different astrophysical and cosmological applications.

Dressler, 1980; Goto et al., 2003; Leauthaud et al., 2012; Bayliss et al., 2016; Foltz et al., 2018). Moreover, they can be utilized to study the galaxy-halo connection which correlates galaxy growth with halo growth (e.g., Wechsler & Tinker, 2018). The connection between numerical simulations and observations is a key role in guiding the development of accurate theoretical models which will advance our understanding of the hierarchical growth of structure, cosmology, and galaxy formation and evolution (see the flowchart in Figure 1.1).

Identification of galaxy clusters and estimation of cluster masses are the key challenges to accurately constructing cluster catalogs. In this dissertation, we introduce an automated technique for constructing galaxy cluster catalogs, identifying cluster members, and estimating cluster masses (Abdullah et al., 2018, 2020b), which can be applied to optical spectroscopic galaxy surveys. The cluster locations are identified by searching for the

Finger-of-God effect (FoG, see Jackson, 1972; Kaiser, 1987; Abdullah et al., 2013). This is the distortion of line-of-sight velocities of galaxies both in viral and infall regions due to the cluster potential well, i.e. galaxies peculiar motions. The cluster members are identified by the GalWeight technique introduced in Abdullah et al. (2018). The cluster masses are calculated from the dynamics of the member galaxies using the virial mass estimaor (e.g., Limber & Mathews, 1960; Abdullah et al., 2011) corrected for the surface pressure term (e.g., The & White, 1986; Carlberg et al., 1997), and the NFW model (Navarro et al., 1996, 1997).

1.1 Galaxy Clusters

Galaxy clusters are the most massive bound systems in the universe and are uniquely powerful cosmological probes. Cluster dynamical parameters, such as line-of-sight velocity dispersion, optical richness, and mass are closely tied to the formation and evolution of large-scale structure (Postman et al., 1992; Carlberg et al., 1996; Sereno & Zitrin, 2012).

1.1.1 Components of Galaxy Clusters

Galaxy clusters consist of three main components listed as follows. I. An aggregate of 100-1000 galaxies in a region of $\sim$ two Mpc. It contributes about 10% of the baryons in the clusters. II. Intracluster medium (ICM) of hot ionized gas and dust surrounding galaxies. It contributes about 90% of the baryons in the clusters. The ICM consists mainly of ionized hydrogen, heated to extremely high temperatures as it fall into the gravitational potential

well of the cluster (e.g., Sarazin, 1988). III. The dark matter which contributes about 90% of the total cluster mass. The dark matter does not emit or reflect electromagnetic radiation, but its presence is inferred by its gravitational effect on luminous matter.

1.1.2 Observations of Galaxy Clusters

Galaxy clusters can be detected based on a number of different properties, such as: i) X-ray emission from hot intracluster gas (e.g., Sarazin, 1988; Reichardt et al., 2013); ii) the Sunyaev-Zeldovich (SZ) effect (distortion of the cosmic microwave background radiation by electrons of hot intracluster gas; Planck Collaboration et al., 2011); iii) optical (e.g., Abell et al., 1989; den Hartog & Katgert, 1996; Abdullah et al., 2011) and infrared emissions (e.g., Genzel & Cesarsky, 2000; Muzzin et al., 2009; Wilson et al., 2009; Wylezalek et al., 2014) from stars in cluster members. Using current capabilities, both X-ray emission and SZ effect are detectable only for the very deep gravitational potential wells of the most massive systems. They cannot be used to detect the outskirts of massive clusters, or intermediate/low-mass clusters. Thus, current optical surveys of galaxies, such as SDSS, and upcoming surveys such as Euclid (Amendola et al., 2013), and LSST (LSST Science Collaboration et al., 2009) are required in order to produce the largest and most complete cluster sample.

Optically, galaxy surveys provides data for position, spectroscopic and/or photometric redshift, magnitudes and other parameters for galaxies. Cluster catalogs constructed by photometric data introduce a large number of groups of different richness ranging from a pair of galaxies to very massive clusters with hundreds of galaxies for entire surveys. However, using photometric redshift to extract cluster catalogs leads to substantial uncertainty

in identifying clusters and their membership in comparison to spectroscopically produced catalogs. Cluster catalogs constructed by spectroscopic data show high accuracy in determining cluster membership but it is prohibitively expensive to obtain spectroscopy of large samples of galaxies. Thus, the expected number of clusters identified spectroscopically is very small relative to that identified photometrically.

1.1.3 Galaxy Cluster Finding

There are many statistical cluster finding methods which rely on optical surveys. For instance, the friends-of-friends (FoF) algorithm is the most frequently usable means for identifying groups and clusters in galaxy redshift data (Turner & Gott, 1976; Press & Davis, 1982). It uses galaxy distances derived from spectroscopic or photometric redshifts as the main basis of grouping. Another group of cluster finding methods are halo-based group finders (Yang et al., 2005, 2007; Duarte & Mamon, 2015). These methods assume some criteria to identify galaxies which belong to the same dark matter halo. There are other cluster finding methods which are used in the literature, including density-field based methods (e.g., Miller et al., 2005), matched filter techniques (e.g., Kepner et al., 1999; Milkeraitis et al., 2010; Bellagamba et al., 2018), and the Voronoi-Delaunay method (e.g., Ramella et al., 2001; Pereira et al., 2017; Soares-Santos et al., 2011). These methods are capable of identifying clusters and groups of different richness ranging from a pair of galaxies to very massive clusters with hundreds of galaxies for entire surveys. However, they assume certain criteria and apply fast-run codes to construct catalogs of entire surveys. This may lead to inaccurate results for recovering the true cluster members because the proposed criteria could be suitable for only some individual clusters depending on their masses and/or

dynamical status. Also, most of these methods use photometric redshift to extract cluster catalogs, leading to substantially more uncertainty in cluster membership in comparison to spectroscopically produced catalogs.

Moreover, there are some cluster finding techniques that depend on the physical properties of galaxy clusters, such as, FOG (e.g., Jackson, 1972; Kaiser, 1987; Abdullah et al., 2013), gravitational lensing (e.g., Metzler et al., 1999; Kubo et al., 2009), red-sequence (e.g., Gladders & Yee, 2005; Rykoff et al., 2014), and Stellar Bump Sequence (SBS) introduced by Muzzin et al. (2013). We discuss the FOG effect in detail in the next section since this is the feature that we use in identifying galaxy clusters in our investigation.

1.1.4 Dynamics of Galaxy Clusters

Galaxy clusters can be divided into three regions: The core, the virialized region and the infall region. The core is the region in which the motion of galaxies is randomly distributed Binney & Tremaine (1987); Praton & Schneider (1994). The boundary of this region is the core radius which cannot determine accurately, but it extends to $\sim 0.25 - 0.5$ Mpc. The virialized region is the region in which the system is in a dynamical equilibrium or the radial velocity $\approx$ transverse velocity. The boundary of this region is the viral radius r_v. It is approximately equal to the radius at which the density $\rho = \Delta_{200}\rho_c$, where ρ_c is the critical density of the Universe and $\Delta_{200} = 200$ (e.g., Carlberg et al., 1997). Therefore, we assume that $r_v = r_{200}$. The infall region in which galaxies radially infall to the center center. The boundary of this infall reion is the turnaround radius r_t at which a galaxy's peculiar velocity (v_{pec}) is canceled out by the global Hubble expansion. In other words, it is the radius at which the infall velocity vanishes ($v_{inf} = v_{pec} - H\ r = 0$), which can be

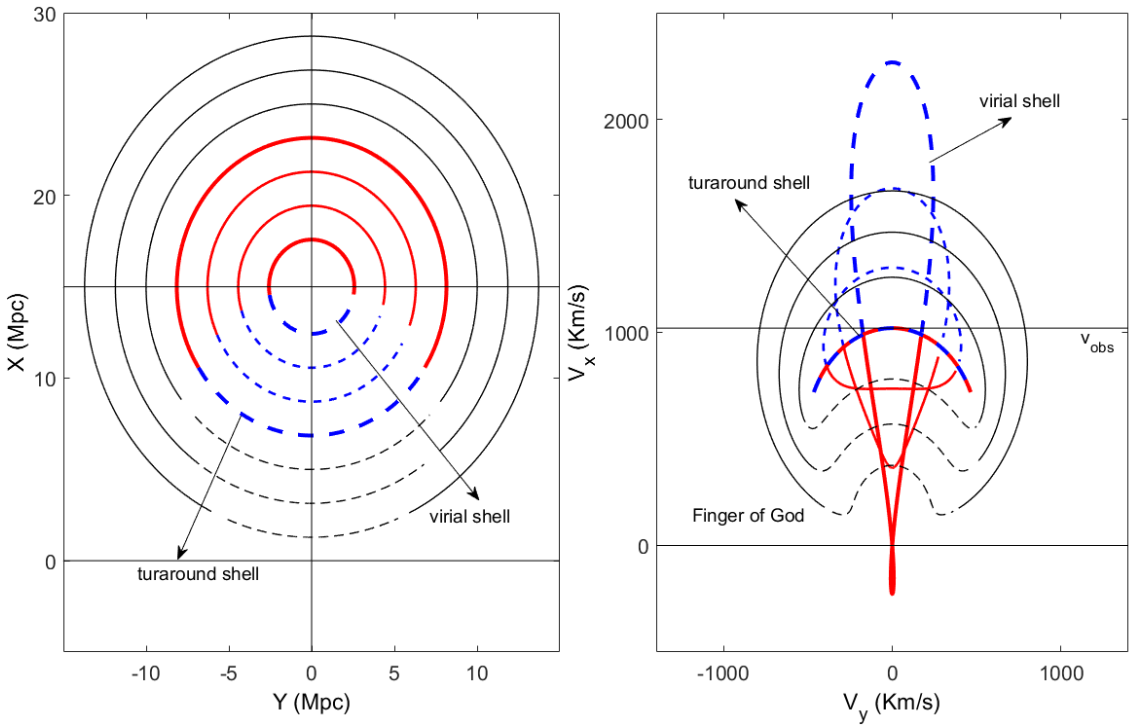

Figure 1.2: Nested spherical shells in the field of a simulated cluster. The left panel shows the shells in real space and the right panels show the shells in the redshift spaces. The FoG effect is shown clearly (blue and red shells) in the redshift space.

calculated as the radius at which $\rho = 5.55\rho_c$ (e.g., Nagamine & Loeb, 2003; Busha et al., 2005; Dünner et al., 2006).

In Figure 1.2, we introduce a set of nested shells of a spherically symmetric simulated cluster. The shells are shown in both real space (left) and redshift space (right). Shells drawn with thin lines are outside the cluster's turnaround shell (bold) and shells drawn with thick lines are inside. The innermost shell represents the virial radius. The near side of each shell is dashed and the far side is solid line. Note that the shells inside the turnaround turn inside-out so that near side and far side reverse, while the turnaround shell collapses so that its near side and far side coincide to form a circular arc in this cross-section view. The shells immediately outside the turnaround do not turn inside out, but are crowded together,

so that some material outside the turnaround lies inside the envelope. This illustrates the triplevalue problem (see Tonry & Davis, 1981), where there are some foreground and background galaxies that appear to be part of the cluster because of the distortion in redshift space. In the redshift space, the distortion of line-of-sight velocities of galaxies (shells) both in viral and infall regions due to the cluster potential well is shown clearly in right panel. We introduce a simple algorithm, called FG, that identifies locations of clusters by looking for the FOG effect. Similar algorithms were introduced in the literature to identity FoG (e.g., Yoon et al., 2008; Tempel et al., 2018). We identify galaxy clusters in the redshift space using the FG algorithm in the optical band using a high-quality spectroscopic data set.

The observed velocity of a galaxy, of radial infall speed $s_{\rm rad}$ and azimuthal angle ϕ, on a shell of radius r' centered on the cluster is given by

$$\begin{aligned} s_{\rm obs} = (H_0 R - v_{0x})\cos\phi - \left(s_{\rm rot}(r')\frac{R}{r'} + v_{0y}\right)\sin\phi \\ \pm \left(H_0 r' - s_{\rm rad}(r')\right)\left(1 - \left(\frac{R}{r'}\sin\phi\right)^2\right)^{1/2}, \end{aligned} \tag{1.1}$$

where v_{0x} and v_{0y} are the radial and transverse peculiar velocities of the observer, respectively, and $s_{\rm rot}$ is rotational speed about the cluster center (see Abdullah et al., 2013 for details). Notice that equation 1.1 is a generalized case of equation (23) in Regos & Geller (1989), which ignores the spatial velocity of the observer with respect to the cluster center and assumes the flow is purely radial.

1.2 Outline

The dissertation includes three publications which are discussed in the next three chapters. In chapter two, we discuss the issue of identification of cluster membership and introduce the GalWeight technique, a new technique for assigning galaxy cluster membership. This technique is specifically designed to simultaneously maximize the number of *bona fide* cluster members while minimizing the number of contaminating interlopers. The GalWeight technique can be applied to both massive galaxy clusters and poor galaxy groups. Moreover, it is effective in identifying members in both the virial and infall regions with high efficiency. We apply the GalWeight technique to MDPL2 & Bolshoi N-body simulations, and find that it is $> 98\%$ accurate in correctly assigning cluster membership. We show that GalWeight compares very favorably against four well-known existing cluster membership techniques (shifting gapper; Girardi et al., 1998b, den Hartog; den Hartog & Katgert, 1996, caustic; Diaferio, 1999, SIM; Yahil, 1985; Regos & Geller, 1989). We also apply the GalWeight technique to a sample of twelve Abell clusters (including the Coma cluster) using observations from the Sloan Digital Sky Survey. This chapter is introduced in the publication Abdullah M. H., Wilson G., Klypin A., 2018, ApJ, 861, 22, Abdullah et al. (2018).

In chapter three, we apply the GalWeight technique to the SDSS-DR13 spectroscopic data set to create a new publicly-available catalog of 1800 galaxy clusters (GalWeight cluster catalog, `GalWCat19`) and a corresponding catalog of 34471 identified member galaxies. The clusters are identified from overdensities in redshift-phase space by looking for FOG. The cluster masses are calculated individually using the virial theorem, corrected

for the surface pressure term and NFW model. The completeness of the cluster catalog (`GalWCat19`) and the procedure followed to determine cluster mass are tested on the Bolshoi N-body simulations. The 1800 `GalWCat19` clusters range in redshift between $0.01 - 0.2$ and in mass between $(0.4 - 14) \times 10^{14} h^{-1} M_{\odot}$. The cluster catalog provides a large number of cluster parameters including sky position, redshift, membership, velocity dispersion, and mass at overdensities $\Delta = 500, 200, 100, 5.5$. The 34471 member galaxies are identified within the radius at which the density is 200 times the critical density of the Universe. The galaxy catalog provides the coordinates of each galaxy and the ID of the cluster that the galaxy belongs to. The relationship between In this chapter, we also discuss the comparison between the `GalWCat19` catalog and some previous catalogs and introduce the cluster mass-velocity dispersion relation. This chapter is introduced in the publication Abdullah M. H., Wilson G., Klypin A., Old L., Ali G. B., 2020, ApJS, 246, 2, Abdullah et al. (2020b).

In chapter four, we derive cosmological constraints on the matter density, Ω_m, and the amplitude of fluctuations, σ_8, using `GalWCat19`. We investigate the volume and mass incompleteness of `GalWCat19` to obtain a complete local subsample of 756 clusters (`SelFMC`) in a redshift range of $0.045 \leq z \leq 0.125$ and virial masses of $M \geq 0.8 \times 10^{14}$ h^{-1} $M_{\odot}$ with mean redshift of $z = 0.085$ used to constrain Ω_m and σ_8. We compare our complete sample with theoretical models to constrain the cosmological parameters. By analyzing the `SelFMC` sample, we obtain $\Omega_m = 0.310^{+0.023}_{-0.027} \pm 0.041$ (systematic) and $\sigma_8 = 0.810^{+0.031}_{-0.036} \pm 0.035$ (systematic), with a cluster normalization relation of $\sigma_8 = 0.43\Omega_m^{-0.55}$. We compare our results with recent results constrained from some cosmological probes. Our constraints on Ω_m and σ_8 are consistent and very competitive with those obtained from

non-cluster abundance cosmological probes such as Cosmic Microwave Background (CMB), Baryonic Acoustic Oscillation (BAO), and supernovae (SNe). The joint analysis of our cluster data with Planck18+BAO+Pantheon gives $\Omega_m = 0.315^{+0.013}_{-0.011}$ and $\sigma_8 = 0.810^{+0.011}_{-0.010}$. There are several unique aspects to this approach: we use the largest spectroscopic data set currently available, and we assign membership using the GalWeight technique which we have shown to be very effective at simultaneously maximizing the number of *bona fide* cluster members while minimizing the number of contaminating interlopers. Moreover, rather than employing scaling relations, we calculate cluster masses individually using the virial mass estimator. Since `GalWCat19` is a low-redshift cluster catalog we do not need to make any assumptions about evolution either in cosmological parameters or in the properties of the clusters themselves. This chapter is accepted for publication in the ApJ as Abdullah M. H., Klypin A., Wilson G., 2020b, Abdullah et al. (2020a) (accepted for publication in the ApJ in July 2020).

Chapter 2

GalWeight: A New and Effective Weighting Technique for Determining Galaxy Cluster and Group Membership

We introduce GalWeight, a new technique for assigning galaxy cluster membership. This technique is specifically designed to simultaneously maximize the number of *bona fide* cluster members while minimizing the number of contaminating interlopers. The GalWeight technique can be applied to both massive galaxy clusters and poor galaxy groups. Moreover, it is effective in identifying members in both the virial and infall regions with high efficiency. We apply the GalWeight technique to MDPL2 & Bolshoi N-body simulations, and find that it is $> 98\%$ accurate in correctly assigning cluster membership. We show that

GalWeight compares very favorably against four well-known existing cluster membership techniques (shifting gapper, den Hartog, caustic, SIM). We also apply the GalWeight technique to a sample of twelve Abell clusters (including the Coma cluster) using observations from the Sloan Digital Sky Survey. We end by discussing GalWeight's potential for other astrophysical applications.

2.1 Introduction

The problem of contamination of kinematic samples of galaxies in clusters by foreground and background galaxies is longstanding. It arises because of the fact that only the projected positions and velocities of galaxies are measured in redshift surveys. Due to the lack of knowledge about the motion perpendicular to the line of sight, it is difficult to judge a priori which of the galaxies found close to a cluster in projected space are actually bound to it and a good tracer of the underlying potential. Excluding fiducial members or including unbound galaxies, or interlopers, may lead to significantly incorrect estimates of the cluster mass.

Several methods have been suggested in the literature to address this problem. All these methods aim at cleaning the galaxy sample by removing non-members before attempting a dynamical analysis of the cluster. Some algorithms utilize only the redshift information, such as (i) the 3σ-clipping method (Yahil & Vidal, 1977) which iteratively eliminates interlopers with velocities greater than 3σ; (ii) the fixed gapper technique (Beers et al., 1990; Zabludoff et al., 1990) in which any galaxy that is separated by more than a fixed value (e.g., 1σ of the sample or 500-1000 km s^{-1}) from the central body of the

velocity distribution is rejected as a non-member; or (iii) the jackknife technique (Perea et al., 1990a) which removes the galaxy whose elimination causes the largest change in the virial mass estimator. These methods are primarily based on statistical rules and some selection criteria. Other algorithms utilize both position and redshift information, such as (i) the shifting gapper technique (Fadda et al., 1996) which applies the fixed gapper technique to a bin shifting along the distance from the cluster center, or (ii) the den Hartog & Katgert (1996) technique that estimates the maximum (escape) velocity as a function of distance from the cluster center calculated either by the virial or projected mass estimator (e.g., Bahcall & Tremaine, 1981; Heisler et al., 1985).

In addition to the techniques described above, the spherical infall models (hereafter referred to as SIMs, e.g., Gunn & Gott, 1972; Yahil, 1985; Regos & Geller, 1989; Praton & Schneider, 1994) can determine the infall velocity as a function of distance from the cluster center. The SIM in phase-space has the shape of two trumpet horns glued face to face (Kaiser, 1987) which enclose the cluster members. However, studies shows that clusters are not well fit by SIMs in projected phase-space diagram, because of the random motion of galaxies in the cluster outer region caused by the presence of substructure or ongoing mergers (van Haarlem & van de Weygaert, 1993; Diaferio, 1999). A recent investigation (Abdullah et al., 2013) showed that SIMs can be applied to a sliced phase-space by taking into account the distortion of phase-space due to transverse motions of galaxies with respect to the observer and/or rotational motion of galaxies in the infall region in the cluster-rest frame. However, that is out of the scope of the current paper.

Another sophisticated method is the caustic technique described by Diaferio (1999) which, based on numerical simulations (Serra & Diaferio, 2013), is estimated to be able to identify cluster membership with $\sim$ 95% completeness within $3r_v$ (r_v is the virial radius defined below). The caustic technique depends on applying the two-dimensional adaptive kernel method (hereafter, 2DAKM, e.g., Pisani, 1993, 1996) to galaxies in phase-space (R_p, v_z), with the optimal smoothing length $h_{opt} = (6.24/N)\sqrt{(\sigma^2_{R_p} + \sigma^2_{v_z})/2}$, where σ_{R_p} and σ_{v_z} are the standard deviations of projected radius and line-of-sight velocity, respectively, and N is the number of galaxies. σ_{R_p} and σ_{v_z} should have the same units and therefore the coordinates (R_p, v_z) should be rescaled such that $q = \sigma_v/\sigma_{R_p}$, where q is a constant which is usually chosen to be 25 or 35 (additional details about the application of this technique may be found in Serra et al., 2011).

One more technique that should be mentioned here is the halo-based group finder (Yang et al., 2005, 2007). Yang et al. (2007) were able to recover true members with $\sim$ 95% completeness in the case of poor groups ($\sim 10^{13}\mathrm{M}_\odot$). However, they found that the completeness dropped to $\sim$ 65% for rich massive clusters ($\sim 10^{14.5}\mathrm{M}_\odot$). Also, theirs is an iterative method which needs to be repeated many times to obtain reliable members. Moreover, its application depends on some assumptions and empirical relations to identify the group members.

This paper introduces a simple and effective new technique to constrain cluster membership which avoids some issues of other techniques e.g., selection criteria, statistical methods, assumption of empirical relations, or need for multiple iterations. The paper is organized as follows. The simulations used in the paper are described in §2.2. In §2.3 the

GalWeight technique is introduced and its efficiency at identifying *bona fide* members is tested on MultiDark N-body simulations. In §2.4, we compare GalWeight with four well-known existing cluster membership techniques (shifting gapper, den Hartog, caustic, SIM). We apply GalWeight to twelve Abell clusters (including the Coma cluster) in §2.5, and present our conclusions in §4.5.4. Throughout this paper we adopt ΛCDM with $\Omega_m = 0.3$, $\Omega_\Lambda = 0.7$, and $H_0 = 100\ h$ km s^{-1} Mpc^{-1}, $h = 1$.

2.2 Simulations

In this section we describe the simulated data that we use in this work in order to test the efficiency of the GalWeight technique to recover the true membership of a galaxy cluster.

1. MDPL2: The MDPL2 [1] simulation is an N-body simulation of 3840^3 particles in a box of co-moving length 1 h^{-1} Gpc, mass resolution of $1.51 \times 10^9\ h^{-1}$ M$_\odot$, and gravitational softening length of 5 h^{-1} kpc (physical) at low redshifts from the suite of MultiDark simulations (see Table 1 in Klypin et al., 2016). It was run using the L-GADGET-2 code, a version of the publicly available cosmological code GADGET-2 (Springel, 2005). It assumes a flat ΛCDM cosmology, with cosmological parameters $\Omega_\Lambda = 0.692$, $\Omega_m = 0.307$, $\Omega_b = 0.048$, $n = 0.96$, $\sigma_8 = 0.823$, and $h = 0.678$ (Planck Collaboration et al., 2014). MDPL2 provides a good compromise between numerical resolution and volume (Favole et al., 2016). It also provides us with a large number of clusters of different masses extended from $0.7{\times}10^{14}$ to $37.4 \times 10^{14}\ h^{-1}\ M_\odot$ (the range used to test the efficiency of GalWeight).

[1] https://www.cosmosim.org/cms/simulations/mdpl2/

2. Bolshoi: The Bolshoi simulation is an N-body simulation of 2048^3 particles in a box of co-moving length 250 h^{-1} Mpc, mass resolution of 1.35×10^8 h^{-1} $M_\odot$, and gravitational softening length of 1 h^{-1} kpc (physical) at low redshifts. It was run using the Adaptive Refinement Tree (ART) code (Kravtsov et al., 1997). It assumes a flat ΛCDM cosmology, with cosmological parameters ($\Omega_\Lambda = 0.73$, $\Omega_m = 0.27$, $\Omega_b = 0.047$, $n = 0.95$, $\sigma_8 = 0.82$, and $h = 0.70$. Bolshoi provides us with clusters of higher mass resolution than MDPL2. Thus, we use both simulations to test the efficiency of GalWeight to recover the true membership.

For both simulations halos are identified using the Bound Density Maximum (BDM) algorithm (Klypin & Holtzman, 1997; Riebe et al., 2013), that was extensively tested (e.g., Knebe et al., 2011) which identifies local density maxima, determines a spherical cut-off for the halo with overdensity equal to 200 times the critical density of the Universe ($\rho = 200\rho_c$) for MDPL2 and 360 times the background matter density of the Universe ($\rho = 360\rho_{bg}$), and removes unbound particles from the halo boundary. Among other parameters, BDM provides a virial masses and radii. The virial mass is defined as $M_v = \frac{4}{3}\pi 200\rho_c r_v^3$ for MDPL2 and $M_v = \frac{4}{3}\pi 360\rho_{bg} r_v^3$ for Bolshoi (see Bryan & Norman, 1998; Klypin et al., 2016). The halo catalogs are complete for halos with circular velocity $v_c \geq 150$ km s^{-1} for MDPL2 (Klypin et al., 2016) and $v_c \geq 100$ km s^{-1} for Bolshoi (e.g., Klypin et al., 2011; Busha et al., 2011; Old et al., 2015).

For both MDPL2 and Bolshoi the phase-space (line-of-sight velocity v_z versus projected radius R_p) of a distinct halo (cluster) is constructed as follows. We assume the line-of-sight to be along the z-direction and the projection to be on the x-y plane. We select

a distinct halo of coordinates (x^h, y^h, z^h) and velocity components (v_x^h, v_y^h, v_z^h), and then we calculate the observed line-of-sight velocity of a subhalo, taking the Hubble expansion into account, as $v_z = (v_z^g - v_z^h) + H_0(z^g - z^h)$, where (x^g, y^g, z^g) and (v_x^g, v_y^g, v_z^g) are the coordinates and velocity components of the subhalo, respectively. Finally, we select all subhalos within a projected radius of [2] $R_{p,max} = 10\ h^{-1}$ Mpc from the center of distinct halo and within a line-of-sight velocity interval of $|v_{z,max}| = 3500$ km s^{-1}. These values are chosen to be sufficiently large to exceed both the turnaround radius and the length of the Finger-of-God (hereafter, FOG) which are typically $\sim 7 - 8\ h^{-1}$ Mpc and ~ 6000 km s^{-1} respectively for massive clusters. The turnaround radius r_t is the radius at which a galaxy's peculiar velocity (v_{pec}) is canceled out by the global Hubble expansion. In other words, it is the radius at which the infall velocity vanishes ($v_{inf} = v_{pec} - H\ r = 0$).

2.3 The Galaxy Weighting Function Technique (GalWeight)

In this section, we describe the GalWeight technique in detail and demonstrate its use by applying it interactively to a simulated cluster of mass $9.37 \times 10^{14}\ h^{-1}\ M_\odot$ selected from the Bolshoi simulation. Figure 2.1 shows the phase-space distribution of subhalos (galaxies) near the center of the simulated cluster.

The GalWeight technique works by assigning a weight to each galaxy i according to its position ($R_{p,i}$,$v_{z,i}$) in the phase-space diagram. This weight is the product of two separate two-dimensional weights which we refer to as the **dynamical** and **phase-space** weights. The dynamical weight (see § 2.3.1 parts A.1 and A.2, and Figure 2.4a which is

[2] Throughout the paper we utilize small r to refer to 3D radius and capital R to refer to projected radius.

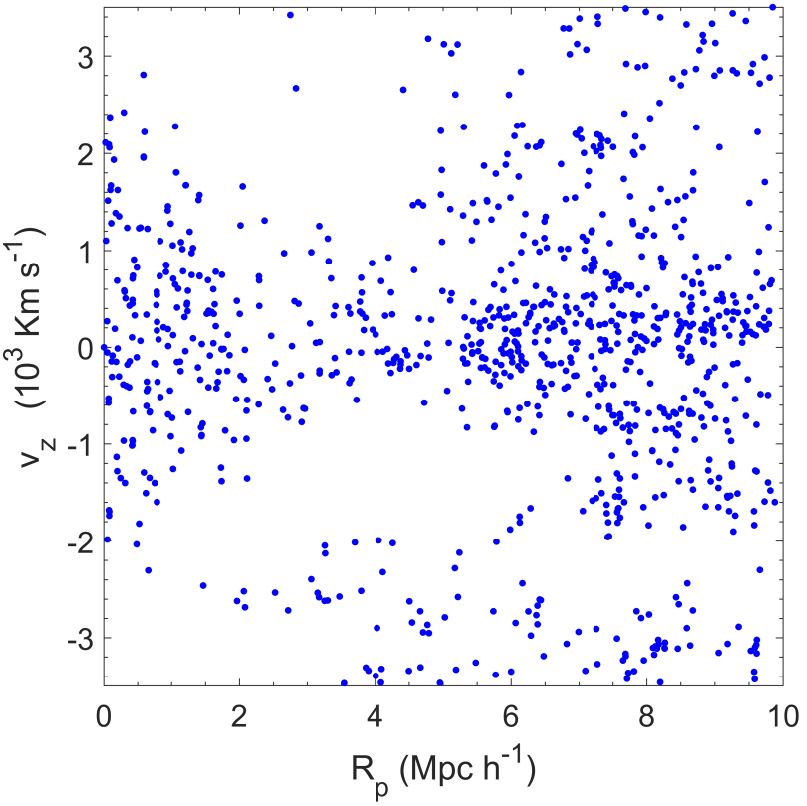

Figure 2.1: Line-of-sight velocity v_z as a function of projected radius R_p in the extended region around a simulated cluster of mass 9.37×10^{14} h^{-1} $M_\odot$ selected from the Bolshoi simulation. The Finger-of-God is clearly seen in the main body of the cluster within $R_p \lesssim 1$ Mpc h^{-1}. The effect of the mass concentration in and around the cluster is manifested as a concentration of galaxies around $v_z = 0$ line well outside the cluster itself. Interlopers are mostly galaxies at large projected distances and large peculiar velocities. In § 2.3 and in Figures 2.2, 2.3 & 2.4 we show in detail how GalWeight can be applied to this cluster to distinguish between interlopers and cluster members (Figure 2.5).

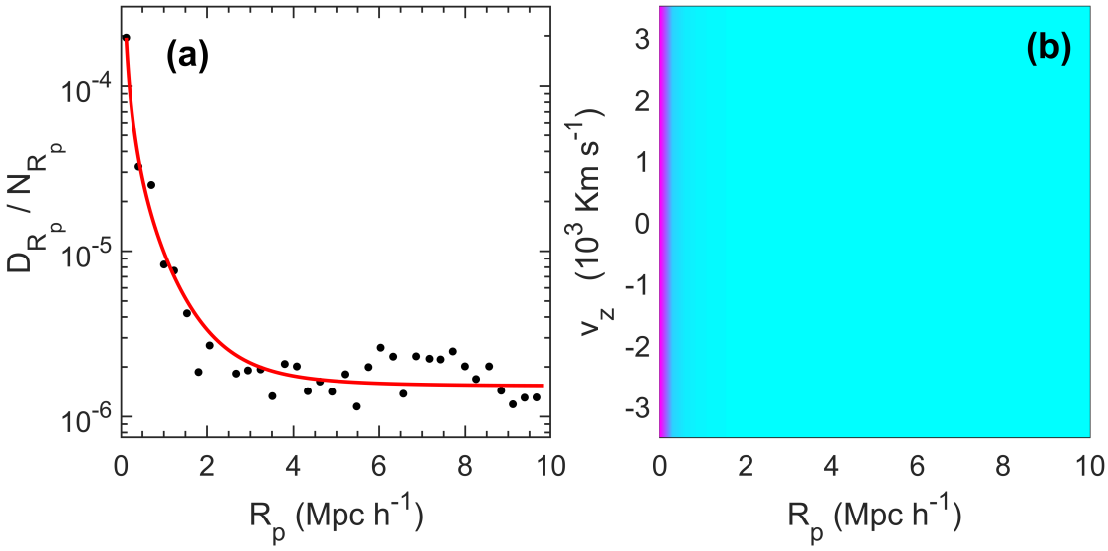

Figure 2.2: Weighting function along projected radius R_p for the simulated cluster of mass 9.37×10^{14} h^{-1} $M_\odot$ selected from Bolshoi (see § 2.3.1 A.1). The left panel (a) shows the function $\mathcal{D}_{R_p}$ derived from the data (black points, Equation (2.1)), normalized by Equation (2.2), and fitted by $\mathcal{W}_{R_p}$ (red curve, Equation (2.4)). The right panel (b) presents its corresponding probability density function in phase-space diagram. As shown in (a & b), the weighting is greatest at $R_p = 0$ and decreases outwards.

the product of Figure 2.2b and Figure 2.3b) is calculated from the surface number density $\Sigma(R_p)$, velocity dispersion $\sigma_{v_z}(R_p)$, and standard deviation $\sigma_{R_p}(v_z)$ profiles of the cluster. The phase-space weight (see § 2.3.1 part B and Figure 2.4b) is calculated from the two-dimensional adaptive kernel method that estimates the probability density underlying the data and consequently identification of clumps and substructures in the phase-space (Pisani, 1996). The total weight is then calculated as the product of the dynamical and phase-space weights (see § 2.3.1 part C and Figure 2.4c). The advantage of using the total weight rather than the dynamical weight or the phase-space weight alone is discussed in § 2.3.3.

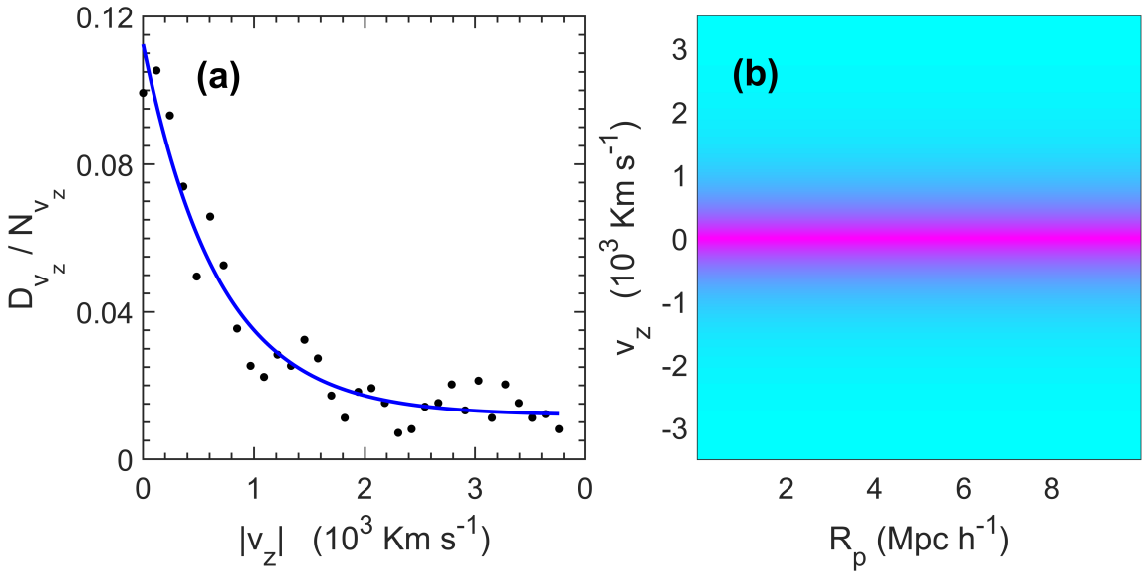

Figure 2.3: Weighting function along line-of-sight velocity v_z for the simulated cluster selected from Bolshoi. The left panel (a) shows the function $\mathcal{D}_{v_z}$ calculated from the data (black points, Equation (2.5)), normalized by Equation (2.6), and fitted by $\mathcal{W}_{v_z}$ (blue curve, Equation (2.7)). The right panel (b) presents its corresponding probability density function in phase-space. As shown in (a & b), the applied weight is greatest at $v_z = 0$ and decreases as the absolute line-of-sight velocity increases.

2.3.1 Galaxy Weighting Functions

A. Dynamical Weighting $\mathcal{W}_{dy}(R_p, v_z)$

In calculating the dynamical weighting function, we assume that the weighting we apply should be larger at the cluster center i.e., at the origin in phase-space (Figure 2.1), and decay along both the R_p and v_z phase space axes. This weighting function is, therefore, a product of two individual weighting functions; one which decays along the R_p-axis and the other along the v_z-axis as described below.

A.1. R_p-axis Weighting Function, $\mathcal{W}_{R_p}(R_p)$

In order to calculate the projected radius weighting function, $\mathcal{W}_{R_p}(R_p)$, we select two properties that are strongly correlated with projected radius and with the dynamical state of a cluster.

The first property is the **Surface Number Density Profile** $\Sigma(R_p)$, defined as the number of galaxies per unit area as a function of distance from the cluster center. It has its maximum value at the cluster center and decreases with radial distance, and is also strongly correlated with the mass distribution of the cluster. The significance of introducing $\Sigma(R_p)$ for calculating $\mathcal{W}_{R_p}$ is that the velocities of member galaxies in the core of some clusters can be as high as ≈ 3000 km s^{-1}. It produces the Kaiser or FOG effect (see Kaiser, 1987). This FOG distortion is the main reason that many membership techniques fail to correctly identify galaxies in the core with high line-of-sight velocities as members. Thus, $\Sigma(R_p)$ is essential to recover the members in the cluster core. In other words, ignoring $\Sigma(R_p)$ means missing some of the cluster members in the core.

The second property is the **Projected Velocity Dispersion Profile,** $\sigma_{v_z}(R_p)$. The significance of introducing $\sigma_{v_z}(R_p)$ for calculating $\mathcal{W}_{R_p}$ is that it characterizes the dynamical state of a cluster from its core to its infall region. Specifically, there are random motion of member galaxies in the infall region due to the presence of substructures and recent mergers (e.g., van Haarlem & van de Weygaert, 1993; Diaferio & Geller, 1997). This effect of random motion can be taken into account implicitly in $\sigma_{v_z}(R_p)$. This is the main reason why the SIM technique fails in the cluster outskirts in the projected phase-space. Thus, $\sigma_{v_z}(R_p)$ is essential to recover the members in the cluster infall region. In other words, ignoring $\sigma_{v_z}(R_p)$ means missing some of the cluster members in the infall region.

Thus, the weighting $\mathcal{W}_{R_p}(R_p)$ in the projected radius direction can be calculated by introducing the function $\mathcal{D}_{R_p}(R_p)$ that is given by

$$\mathcal{D}_{R_p}(R_p) = \frac{\Sigma(R_p)\sigma_{v_z}(R_p)}{R_p^{\nu}}, \tag{2.1}$$

with the normalization

$$\mathcal{N}_{R_p} = \int_0^{R_{p,max}} \mathcal{D}_{R_p}(R_p) dR_p, \tag{2.2}$$

where $R_{p,max}$ is the maximum projected radius in phase-space. The denominator R_p^{ν}, where the slope of the power low ν is a free parameter in the range $-1 \lesssim \nu \lesssim 1$, is introduced in Equation (2.1) to provide flexibility and generalization for the technique. The free parameter ν is selected to adjust the effect of the distortion of FOG in the core and the distortion of the random motion in the outer region. It is defined as

$$\nu = \frac{\sigma_{FOG}(R \leq 0.25)}{\sigma_{rand}(0.25 < R \leq 4))} - 1, \tag{2.3}$$

where σ_{FOG} is the velocity dispersion of the core galaxies and σ_{rand} is the velocity dispersion of the galaxies outside the core.

The function $\mathcal{D}_{R_p}(R_p)$, calculated from the data, is contaminated by interlopers that cause scattering, especially at large projected distances (see black points in the left panel of Figure 2.2). Therefore, in order to apply a smooth weighting function, we fit $\mathcal{D}_{R_p}(R_p)$ with an analytical function. Any analytical function that is a good fit to $\mathcal{D}_{R_p}(R_p)$ could be utilized. In this paper we choose to use the function

$$\mathcal{W}_{R_p}(R_p) = \mathcal{A}_0 \left(1 + \frac{R_p^2}{a^2}\right)^{\gamma} + \mathcal{A}_{bg}, \tag{2.4}$$

which has four parameters: a is a scale radius ($0 < a \lesssim 1$), γ is a slope of the power law ($-2 \lesssim \gamma < 0$), and $\mathcal{A}_0$ and $\mathcal{A}_{bg}$ are the central and background weights in the R_p-direction. These parameters are determined by applying the chi-squared algorithm using the Curve Fitting MatLab Toolbox. Note that the analytical function we selected here has the same form as the generalized King model (King, 1972; Adami et al., 1998).

Thus, the weight $\mathcal{W}_{R_p}(R_{p,i})$ of each galaxy can be calculated according to its projected radius R_p from the cluster center. The weighting along R_p is shown in Figure 2.2a, where the function $\mathcal{D}_{R_p}(R_p)$ is normalized using Equation (2.2). The data are smoothed and approximated using Equation (2.4) (shown as red line). The right panel (b) shows the projected radius weight function in phase space.

A.2. v_z-axis Weighting Function, $\mathcal{W}_{v_z}(v_z)$

In phase-space, most members are concentrated near the line $v_z = 0$ and the number of members decreases with increasing absolute line-of-sight velocity. The weighting function along v_z-axis can, therefore, be approximated by the histogram of the number of galaxies per bin, $N_{bin}(v_z)$, or equivalently the standard deviation of projected radius, $\sigma_{R_p}(v_z)$, directed along the line-of-sight velocity axis, normalized by the total number of galaxies N_{tot} in the cluster field. In other words, the weighting in the line-of-sight velocity direction can be calculated by introducing the function $\mathcal{D}_{v_z}(v_z)$ that is given by

$$\mathcal{D}_{v_z}(v_z) = \sigma_{R_p}(v_z), \tag{2.5}$$

with the normalization

$$\mathcal{N}_{v_z} = \int_{-v_{z,max}}^{v_{z,max}} \mathcal{D}_{v_z}(v_z) dv_z, \tag{2.6}$$

where $v_{z,max}$ is the maximum line-of-sight velocity of phase-space. As above, to obtain a smooth weighting function in v_z, the histogram or equivalently $\mathcal{D}_{v_z}(v_z)$ can be fitted by an analytical function. In this paper we select an exponential model that is given by

$$\mathcal{W}_{v_z}(v_z) = \mathcal{B}_0 \exp(b\ v_z) + \mathcal{B}_{bg}, \tag{2.7}$$

where $\mathcal{B}_0$ is the central weight, $\mathcal{B}_{bg}$ is the background weight in v_z and b is scale parameter ($-0.01 \lesssim b < 0$). Again, these parameters are determined by applying the chi-squared

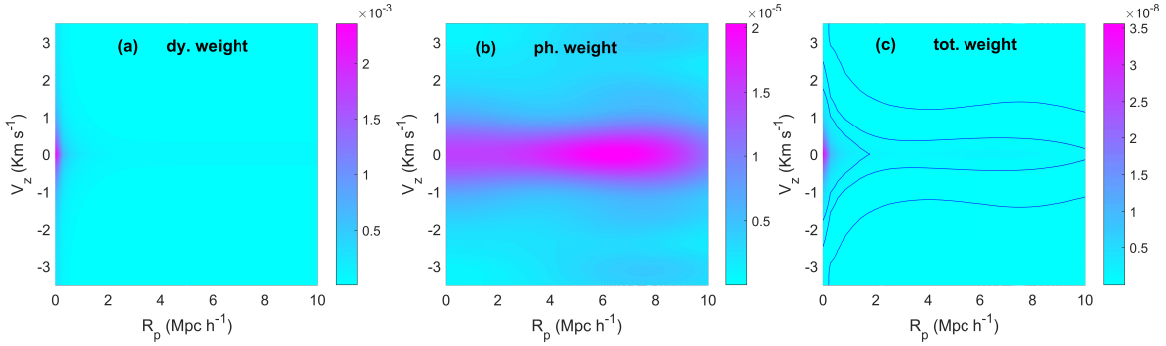

Figure 2.4: Weights to be applied as a function of position in line-of-sight velocity/projected radius phase-space for the simulated cluster selected from the Bolshoi simulation. Panel (a) shows the dynamical weight $\mathcal{W}_{dy}$ (The product of the weights shown in Figures 2.2b and 2.3b). Panel (b) presents the phase-space weight $\mathcal{W}_{ph}$ calculated from the 2DAKM. The total weight $\mathcal{W}_{tot} = \mathcal{W}_{dy} \times \mathcal{W}_{ph}$ is shown in panel (c) with explicitly drawing three contour weights. The weight $\mathcal{W}_{dy}$ is maximum at the origin (0,0) and decreases along both the R_p and v_z axes and $\mathcal{W}_{ph}$ gives higher weight for galaxy clumping around the center and substructures as well. Note that the scaling for each panel is independent, with magenta representing maximum values.

algorithm using the Curve Fitting MatLab Toolbox. The weighting along v_z, is shown in Figure 2.3a, where the function $\mathcal{D}_{v_z}(v_z)$ (black points) is normalized using Equation (2.6). The data are smoothed and approximated by Equation (2.7) for an exponential model (blue curve). The right panel (b) shows the resulting exponential-model weight as a function of location in line-of-sight velocity/projected radius phase-space. As shown in (a & b), the applied weight is greatest at $v_z = 0$ and decreases as the absolute line-of-sight velocity increases.

We can now construct a two-dimensional **dynamical weight** $\mathcal{W}_{dy}(R_p, v_z)$ by multiplying $\mathcal{W}_{R_p}(R_p)$ and $\mathcal{W}_{v_z}(v_z)$ together:

$$\mathcal{W}_{dy}(R_p, v_z) = \mathcal{W}_{R_p}(R_p)\mathcal{W}_{v_z}(v_z), \tag{2.8}$$

$\mathcal{W}_{dy}(R_p, v_z)$ is shown in the left panel of Figure 2.4, and is the product of the weights shown in Figure 2.2b and Figure 2.3b. The weight is maximum at the origin, and decreases along both R_p and v_z.

To sum up, the dynamical weight is calculated from three properties (surface number density $\Sigma(R_p)$ and velocity dispersion $\sigma_{v_z}(R_p)$ along R_p, and standard deviation of projected radius $\sigma_{R_p}(v_z)$ along v_z) which are correlated strongly with the dynamics of the cluster. This weight takes into account the effects of the FOG in the cluster core and the random motion of galaxies in the infall region.

B. Phase-Space Weighting, $\mathcal{W}_{ph}(R_p, v_z)$

This weighting is the coarse-grained phase-space density which can be simply calculated by the 2-dimensional adaptive kernel method (2DAKM, e.g., Silverman, 1986; Pisani, 1996). The kernel density estimator is the estimated probability density function of a random variable. For N galaxies with coordinates $(x, y) = (R_p, v_z)$ the density estimator is given by

$$f(x,y) = \frac{1}{N}\sum_{i=1}^{N} \frac{1}{h_{x,i}h_{y,i}} K\left(\frac{x - X_i}{h_{x,i}}\right) K\left(\frac{y - Y_i}{h_{y,i}}\right) \tag{2.9}$$

where, the kernel $K(t)$ is given by Gaussian distribution

$$K(t) = \frac{1}{\sqrt{(2\pi)}} \exp\left(-\frac{1}{2}t^2\right) \tag{2.10}$$

and $h_{j,i} = \lambda_i h_j$ is the local bandwidth, $h_j = \sigma_j N^{-1/6}$ is the fixed bandwidth for 2-dimensional space and σ_j is the standard deviation for j={x,y}. The term $\lambda_i = [\gamma / f_0(x_i, y_i)]^{0.5}$

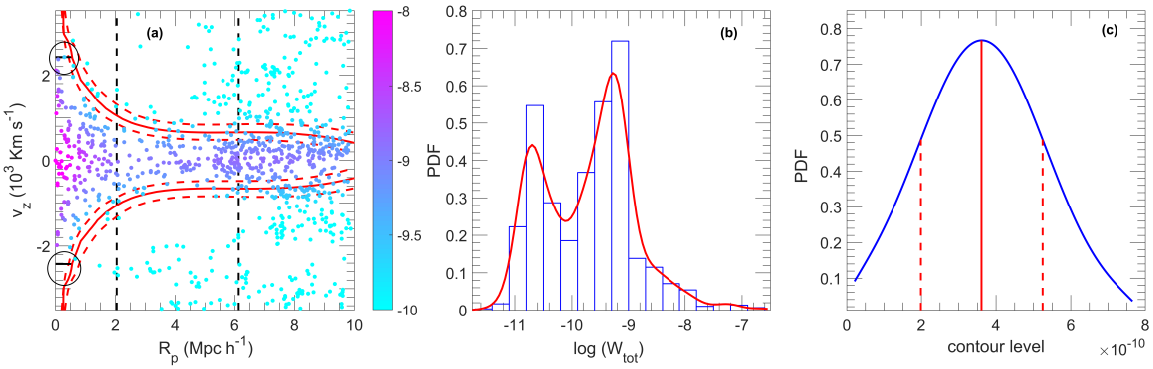

Figure 2.5: Identification of the simulated cluster membership from weighted galaxies. Panel (a) shows the weight of each galaxy in line-of-sight velocity/projected radius phase-space (magenta color indicates higher weight). Panel (b) shows a histogram or PDF of the weight applied to each galaxy, $\mathcal{W}_{tot}(R_{p,i}, v_{z,i})$. 1DAKM fitting returns a bimodal PDF in this example of the simulated cluster. We choose to use the number density method (NDM, Abdullah et al., 2013) to identify the contour weight value which separates cluster members from interlopers. This is shown by the solid red vertical line in panel (c) and solid red line in panel (a). 1σ confidence intervals are shown by the two red dashed lines. The two vertical dashed-black lines represent the virial and turnaround radii, where the cluster members are those enclosed by the best contour line and within the turnaround radius. We impose one additional cut, shown by the black solid lines in panel (a), cutting the red contour line in the very inner radius by the maximum v_z of the enclosed members.

and $\log\gamma = \sum_i \log f_0(x_i, y_i)/N$, where $f_0(x_i, y_i)$ is given by Equation 2.9 for $\lambda_i = 1$ (see also, Shimazaki & Shinomoto, 2010).

Consequently, applying 2DAKM for the distribution of galaxies in the phase-space demonstrates high weights for positions of high-density distribution of galaxies. Therefore, the main purpose of introducing the phase-space weight is to take into account the effect of the presence of any clump or substructure in the field that cannot be counted by the dynamical weight. Also, the phase-space weight is introduced to reduce the excessive increase of dynamical weight near the center (see §2.3.3). The phase-space weight $\mathcal{W}_{ph}(R_p, v_z)$ is shown in Figure 2.4b that gives more weights for galaxies in clumps and substructures, and

from the distribution of galaxies in the cluster field this weighting function is maximum around the cluster center.

C. Total Weighting, $\mathcal{W}_{tot}(R_p, v_z)$

The total weighting function is calculated as

$$\mathcal{W}_{tot}(R_p, v_z) = \mathcal{W}_{dy}(R_p, v_z)\mathcal{W}_{ph}(R_p, v_z), \tag{2.11}$$

and shown in Figure 2.4c for the simulated cluster. It shows the probability distribution function of the total weight $\mathcal{W}_{tot}(R_p, v_z)$. The weighting in Figure 2.4c is then applied to individual galaxies. Figure 2.5a shows Fig 2.1 once again, but now after applying the "total weighting". We still need to separate cluster members from interlopers. We explain how to do that in § 2.3.2.

2.3.2 Membership Determination

Figure 2.5a shows the weight of each galaxy in the simulated cluster phase-space. The question is now how to utilize the weighted galaxies in phase-space to best identify cluster members. One would like to identify a single, optimal weight value which separates cluster members from field galaxies i.e., identify the best contour weight to select in panel (a). One way is to consider the probability distribution function (PDF), or histogram of the total weight for all galaxies, which is shown in Figure 2.5b. Fitting the PDF using a 1DAKM reveals two obvious peaks (bimodal PDF). One might imagine simply drawing a vertical line to separate the members located on the right with higher weights from the interlopers located on the left. However, not all clusters show this bimodality in the PDF of

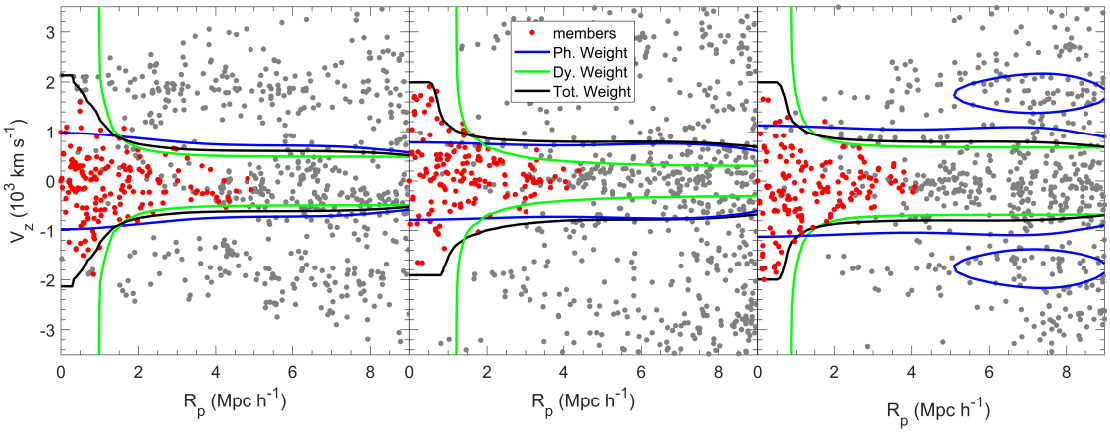

Figure 2.6: Application of dynamical, phase-space, and total weights (green, blue, and black lines, respectively) to three simulated clusters taken from the Bolshoi simulation (§ 2.2). The red points show true members within $3r_v$. Applying the dynamical weight alone (green) results in the inclusion of many galaxies within $R \sim 1$ Mpc h^{-1} with very high line-of-sight velocities. Applying the phase-space weight alone (blue), fails to recover some members in the core while simultaneously incorrectly including some interlopers at large distances due to the presence of nearby clusterings and clumps. The total weight (black), the product of the dynamical and phase-space weights, recovers true members effectively in both the core and infall regions (see Table 2.1).

$\mathcal{W}_{tot}$. Another way could be to exclude all galaxies that have weights less than, for example, 3σ from the average value of the main peak (i.e., $\mathcal{W}_{cut} = \mathcal{W}_{peak} - 3\sigma$). However, attempting to do the separation by either of these two ways is subjective.

Therefore, we prefer to select the optimal contour weight by utilizing the Number Density Method (hereafter, NDM), a technique which was introduced in Abdullah et al. (2013). The goal in applying the method here, is to find the optimal contour weight (or line) that returns the maximum number density of galaxies. In other words, we select a certain contour line (weight) and calculate its enclosed area and number of galaxies, $N_{\rm in}$ (which contribute positively), then account for the number of galaxies, $N_{\rm out}$ (which contribute negatively) located outside this contour line. Then, the number density of this

contour line can be calculated by $(N_{\rm in} - N_{\rm out})$/Area (see figure 9 in Abdullah et al., 2013).

In Figure 2.5c the PDF of the number density of galaxies calculated by NDM is plotted for weights (contour lines) in the range $-12 \leq \log \mathcal{W}_{tot} \leq -6$. The optimal contour line corresponds to the maximum number density of galaxies, the value of weight which should be utilized as the separator of cluster members from interlopers, is shown by the red vertical solid line with 1σ confidence intervals shown by the red two vertical dashed lines. This optimal contour line with 1σ confidence are shown as solid and dashed red lines in panel (a), respectively.

As shown in Figure 2.5a the optimal contour line extends to large distances ($R \sim 10\ h^{-1}$ Mpc) and not all galaxies within this boundary are members. Therefore, the last step of GalWeight is to determine a cutoff radius within which the galaxies are assumed to be bounded. Thus, the cluster members are defined as the galaxies enclosed by the optimal contour line and within the cutoff radius. This cutoff radius can be adopted as the virial radius r_v (which is the boundary of the virialized region) or the turnaround radius r_t (which is the boundary of the cluster infall region). Note that the main goal of this paper is to introduce and test the efficiency of GalWeight to recover the true members in the virial and infall regions using simulations. Thus, knowing the virial radius of each simulated cluster we test the efficiency of GalWeight at r_v, $2r_v$, and $3r_v$ projected on the phase-space diagram as described in §2.3.4 and Table 2.1 (see, e.g., Serra & Diaferio, 2013). However, for our sample of the twelve Abell clusters (observations) r_v and r_t are determined from the mass profile estimated by the virial mass estimator and NFW mass profile (Navarro et al., 1996, 1997) as discussed in §2.5.

We impose one additional cut, shown by the solid black lines highlighted by black circles in panel (a), to cut the red contour line in the very inner radius by the maximum v_z of the enclosed members. This is because in some cases the optimal contour line extends to very high velocities in the innermost region ($R \lesssim 0.25h^{-1}$ Mpc) without including any other members, so it is not necessarily to show this tail of the contour line.

The main steps in applying the GalWeight technique to determine cluster membership are summarized below:

1. Make an appropriate cut in R_p and v_z, and plot galaxies in line-of-sight velocity/projected radius phase-space. In this paper, we use $R_{p,max} = 10\ h^{-1}$ Mpc and $|v_{z,max}| = 3500$ km s^{-1}.

2. Calculate the function $\frac{\Sigma(R_p)\sigma(R_p)}{R_p^{\nu}}$ and fit it with an analytical model (e.g., Equation 2.4) to obtain $\mathcal{W}_{R_p}(R_p)$.

3. Calculate the function $\sigma_{v_z}(v_z)$ and fit it with an analytical model (e.g., Equation 2.7) to obtain $\mathcal{W}_v(v)$.

4. Determine the dynamical weighting, $\mathcal{W}_{dy}(R_p, v_z) = \mathcal{W}_{R_p}(R_p) \times \mathcal{W}_{v_z}(v_z)$.

5. Apply the 2DAKM in phase-space to determine the phase-space weighting, $\mathcal{W}_{ph}(R_p, v_z)$.

6. Calculate the total weight $\mathcal{W}_{tot}(R_p, v_z) = \mathcal{W}_{dy}(R_p, v_z) \times \mathcal{W}_{ph}(R_p, v_z)$.

7. Plot the PDF for all galaxy weights and apply a cut, retaining all galaxies with weight larger than this cut as members (NDM is used here to determine the optimal value of cut).

8. Determine the cutoff radius (r_v or r_t) using a dynamical mass estimator and identify cluster members as those enclosed by the optimal contour line and within the cutoff radius.

2.3.3 Why do we use total weight rather than dynamical or phase-space weights?

One may ask why we depend on the total weight to assign a cluster membership rather than using the dynamical weight or phase-space weight alone. We present Figure 2.6 to help answer this question. It shows the phase-space of three Bolshoi simulated clusters (see §2.2). Using simulated clusters brings the advantage that true members are known definitively. Figure 2.6 shows the optimal contour lines determined by applying, separately, the dynamical weight (green line), the phase-space weight (blue line) and the total weight (black line). The red points show true members within $3r_v$.

In Figure 2.6, the dynamical weight $\mathcal{W}_{dy}(R_p, v_z)$ (green; see also Figure 2.4a) is seen to be very smooth and idealised. In other words, $\mathcal{W}_{dy}(R_p, v_z)$ describes well an isolated galaxy cluster in phase-space. It does not take into account the effects of nearby clusters, clumps and/or substructures. Also, it shows an excessive increase near the cluster center ($\sim 1\ h^{-1}$ Mpc) and incorrectly includes interlopers near the center which have very high velocities. This effect is due to introducing $\Sigma(R_p)$ in $\mathcal{W}_{dy}(R_p, v_z)$, where the surface number density is very high near the cluster center. However, ignoring $\mathcal{W}_{dy}(R_p, v_z)$ leads to missing some cluster members especially those that close to the center in phase-space. Thus, $\mathcal{W}_{dy}(R_p, v_z)$ cannot be used on its own to assign cluster membership, but it is very important for correctly identifying members with high line-of-sight velocities.

Figure 2.6 demonstrates that, on its own, phase-space weighting $\mathcal{W}_{ph}(R_p, v_z)$ also has some difficulty in recovering true cluster members (blue; see also Figure 2.4b). This is because it does not take into account the FOG effect in the cluster core, where those

Table 2.1: Efficiency of the GalWeight technique
determined by calculating f_c and f_i at r_v, $2r_v$ and $3r_v$ for a sample of $\sim$ 3000 clusters from the MDPL2 & Bolshoi simulations.

Mass (10^{14} h^{-1} $M_\odot$)	mean	halo	f_c			f_i		
		num	r_v	$2r_v$	$3r_v$	r_v	$2r_v$	$3r_v$
(1)	(2)	(3)	(4)	(5)	(6)	(7)	(8)	(9)
MDPL2								
0.73-37.39	4.28	1500	0.993 ± 0.014	0.986 ± 0.015	0.981 ± 0.013	0.112 ± 0.035	0.096 ± 0.048	0.113 ± 0.051
0.73-2.00	1.37	253	0.998 ± 0.050	0.992 ± 0.016	0.981 ± 0.018	0.096 ± 0.039	0.098 ± 0.050	0.118 ± 0.053
2.00-4.00	3.16	617	0.993 ± 0.015	0.983 ± 0.016	0.979 ± 0.012	0.113 ± 0.034	0.099 ± 0.050	0.118 ± 0.053
4.00-8.00	5.37	484	0.989 ± 0.016	0.984 ± 0.013	0.982 ± 0.011	0.118 ± 0.032	0.099 ± 0.045	0.117 ± 0.049
8.00-37.39	11.20	146	0.988 ± 0.013	0.988 ± 0.010	0.988 ± 0.013	0.121 ± 0.028	0.105 ± 0.043	0.122 ± 0.045
Bolshoi								
0.70-10.92	1.53	1500	0.995 ± 0.011	0.981 ± 0.021	0.971 ± 0.020	0.126 ± 0.045	0.217 ± 0.109	0.226 ± 0.102
0.70-2.00	1.31	1194	0.996 ± 0.011	0.983 ± 0.021	0.972 ± 0.019	0.124 ± 0.047	0.218 ± 0.109	0.227 ± 0.102
2.00-4.00	2.70	252	0.992 ± 0.012	0.975 ± 0.023	0.967 ± 0.025	0.133 ± 0.040	0.128 ± 0.103	0.227 ± 0.105
4.00-8.00	4.43	48	0.990 ± 0.012	0.970 ± 0.022	0.961 ± 0.022	0.131 ± 0.039	0.207 ± 0.113	0.217 ± 0.103
8.00-10.92	9.68	6	0.997 ± 0.004	0.982 ± 0.024	0.973 ± 0.025	0.130 ± 0.018	0.270 ± 0.116	0.250 ± 0.094

f_c is the completeness or the fraction of the number of fiducial members identified by GalWeight as members relative to the actual number of members.

f_i is the contamination or the fraction of interlopers incorrectly assigned to be members.

Columns: (1) Cluster mass range; (2) cluster mean mass per bin; (3) the actual number of clusters per bin in simulations and the number between brackets gives the number of clusters in different orientations for Bolshoi; (4-6) and (7-9) are f_c and f_i for each mass bin at r_v, $2r_v$, and $3r_v$, respectively.

members that have high velocities do not have high concentration, so they are assigned low weights in phase-space and not counted as members. Also, the presence of nearby clusterings and substructures have the effect of widening the "optimal" contour line. Consequently, it is very difficult to separate true members from galaxies (interlopers) located in nearby clumps. This results in the inclusion of some interlopers in the infall region. In summary, using $\mathcal{W}_{ph}(R_p, v_z)$ alone, simultaneously excludes some true members near the cluster center and includes some interlopers in the infall region.

We have shown that both the dynamical weight and phase-space weight have issues in identifying true members when applied alone. However, as the black solid line in Figure 2.6 shows, the total weight (the product of the dynamical and phase-space weights), is very effective. It can simultaneously identify cluster members moving with high velocities in the core ($R_p \lesssim 1$ Mpc h^{-1}) as well as members moving with random motions in the infall regions ($R_p \sim 3r_v$).

2.3.4 Testing the Efficiency of GalWeight on MDPL & Bolshoi Simulations

To further demonstrate and quantify the GalWeight technique at assigning membership, we again utilize the MDPL2 & Bolshoi[3] simulations from the suite of MultiDark simulations. The efficiency of GalWeight can be quantified by calculating two fractions defined as follows. The first is the completeness f_c, which is the fraction of the number of fiducial members identified by GalWeight as members in the projected phase-space relative to the actual number of 3D members projected in the phase-space. The second is

[3]https://www.cosmosim.org/cms/simulations/mdpl2/

the contamination f_i, which is the fraction of interlopers incorrectly assigned to be members, projected in the phase-space (see e.g., Wojtak & Łokas, 2007; Serra & Diaferio, 2013). Ideally, of course, GalWeight would return fractions of $f_c = 1$ and $f_i = 0$.

MDPL2 provides us with 1500 simulated clusters with masses ranging from $0.73 \times 10^{14} h^{-1} M_\odot$ to $37.4 \times 10^{14} h^{-1} M_\odot$ to which we can apply GalWeight. We calculate the fractions f_c and f_i at three radii – $r_v, 2r_v$ and $3r_v$. As shown in Table 2.1, the mean values of f_c and f_i within r_v are 0.993 and 0.112 respectively for the 1500 clusters overall. Also, the fraction f_c decreases from 0.993 at r_v to 0.981 at $3r_v$.

For Bolshoi, we have about 500 clusters with masses greater than $0.70 \times 10^{14} h^{-1} M_\odot$. In order to increase the cluster sample of Bolshoi to 1500 clusters, we randomly select different line-of-sights or ordinations for each distinct halo in additional to the original line-of-sight along the z-direction (see column 3 in Table 2.1 for Bolshoi). Then, we apply GalWeight to each cluster. The mass range of the sample is $0.70 \times 10^{14} h^{-1} M_\odot$ to $10.92 \times 10^{14} h^{-1} M_\odot$ as shown in Table 2.1. The mean values of f_c and f_i within r_v are 0.995 and 0.126 respectively for the 1500 clusters overall. Also, the fraction f_c decreases from 0.995 at r_v to 0.971 at $3r_v$.

The main reason that some interlopers are assigned as members ($f_i = 0.113$ for MDPL2 and $f_i = 0.226$ for Bolshoi, as maximal value) is because of the triple-value problem (Tonry & Davis, 1981). That is, there are some foreground and background interlopers that appear to be part of the cluster body because of the distortion of phase-space. The effect of the triple-value problem is apparent in Figure 2.7 (discussed below), where most of the interlopers assigned as members are embedded in the cluster body.

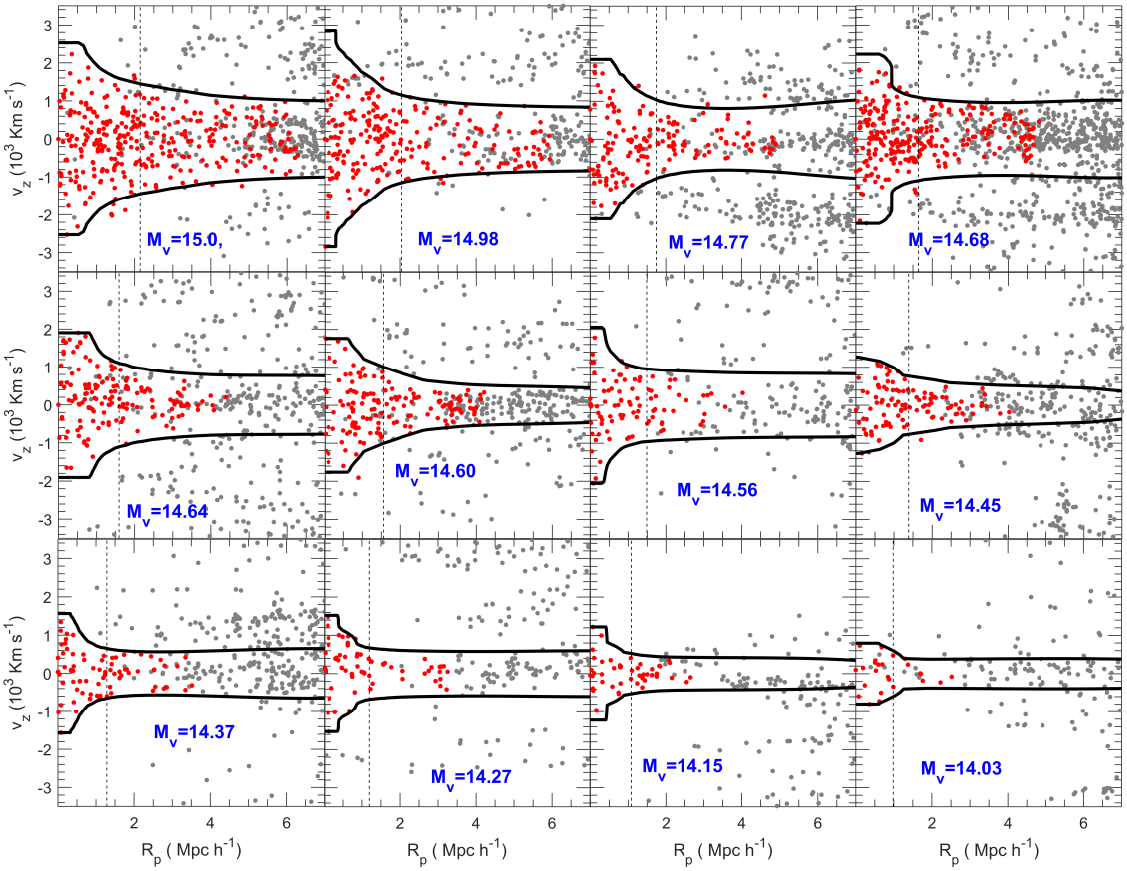

Figure 2.7: Application of the GalWeight technique (solid black lines) to twelve simulated clusters selected from the MDPL simulation (§ 2.2). Red points show fiducial members within $3r_v$. The virial mass ($\log \mathrm{M}_v\ h^{-1}\ \mathrm{M}_\odot$) and number of members within r_v is shown for each cluster. Clearly, GalWeight does well in effectively identifying members with high accuracy in both the virialized and infall regions for structures ranging in mass from rich clusters to poor groups.

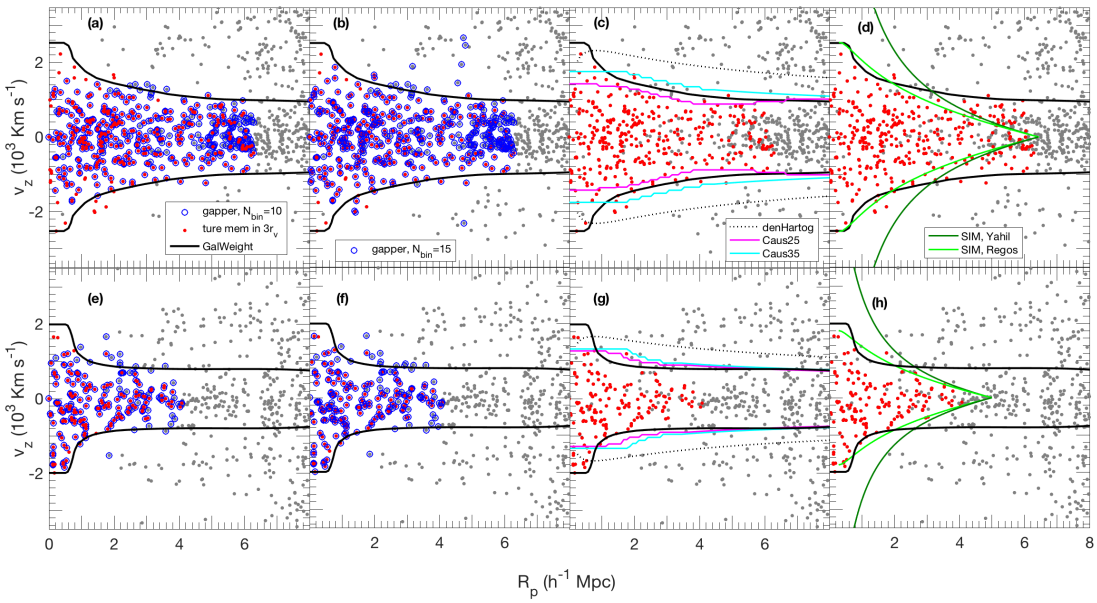

Figure 2.8: Example of four well-known membership techniques applied to two simulated clusters with mass of $10.92 \times 10^{14}\ h^{-1}\ \mathrm{M}_{\odot}$ (top panles) & $4.24 \times 10^{14}\ h^{-1}\ \mathrm{M}_{\odot}$ (bottom) from the Bolshoi simulation (§ 2.2). In each panel, the red points represent fiducial cluster members within $3r_v$, and the solid black lines show the demarcation contour enclosing cluster members, identified by applying our new technique (GalWeight). The open blue circles in panels (a, b, e & f) show members identified by the shifting gapper technique using $N_{bin} = 10$ and $N_{bin} = 15$, respectively. Panel (c & g) shows the caustic technique employing rescale parameters of q=25 (cyan lines), and q=35 (pink lines) and also the Den Hartog technique (dotted black lines). The Yahil SIM (dark green lines) and Regős SIM (light green lines) techniques are presented in panel (d & h). GalWeight recovers fiducial members with high accuracy, improving upon the shifting gapper and den Hartog techniques simultaneously at small and large projected radii, the caustic techniques at small projected radius and the SIM technique at large projected radius ($\sim 3r_v$)

.

In order to demonstrate the ability of GalWeight to assign membership in the case of both poor and massive clusters we divide the 1500 clusters (for each simulation) into four mass bins as shown in Table 2.1. The fraction f_c varies from 0.998 (0.996) for the poor clusters of mean mass 1.44×10^{14} (1.13×10^{14}) $h^{-1}M_{\odot}$ to 0.988 (0.997) for the massive clusters of mean mass 11.34×10^{14} (9.68×10^{14}) $h^{-1}M_{\odot}$ at r_v for MDPL2 (Bolshoi). We conclude that GalWeight can be applied effectively to a range of clusters masses with high efficiency.

Figure 2.7 shows examples of GalWeight being applied to twelve simulated Bolshoi clusters (solid black lines), where red and gray points show fiducial members and interlopers, respectively, within $3r_v$. The twelve clusters shown in Figure 2.7 are ranked by virial mass, with the most massive cluster (10.92×10^{14} h^{-1} $M_{\odot}$) shown in the upper left corner and the least massive one (1.06×10^{14} h^{-1} $M_{\odot}$) shown in the lower right corner. The figure demonstrates that GalWeight can effectively recover cluster membership for rich massive galaxy clusters as well as small or poor groups of galaxies with the same efficiency.

In summary, applying GalWeight to the suite of MDPL2 and Bolshoi simulations demonstrates that GalWeight can successfully recover cluster membership with high efficiency. It also further demonstrates that it can simultaneously identify members in both the virial and infall regions with taking into account the FOG effect and the random motion of galaxies in the infall region. Furthermore, it can be applied to both rich galaxy clusters and poor groups of galaxies with the same efficiency (see Table 2.1).

2.4 A comparison of membership techniques

In this section, we perform a general comparison between GalWeight and four other well-known techniques (**shifting gapper, caustic, den Hartog technique, and SIM**) without doing any quantitative comparison. We defer testing the efficiency of different membership techniques to recover the 3D true members of clusters and the influence of the determining their dynamical masses to a future work (see e.g., Wojtak & Łokas, 2007).

We begin by showing how each technique fares when it is applied in turn to two simulated clusters with mass of $10.92 \times 10^{14}\ h^{-1}\ \mathrm{M}_{\odot}$ & $4.24 \times 10^{14}\ h^{-1}\ \mathrm{M}_{\odot}$ from the Bolshoi simulation, shown in Figure 2.8. Making the assumption that the cluster is spherical, fiducial members are assumed to lie within three virial radii, $3r_v$, and are shown as 2D members in the phase-space (red points) in each panel of Figure 2.8. We select this radius ($3r_v$) in order to examine the ability of each technique to recover true members not only within the virial radius but also in the infall region i.e., the region of a cluster that extends from the viral radius r_v to the turnaround radius r_t, where $r_t \sim 2 - 4\ r_v$. Shown in each panel by the solid black line is the optimal choice of demarcation contour separating members and field galaxies identified by our GalWeight technique. For reasons of space we do not describe each of the four techniques (shifting gapper, den Hartog, caustic and SIM) in detail here. However, we summarize them below and refer the reader to the references for more information.

The **shifting gapper technique** (Fadda et al., 1996) works by first placing galaxies into bins according to their projected radial distance from the cluster center. The user has the freedom to choose the number of galaxies per bin which they believe is best-suited

to each application of the technique. Commonly chosen values are N_{bin} = 10 or 15. For each bin, the galaxies are sorted according to their velocities, then any galaxy separated by more than a fixed value (e.g., 1σ of the sample or 500-1000 km s^{-1}) from the previous one is considered an interloper and removed. Fadda et al. (1996) used a gap of 1000 km s^{-1} and a bin of 0.4 h^{-1} Mpc or larger, in order to have at least 15 galaxies. The open blue circles in panels **(a, e) & (b, f)** of Figure 2.8 represent the members identified by this technique, where the number of galaxies utilized per bin was N_{bin} = 10 and N_{bin} = 15, respectively. The gray points symbolize interlopers. Clearly, membership identification depends heavily upon the choice of N_{bin}, as there are many differences between the galaxies identified as members in panels **(a, e) & (b, f)**. Additionally, in both cases, some true members of the two cluster are missed, especially at small projected radius. Furthermore, the shifting gapper technique depends on the choice of the velocity gap used to remove interlopers in each bin. A choice of a high-velocity gap results in the identification of large fraction of interlopers as cluster members, while the choice of a low-velocity gap results in missing true cluster members (Aguerri et al., 2007).

The application of the **caustic technique** (e.g., Alpaslan et al., 2012; Serra & Diaferio, 2013) is shown in panels **(c & g)** of Figure 2.8 for two rescale parameters, q = 25 (cyan lines) and q = 35 (pink lines). Although this technique is quite successful when applied to the cluster outskirts, it misses some of the true members located within the core, which are the most important galaxies affecting the dynamics of the clusters. They are missed because the caustic technique does not take into account the effects of the FOG distortion. Also, the caustic technique cannot be applied to small galaxy groups.

Furthermore, applying the caustic technique is rather subjective and relies upon how the caustics can be inferred from the data (Reisenegger et al., 2000; Pearson et al., 2014). Nonetheless, it is still a powerful technique for estimating cluster masses.

The application of the **den Hartog technique** (den Hartog & Katgert, 1996) is also shown by the dotted black lines in Figure 2.8 panels **(c & g)**. This technique estimates the escape velocity as a function of distance from the cluster center by calculating the virial mass profile (see §2.5), $v_{esc}(R) = \sqrt{\frac{2GM_{vir}(R)}{R}}$, where G is the gravitational constant,. The figure demonstrates that this technique is very biased towards including many far interlopers. In addition, its application relies on assumptions of hydrostatic equilibrium and spherical symmetry.

Panels **(d & h)** in Figure 2.8 show the application of two **spherical infall models (SIMs).** The Yahil (Yahil, 1985) and Regős models (Regos & Geller, 1989) are shown by dark green and light green lines respectively. Note that, one needs to determine the mass density profile and the background mass density in order to apply the SIM technique and determine the infall velocity profile (e.g., van Haarlem & van de Weygaert, 1993). We determine the mass density profile for the simulated cluster from the NFW model (Navarro et al., 1996 & 1997, Equations (2.15 & 2.16), knowing its concentration c, virial radius r_v, and scale radius $r_s = r_v/C$. Also, the background mass density is given by $\rho_{bg} = \Omega_m \ \rho_c$.

As shown in Figure 2.8 (d & h), SIMs have difficulty identifying true members in the infall region in projected phase-space. This is due to the fact that the effect of random motion of galaxies in the infall regions (van Haarlem & van de Weygaert, 1993; Diaferio, 1999) causes some members in the cluster outskirts to be missed. A recent investigation by

our own team (Abdullah et al., 2013) has shown that SIMs can successfully be applied to sliced phase-space by taking into account some kinds of distortions such as the transverse motion of galaxies with respect to the observer and/or rotational motions of galaxies inside the cluster. However, this is out of the scope of the current paper.

2.5 Observations - Application to a Sample of 12 Abell Clusters

In this section we apply GalWeight to a sample of twelve Abell galaxy clusters, with galaxy coordinates and redshifts taken from SDSS-DR12[4] (hereafter, SDSS-DR12 Alam et al., 2015). In order to demonstrate the technique for both massive and poor clusters, we selected clusters with Abell richness parameter ranging from 0 to 3 (Abell et al., 1989). We deliberately selected some clusters which were almost isolated and others which had clumps or groups of galaxies nearby in order to demonstrate how the technique performs under these different scenarios. We apply the GalWeight technique only to this pilot sample of twelve clusters in this paper, deferring application to the entire SDSS-DR13 sample of ~ 800 clusters to a later paper.

The data sample is collected as follows. The NASA/IPAC Extragalactic Database (NED)[5] provides us with a first approximation of the angular coordinates and redshift of the center of our cluster sample (α_c, δ_c, z_c). We then download the coordinates and redshifts (right ascension α, declination δ, and spectroscopic redshift z) for objects classified as galaxies near the center of each cluster from SDSS-DR12 (Alam et al., 2015). The next

[4]https://http://www.sdss.org/dr12
[5]https://ned.ipac.caltech.edu

step is to apply the binary tree algorithm (e.g., Serra et al., 2011) to accurately determine the cluster center (α_c, δ_c, z_c) and create a line-of-sight velocity (v_z) versus projected radius (R_p) phase-space diagram. R_p is the projected radius from the cluster center and v_z is the line-of-sight velocity of a galaxy in the cluster frame, calculated as $v_z = c(z - z_c)/(1 + z_c)$, where z is the observed spectroscopic redshift of the galaxy and z_c is the cluster redshift. The term $(1 + z_c)$ is a correction due to the global Hubble expansion (Danese et al., 1980) and c is the speed of light.

We then apply GalWeight to the twelve Abell clusters as described in detail in § 2.3 in order to get the optimal contour line. The final step is to determine the virial radius, r_v, at which $\rho = 200\rho_c$ and the turnaround radius, r_t, at which $\rho = 5.55\rho_c$ (e.g., Nagamine & Loeb, 2003; Busha et al., 2005; Dünner et al., 2006) from all galaxies located inside optimal contour line of a cluster.

In order to calculate these two radii we should first determine the cluster mass profile. The cluster mass can be estimated from the virial mass estimator and NFW mass profile (Navarro et al., 1996, 1997) as follows.

The viral mass estimator is given by

$$M(< r) = \frac{3\pi N \sum_i v_{z,i}(< r)^2}{2G \sum_{i \neq j} \frac{1}{R_{ij}}} \tag{2.12}$$

where $v_{z,i}$ is the galaxy line-of-sight velocity and R_{ij} is the projected distance between two galaxies (e.g., Limber & Mathews, 1960; Binney & Tremaine, 1987; Rines et al., 2003).

If a system extends beyond the virial radius, Equation (2.12) will overestimate the mass due to external pressure from matter outside the virialized region (The & White, 1986;

Carlberg et al., 1997; Girardi et al., 1998b). The corrected virial mass can be determined using the following expression:

$$M_v(< r) = M(< r)[1 - S(r)], \tag{2.13}$$

where $S(r)$ is a term introduced to correct for surface pressure. For an NFW density profile and for isotropic orbits (i.e. the projected, σ_v, and angular, σ_θ, velocity dispersion components of a galaxy in the cluster frame are the same, or equivalently the anisotropy parameter $\beta = 1 - \frac{\sigma_\theta^2}{\sigma_r^2} = 0$), $S(r)$ can be calculated by

$$S(r) = \left(\frac{x}{1+x}\right)^2 \left[\ln(1+x) - \frac{x}{1+x}\right]^{-1} \left[\frac{\sigma_v(r)}{\sigma(< r)}\right]^2, \tag{2.14}$$

where $x = r/r_s$, r_s is the scale radius, $\sigma(< r)$ is the integrated three-dimensional velocity dispersion within r, and $\sigma_v(r)$ is a projected velocity dispersion (e.g., Koranyi & Geller, 2000; Abdullah et al., 2011).

The mass density within a sphere of radius r introduced by NFW is given by

$$\rho(r) = \frac{\rho_s}{x\,(1+x)^2}, \tag{2.15}$$

and its corresponding mass is given by

$$M(< r) = \frac{M_s}{\ln(2) - (1/2)} \left[\ln(1+x) - \frac{x}{1+x}\right], \tag{2.16}$$

where $M_s = 4\pi\rho_s r_s^3[\ln(2) - (1/2)]$ is the mass within r_s, $\rho_s = \delta_s \rho_c$ is the characteristic

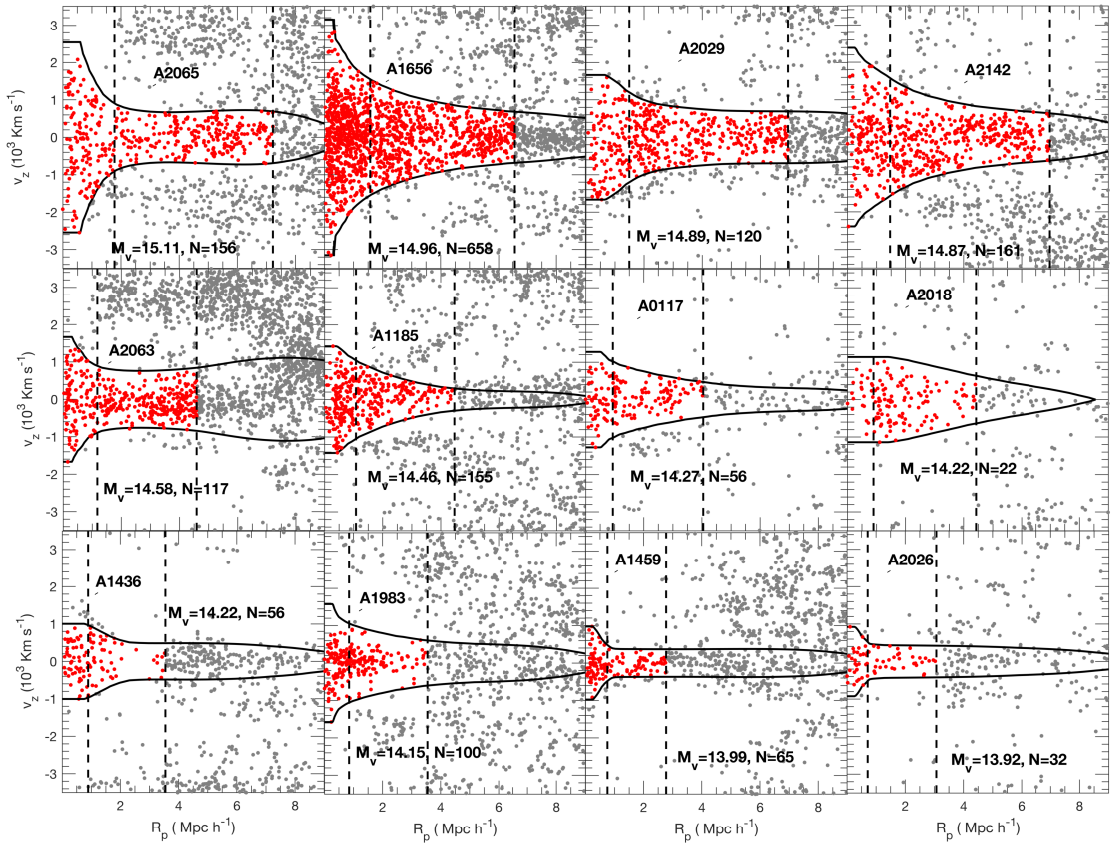

Figure 2.9: Application of the GalWeight technique to twelve Abell clusters from SDSS-DR12 (see also Table 2.2). The solid black lines shows the optimal contour line and the two dashed vertical lines show the virial and turnaround radii respectively. The red points show galaxies identified as clusters members - those enclosed by optimal contour line and r_t. Also shown in each panel is the cluster virial mass ($\log \mathrm{M}_v\ h^{-1}\ \mathrm{M}_\odot$) and number of galaxies within r_v.

density within r_s and $\delta_s = (\Delta_v/3)c^3 \left[\ln(1+c) - \frac{c}{1+c}\right]^{-1}$, and the concentration $c = r_v/r_s$ (e.g., Navarro et al., 1997; Rines et al., 2003; Mamon et al., 2013).

The projected number of galaxies within a cylinder of radius R is given by integrating the NFW profile (Equation (2.15)) along the line of sight (e.g., Bartelmann, 1996; Zenteno et al., 2016)

$$N(< R) = \frac{N_s}{\ln(2) - (1/2)} g(x), \tag{2.17}$$

where N_s is the number of galaxies within r_s that has the same formula as M_s, and $g(x)$ is given by (e.g., Golse & Kneib, 2002; Mamon & Boué, 2010)

$$g(x) = \begin{cases} \ln(x/2) + \frac{\cosh^{-1}(1/x)}{\sqrt{1-x^2}} & \text{if } x < 1 \\ 1 - \ln(2) & \text{if } x = 1 \\ \ln(x/2) + \frac{\cos^{-1}(1/x)}{\sqrt{x^2-1}} & \text{if } x > 1 \end{cases} \tag{2.18}$$

Thus, we can fit r_s for each cluster to get $S(r)$ from Equation 2.14 and calculate the corrected mass profile $M_v(r)$ from Equation 2.13. Also, the NFW mass profile is calculated from Equation 2.16. Then, r_v, at which $\Delta = 200\rho_c$, can be calculated from the viral or NFW mass profiles. While r_t, at which $\Delta = 5.55\rho_c$, can be determined from NFW mass profile only. We cannot determine r_t from the virial mass profile because the assumption of hydrostatic equilibrium is invalid.

Finally, after we calculate r_v and r_t (from NFW mass profile) the cluster membership can be defined as all galaxies enclosed by the optimal contour line and within r_t,

Table 2.2: Dynamical parameters derived for the sample of twelve Abell galaxy clusters

cluster	z_c	virial mass estimator						NFW mass estimator						NFW parameters		
		r_{500}	M_{500}	r_{200}	M_{200}	r_{100}	M_{100}	r_{500}	M_{500}	r_{200}	M_{200}	r_{100}	M_{100}	r_s	M_s	c
(1)	(2)	(3)	(4)	(5)	(6)	(7)	(8)	(9)	(10)	(11)	(12)	(13)	(14)	(15)	(16)	(17)
A2065	0.073	1.27	11.95	1.78	12.97	2.29	13.86	1.20	10.11	1.78	13.01	2.36	15.30	0.22	1.90	8.16
A1656	0.023	1.07	7.14	1.58	9.06	2.07	10.30	1.06	6.78	1.58	9.09	2.11	10.96	0.26	1.61	6.01
A2029	0.078	0.99	5.68	1.49	7.65	1.97	8.84	0.94	4.73	1.49	7.67	2.07	10.31	0.61	2.80	2.46
A2142	0.090	0.97	5.24	1.47	7.27	2.03	9.64	0.91	4.35	1.47	7.32	2.05	10.02	0.67	2.99	2.19
A2063	0.035	0.80	2.91	1.17	3.73	1.54	4.23	0.81	3.10	1.18	3.76	1.55	4.27	0.08	0.40	14.40
A1185	0.033	0.75	2.38	1.08	2.89	1.42	3.29	0.72	2.20	1.08	2.91	1.44	3.48	0.17	0.49	6.53
A0117	0.055	0.65	1.55	0.93	1.86	1.26	2.31	0.61	1.29	0.93	1.88	1.27	2.37	0.24	0.46	3.87
A2018	0.088	0.55	0.92	0.90	1.67	1.35	2.84	0.55	0.95	0.90	1.67	1.27	2.36	0.48	0.82	1.83
A1436	0.065	0.49	0.68	0.89	1.64	1.25	2.27	0.61	1.29	0.89	1.64	1.18	1.92	0.10	0.23	8.68
A1983	0.045	0.58	1.09	0.85	1.39	1.09	1.51	0.57	1.03	0.85	1.41	1.14	1.71	0.16	0.27	5.37
A1459	0.020	0.50	0.73	0.72	0.85	0.92	0.89	0.50	0.73	0.72	0.87	0.95	0.97	0.04	0.08	18.4
A2026	0.091	0.46	0.54	0.71	0.82	0.91	0.88	0.47	0.59	0.71	0.83	0.96	1.03	0.16	0.19	4.32

Radii and their masses are calculated by virial and NFW mass estimators at overdensities of $\Delta = 500$, 200 and 100 ρ_c. The radius and mass are in units of h^{-1}Mpc and 10^{14} $h^{-1}\mathrm{M}_\odot$.

Columns: (1) cluster name; (2) cluster redshift; (3-4), (5-6) & (7-8) are radii and their corresponding masses calculated bythe virial mass estimator at overdensities of $\Delta = 500, 200$ and 100, respectively. (9-10), (11-12) & (13-14) are radii and their corresponding masses calculated by an NFW model at overdensities of $\Delta = 500, 200$ and 100, respectively. (15-17) are scale radius, its corresponding scale mass and concentration of NFW parameters.

as shown by the red points in Figure 2.9. It is worth noting once again that GalWeight is effective at taking into account the effects of the FOG distortion in the innermost regions and the random motion of galaxies in the cluster infall region. Moreover, GalWeight is not affected by the presence of substructures or nearby clusters or groups as demonstrated, for example, for A2063 & A2065. Furthermore, GalWeight can be applied both to rich clusters such as A2065 & A1656 and to poor galaxy groups such as A1459 & A2026.

In order to compare our results with the literature, we calculate the radii and their corresponding masses at three overdensities, $\Delta_{500} = 500\rho_c$, $\Delta_{200} = 200\rho_c$ and $\Delta_{100} = 100\rho_c$ as shown in Table 2.2. The sample is displayed in order of decreasing NFW M_{200} mass. A complete list of NFW parameters is also provided in Table 2.2.

In Table 2.3 we list ratios of radii and masses for each of the twelve Abell clusters using our GalWeight-determined method (assuming an NFW profile) divided by previously-published values, (r_{NFW}/r_{ref}) and (M_{NFW}/M_{ref}) respectively, at overdensities of $\Delta = 500$, 200 and $100\rho_c$. Column 8 of Table 2.3 also lists the ratio of GalWeight-determined masses relative to those estimated from the caustic technique (Rines et al., 2016), $(M_{NFW}/M_{caus})_{200}$, at $\Delta = 200\rho_c$. Table 2.3 clearly shows that the radii and masses estimated for a cluster are strongly dependent on the technique used to assign membership and remove interlopers (see Wojtak & Łokas, 2007). The ratio (r_{NFW}/r_{ref}) ranges between 0.63 and 1.55, while the ratio (M_{NFW}/M_{ref}) ranges between 0.58 and 2.18.

The cluster masses from the literature tabulated in Table 2.3 have been calculated in various ways. Below, we explicitly compare our values to those obtained from applying the shifting gapper, SIM and caustic methods.

Table 2.3: GalWeight-determined ratios of radii and mass for each of the twelve Abell clusters compared to previously-published values

cluster	(r_{NFW}/r_{ref})			(M_{NFW}/M_{ref})			$(M_{NFW}/M_{caus})_{200}$
(1)	(2) Δ_{500}	(3) Δ_{200}	(4) Δ_{100}	(5) Δ_{500}	(6) Δ_{200}	(7) Δ_{100}	(8) Rines et al. (2016)
A2065	1.70^{5}, 1.15^{8}	1.04^{8}, 1.11^{11}	—	1.50^{8}	1.12^{8}, 1.30^{11}	—	3.84
A1656	1.16^{5}	0.89^{4}, 1.05^{9}	1.04^{6}	1.09^{5}	0.72^{4}, $1.16^{9,+}$	1.12^{6}	2.02
A2029	1.05^{5}, 0.93^{8}	0.93^{8}, 0.89^{11}	—	0.92^{5}, 0.80^{8}	0.82^{8}, 0.88^{11}	—	1.42
A2142	0.91^{8}, $1.30^{10,+}$	$1.30^{10,+}$, 0.94^{11}	0.96^{12}	0.66^{8}	$1.80^{10,+}$, 0.75^{11}	0.86^{12}	2.27
A2063	1.30^{8}	1.18^{8}	1.05^{12}	2.18^{8}	1.65^{8}	1.03^{12}	1.40
A1185	—	$1.01^{3,\bullet}$	—	—	$2.77^{3,\bullet}$	—	1.37
A0117	—	$0.83^{1,\star}$, 1.05^{2}	—	—	$0.58^{1,\star}$	—	—
A2018	—	0.82^{2}, 1.18^{13}	—	—	—	—	0.94
A1983	0.85^{7}	$0.90^{3,\bullet}$, 0.81^{7}	—	1.18^{7}	$0.99^{3,\bullet}$,1.03^{7}	—	1.64
A1436	$1.55^{10,+}$	$0.64^{1,\star}$, $1.24^{10,+}$	—	—	$0.64^{1,\star}$, $1.30^{10,+}$	—	—
A1459	—	$0.94^{1,\star}$	—	—	$0.84^{1,\star}$	—	—
A2026	—	0.63^{2}	—	—	—	—	—

Columns: (1) cluster name; (2-4) ratio of GalWeight radii to those in the literature at overdensities of $\Delta = 500$, 200 and 100 ρ_c respectively, assuming an NFW model. (5-7) ratio of GalWeight masses to those in the literature at overdensities of $\Delta = 500$, 200 and 100 ρ_c respectively, assuming an NFW model. (8) ratio of GalWeight masses assuming an NFW model to those calculated from the caustic technique in Rines et al. (2016) at $\Delta = 200$ ρ_c .
1=Abdullah et al. (2011), 2=Aguerri et al. (2007), 3=Girardi et al. (2002), 4=Kubo et al. (2007), 5=Laganá et al. (2011), 6=Łokas & Mamon (2003), 7=Pointecouteau et al. (2005), 8=Reiprich & Böhringer (2002), 9=Rines et al. (2003), 10=Rines & Diaferio (2006), 11=Sifón et al. (2015), 12=Wojtak & Łokas (2010). $^{+}$ (caustic technique), $^{\bullet}$ (shifting gapper),* (SIM).

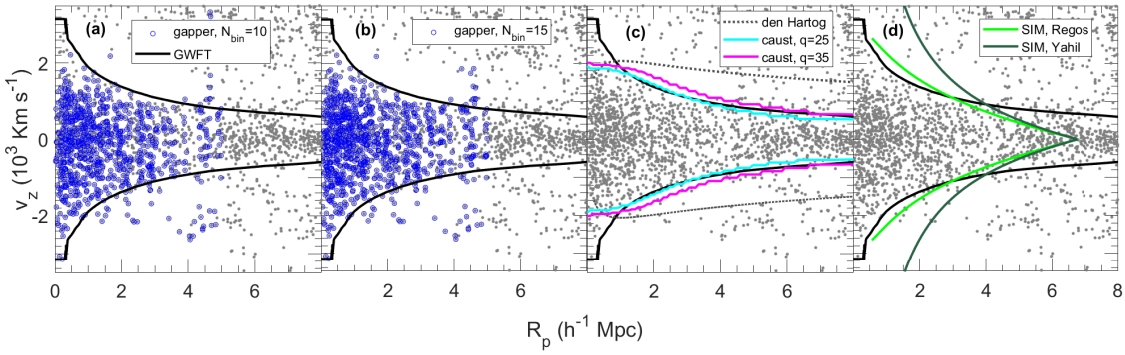

Figure 2.10: Example of four well-known membership techniques applied to the cluster. The blue open symbols and solid lines are as in Figure 2.8. Clearly GalWeight (solid black lines) appears to identify cluster members well both in the virialized and infall regions of phase-space.

First, comparing to the shifting gapper technique (see ($^\bullet$) in Table 2.3, Girardi et al., 2002; Sifón et al., 2015), we find that the ratio (M_{NFW}/M_{ref}) is larger than unity in some cases (A2065, A1185) and smaller than unity in others (A2029, A2142). This is because members assigned by this technique, and consequently the mass calculated, depend on the selection criteria of number of galaxies and velocity gap per bin. As discussed before, the choice of a high-velocity gap includes more members and consequently larger mass and vice versa.

Second, comparing to the SIM method (see (*) in Table 2.3, Abdullah et al., 2011) we note that the mass ratio (M_{NFW}/M_{ref}) is less than unity for the three clusters A0117, A1436 and A1459. This is because SIM includes more galaxy members inside the virial region even though they are very far from the cluster body. This is due to the assumption of conservation of mass that influences on the validity of SIM in the innermost region (see Figure 6 in Abdullah et al., 2011).

Third, comparing to the caustic technique (see ($^+$) in Table 2.3, Rines et al., 2003; Rines & Diaferio, 2006; Rines et al., 2016) we specifically calculate the ratio $(M_{NFW}/M_{caus})_{200}$ as listed in Table 2.3, column 8. It demonstrates that this ratio is larger than unity for 7 clusters with the highest ratio is for A2065, for which the estimated mass from NFW is four times that expected from the caustic technique. As described above, the main reason for this discrepancy is that the caustic technique does not take into consideration the effect of FOG. Thus, it misses more members inside the virial region and consequently expects lower masses.

We compare again GalWeight with the four well-known techniques (shifting gapper, caustic, den Hartog, and SIM) for the Coma cluster as shown in Figure 2.10. The Figure (see also Figure 2.8) demonstrates that the GalWeight performs very favorably against established methods, taking into account as it does the effects of the FOG distortion at small projected radius well as the random motion of galaxies in the infall region. In order to apply SIM to the Coma cluster the spatial number density profile is calculated from the NFW model (Navarro et al., 1996, 1997). Also, we assume that the background number density $\rho_{bg} = 0.0106\ h^3\ \mathrm{Mpc}^{-3}$ which is calculated using the parameters of Schechter luminosity function ($\phi^* = 0.0149\ h^3\ \mathrm{Mpc}^{-3}$, $\mathrm{M}^* - 5\log h = -20.44$ and $\alpha = -1.05$ for r magnitude, Blanton et al., 2003).

Because of the presence of interlopers, estimates of cluster mass tend to be biased too high and estimates of cluster concentration tend to be biased too low. Our work suggests that applying GalWeight rather than another technique to determine cluster membership before applying a dynamical mass estimator (virial theorem, NFW model etc.), likely results

in a more accurate estimate of the true cluster mass and concentration. In a future work we will compare the efficiency of different membership techniques to assign membership and their influence on estimating cluster mass using different mass estimators.

2.6 Discussion and Conclusion

In this paper we introduced the Galaxy Weighting Function Technique (GalWeight), a powerful new technique for identifying cluster members. specifically designed to simultaneously maximize the number of *bona fide* cluster members while minimizing the number of contaminating interlopers.

GalWeight takes into account the causes of different distortions in phase-space diagram and is independent of statistical or selection criteria. It can recover membership in both the virial and infall regions with high accuracy and is minimally affected by substructure and/or nearby clusters.

We first demonstrated GalWeight's use by applying it interactively to a simulated cluster of mass $9.37 \times 10^{14}\ h^{-1}\ \mathrm{M}_{\odot}$ selected from Bolshoi simulation. Next, we tested the efficiency of the technique on ~ 3000 clusters selected from the MDPL2 and Bolshoi simulations with masses ranging from $0.70 \times 10^{14} h^{-1} M_{\odot}$ to $37.4 \times 10^{14} h^{-1} M_{\odot}$. The completeness and interloper fractions for MDPL2 are $f_c = 0.993, 0.992$ and 0.981 and $f_i = 0.096, 0.098$ and 0.118, while for Bolshoi $f_c = 0.995, 0.981$ and 0.971 and $f_i = 0.126, 0.217$ and 0.226 within r_v, $2r_v$ and $3r_v$, respectively. We then compared its performance to four well-known existing cluster membership techniques (shifting gapper, den Hartog, caustic, SIM). Finally, we applied GalWeight to a sample of twelve Abell clusters of varying richnesses taken from

SDSS-DR12. By assuming an NFW model and applying the virial mass estimator we determined the radius and corresponding mass at overdensities of Δ_{500}, Δ_{200} and Δ_{100}. The virial mass (at Δ_{200}) of the sample ranged from $0.82 \times 10^{14}\ h^{-1}\ M_{\odot}$ to $12.97 \times 10^{14}\ h^{-1}\ M_{\odot}$, demonstrating that GalWeight is effective for poor and massive clusters. In the future we plan to apply GalWeight to a larger SDSS sample of galaxy clusters at low and high redshifts.

We believe that GalWeight has the potential for astrophysical applications far beyond the identification of cluster members e.g., identifying stellar members of nearby dwarf galaxies, or separating star-forming and quiescent galaxies. We also plan to investigate these applications in a future work.

Acknowledgement

We thank Brian Siana for useful discussions. We also thanks Gary Mamon for his useful comments on the paper. Finally, we thank the reviewer for suggestions which improved this paper. G.W. acknowledges financial support for this work from NSF grant AST-1517863 and from NASA through programs GO-13306, GO- 13677, GO-13747 & GO-13845/14327 from the Space Telescope Science Institute, which is operated by AURA, Inc., under NASA contract NAS 5-26555, and grant number 80NSSC17K0019 issued through the Astrophysics Data Analysis Program (ADAP).

Chapter 3

GalWeight Application: A publicly-available catalog of dynamical parameters of 1,800 galaxy clusters from SDSS-DR13, (GalWCat19

Utilizing the SDSS-DR13 spectroscopic dataset, we create a new publicly-available catalog of 1,800 galaxy clusters (GalWeight cluster catalog, `GalWCat19`) and a corresponding catalog of 34,471 identified member galaxies. The clusters are identified from overdensities in redshift-phase space. The GalWeight technique introduced in Abdullah, Wilson and Klypin (AWK18) is then applied to identify cluster members. The completeness of the

cluster catalog (`GalWCat19`) and the procedure followed to determine cluster mass are tested on the Bolshoi N-body simulations. The 1,800 `GalWCat19` clusters range in redshift between $0.01 - 0.2$ and in mass between $(0.4 - 14) \times 10^{14} h^{-1} M_{\odot}$. The cluster catalog provides a large number of cluster parameters including sky position, redshift, membership, velocity dispersion, and mass at overdensities $\Delta = 500, 200, 100, 5.5$. The 34,471 member galaxies are identified within the radius at which the density is 200 times the critical density of the Universe. The galaxy catalog provides the coordinates of each galaxy and the ID of the cluster that the galaxy belongs to. The cluster velocity dispersion scales with mass as $\log(\sigma_{200}) = \log(946 \pm 52 \text{ km s}^{-1}) + (0.349 \pm 0.142) \log \left[h(z)\ M_{200}/10^{15} M_{\odot}\right]$ with scatter of $\delta_{\log \sigma} = 0.06 \pm 0.04$. The catalogs are publicly available at the following website[1].

3.1 Introduction

Galaxy clusters are the most massive bound systems in the universe and are uniquely powerful cosmological probes. Cluster dynamical parameters, such as line-of-sight velocity dispersion, optical richness, and mass are closely tied to the formation and evolution of large-scale structures (Bahcall, 1988; Postman et al., 1992; Carlberg et al., 1996; Sereno & Zitrin, 2012). Catalogs of galaxy clusters provide an unlimited data source for a wide range of astrophysical and cosmological applications. In particular, the statistical study of the abundance of galaxy clusters as a function of mass and redshift (Wang & Steinhardt, 1998; Haiman et al., 2001; Reiprich & Böhringer, 2002; Battye & Weller, 2003; Dahle, 2006; Lima & Hu, 2007; Wen et al., 2010b) is a powerful tool for constraining the cosmological

[1] `https://mohamed-elhashash-94.webself.net/galwcat/`

parameters, specifically the normalization of the power spectrum σ_8 and the matter density parameter Ω_m. Catalogs of galaxy clusters are also interesting laboratories to investigate galaxy evolution under the influence of extreme environments(Butcher & Oemler, 1978; Dressler, 1980; Goto et al., 2003; Leauthaud et al., 2012; Bayliss et al., 2016; Foltz et al., 2018). Moreover, they can be utilized to study the galaxy-halo connection which correlates galaxy growth with halo growth (e.g., Wechsler & Tinker, 2018).

Galaxy clusters can be detected based on a number of different properties, such as X-ray emission from hot intracluster gas (e.g., Sarazin, 1988; Reichardt et al., 2013), the Sunyaev-Zeldovich (SZ) effect (Planck Collaboration et al., 2011), optical (e.g., Abell et al., 1989; den Hartog & Katgert, 1996; Abdullah et al., 2011) and infrared emissions (e.g., Genzel & Cesarsky, 2000; Muzzin et al., 2009; Wilson et al., 2009; Wylezalek et al., 2014) from stars in cluster members, Stellar Bump Sequence (Muzzin et al., 2013), and the gravitational lensing (e.g., Metzler et al., 1999; Kubo et al., 2009). Using current capabilities, both X-ray emission and SZ effect are detectable only for the very deep gravitational potential wells of the most massive systems. They cannot be used to detect the outskirts of massive clusters, or intermediate/low-mass clusters. Thus, current optical surveys of galaxies, such as SDSS, and upcoming surveys such as Euclid (Amendola et al., 2013), and LSST (LSST Science Collaboration et al., 2009) are required in order to produce the largest and most complete cluster sample.

Among the most popular applications of galaxy cluster catalogs are scaling relations. Scaling relations of clusters provide insight into the nature of cluster assembly and how the implementation of baryonic physics in simulations affects such relations. Studying

these relations for local clusters is also crucial for high-z cluster studies to constrain dark energy (e.g., Majumdar & Mohr, 2004). Cluster mass is not a directly observable quantity. It can be calculated in several ways such as, the caustic technique (Diaferio, 1999), the projected mass estimator (e.g, Bahcall & Tremaine, 1981), the virial mass estimator (e.g., Binney & Tremaine, 1987), weak gravitational lensing (Wilson et al., 1996; Holhjem et al., 2009), and application of Jeans equation for the gas density calculated from the x-ray analysis of galaxy cluster (Sarazin, 1988). However, these methods are observationally expensive to perform, requiring high quality datasets, and are biased due to the assumptions that have to be made (e.g. spherical symmetry, hydrostatic equilibrium, and galaxies as tracers of the underlying mass distribution). Fortunately, the cluster mass can be still indirectly inferred from other observables, the so-called mass proxies, which scale tightly with cluster mass. Among these mass proxies are X-ray luminosity, temperature, the product of X-ray temperature and gas mass (e.g. Vikhlinin et al., 2009b; Pratt et al., 2009; Mantz et al., 2016), optical luminosity or richness (e.g. Yee & Ellingson, 2003; Simet et al., 2017), and the velocity dispersion of member galaxies (e.g. Biviano et al., 2006; Bocquet et al., 2015).

There are many cluster finding methods which rely on optical surveys. For instance, the friends-of-friends (FoF) algorithm is the most frequently usable means for identifying groups and clusters in galaxy redshift data (Turner & Gott, 1976; Press & Davis, 1982). It uses galaxy distances derived from spectroscopic or photometric redshifts as the main basis of grouping. Another group of cluster finding methods are halo-based group finders (Yang et al., 2005, 2007; Duarte & Mamon, 2015). These methods assume some criteria to identify galaxies which belong to the same dark matter halo. An additional cluster

finding method is the red-sequence technique, which relies on galaxy colors (e.g., Gladders & Yee, 2005; Rykoff et al., 2014). This red-sequence-based technique assumes the existence of a tight red sequence for clusters, and uses only quiescent galaxies as a proxy of their host cluster environment. There are other cluster finding methods which are used in the literature, including density-field based methods (e.g., Miller et al., 2005), matched filter techniques (e.g., Kepner et al., 1999; Milkeraitis et al., 2010; Bellagamba et al., 2018), and the Voronoi-Delaunay method (e.g., Ramella et al., 2001; Pereira et al., 2017; Soares-Santos et al., 2011). These methods are capable of identifying clusters and groups of different richness ranging from a pair of galaxies to very massive clusters with hundreds of galaxies for entire surveys. However, they assume certain criteria and apply fast-run codes to construct catalogs of entire surveys. This may lead to inaccurate results for recovering the true cluster members because the proposed criteria could be suitable for only some individual clusters depending on their masses and/or dynamical status. Also, most of these methods use photometric redshift to extract cluster catalogs, leading to substantially more uncertainty in cluster membership in comparison to spectroscopically produced catalogs.

It is well-known that galaxy clusters manifest the Finger-of-God effect (FoG, see Jackson, 1972; Kaiser, 1987; Abdullah et al., 2013). This is the distortion of line-of-sight velocities of galaxies both in viral and infall regions due to the cluster potential well, i.e. galaxies peculiar motions. We introduce a simple algorithm, called FG, that identifies locations of clusters by looking for the FOG effect. Similar algorithms were introduced in the literature to identity FOG (e.g., Yoon et al., 2008; Wen et al., 2009; Tempel et al., 2018). In this paper, we aim to construct a sample of galaxy clusters using the FG identification in

the optical band using a high-quality spectroscopic dataset. In a previous work (Abdullah et al. 2018, hereafter AWK18) we introduced a new technique (GalWeight) to assign cluster membership. Galaxy clusters in this catalog are studied individually after assigning galaxy members using the GalWeight technique.

The paper introduces a catalog of 1800 galaxy clusters (hereafter, `GalWCat19`) identified from the spectroscopic dataset of the Sloan Digital Sky Survey-Data Release 13 (hereafter, SDSS-DR13[2], Albareti et al., 2017). We also provide a catalog of 34,471 cluster members. The paper is organized as follows. The data, the FG cluster finding algorithm, and membership identification using GalWeight are introduced in §3.2. In §3.3 we describe our procedure for calculating the dynamical parameters of each galaxy cluster. Testing the completeness of the catalog and the recovery of dynamical mass using simulations are discussed in §3.4. In §3.5 we describe the `GalWCat19` catalog and compare it with some previous catalogs, and introduce the velocity dispersion-mass relation. We summarize our conclusions and future work in §3.6. Throughout the paper we adopt ΛCDM with $\Omega_m = 0.3$, $\Omega_\Lambda = 0.7$, and $H_0 = 100\ h$ km s^{-1} Mpc^{-1}.

3.2 Data and clusters identification

3.2.1 SDSS sample

Using photometric and spectroscopic database from SDSS-DR13, we extract data for 704,200 galaxies. These galaxies fulfill the following set of criteria: spectroscopic detection, photometric and spectroscopic classification as a galaxy (by the automatic pipeline),

[2] `https://http://www.sdss.org/dr13`

spectroscopic redshift between 0.001 and 0.2 (with a redshift completeness > 0.7, Yang et al., 2007; Tempel et al., 2014), r-band magnitude (reddening-corrected) < 18, and the flag SpecObj.zWarning is zero for well-measured redshift. We downloaded the following parameters for each galaxy: photometric object ID, equatorial coordinates (right ascension α, declination δ), spectroscopic redshift (z), Petrosian magnitudes in the u, g, r, i and z bands, uncertainties, and extinction values based on Schlegel et al. (1998).

3.2.2 Identification of a galaxy cluster

Galaxy clusters exhibit overdensity regions of ∼2-3 orders of magnitude above the background density. One key signature of a galaxy cluster is the distortion of the peculiar velocities of its core members (within ~ 0.5 Mpc from the cluster center) along the line-of-sight. This distortion of FOG appears clearly in a line-of-sight velocity (v_z) versus projected radius (R_p) phase-space diagram. Here R_p is the projected radius from the cluster center. While, v_z is the line-of-sight velocity of a galaxy in the cluster frame, calculated as $v_z = (v_{obs} - v_c)/(1 + z_c)$, where v_{obs} is the observed spectroscopic velocity of the galaxy and z_c and v_c are the cluster redshift and velocity, respectively. The observed spectroscopic velocity is calculated as $v_{obs} = c[(z + 1)^2 - 1]/[(z + 1)^2 + 1]$ (relativistic correction). The term $(1 + z_c)$ is a correction due to the global Hubble expansion (Danese et al., 1980) and c is the speed of light. Consequently, the procedure that we follow in this investigation depends on looking for the FOG effect as described below.

1. We calculate the number density ρ_{cy} of all galaxies within a cylinder of radius $R_{cy} = 0.5h^{-1}$ Mpc (∼ the width of FOG), and height 3000 km s^{-1} (∼ the length of FOG)

centered on a galaxy i. Note that the radius of the cylinder is equivalent to angular radius $\sin(\theta_{cy}) = R_{cy}/D_{c,g}$, where the comoving distance of the galaxy $D_{c,g}$ is calculated as

$$D_{c,g} = \frac{c}{H_0} \int_0^z \frac{dz'}{\sqrt{\Omega_m(1+z)^3 + \Omega_k((1+z)^2 + \Omega_\Lambda}} \tag{3.1}$$

2. We sort all galaxies descending from highest to lowest number density with the condition that the cylinder has at least eight galaxies. This means we are aiming to detect all clusters that have at least eight galaxies within a projected distance $R_p = 0.5h^{-1}$ Mpc and velocity range = $\pm$1500 km s^{-1} from the cluster center. The completeness of the catalog is tested on an N-body simulation as described in §3.4.1.

3. Starting with the galaxy with highest number density, we apply the binary tree algorithm (e.g., Serra et al., 2011) to accurately determine a cluster center (α_c, δ_c, z_c) and a phase-space diagram.

4. We apply the GalWeight technique (see §3.2.3) to galaxies in the phase-space diagram out to maximum projected radius of $R_{p,max} = 10\ h^{-1}$ Mpc and a maximum line-of-sight velocity of $|v_{z,max}| = 3000$ km s^{-1} to identify those galaxies within the optimal contour line (see §3.2.3 and AWK18). These values are chosen to be sufficiently large to exceed both the turnaround radius (defined in §3.2.3) and the length of the FOG which is typically $\sim 7-8\ h^{-1}$ Mpc and $\sim$ 6000 km s^{-1}, respectively, for massive clusters.

5. Next, using all galaxies enclosed by the optimal contour line (see §3.2.3), we determine the dynamical parameters of each cluster in the catalog (see §3.3).

3.2.3 Membership identification: GALWEIGHT

In AWK18, we introduced GalWeight, a new technique for assigning galaxy cluster membership. AWK18 showed that GalWeight could be applied both to massive galaxy clusters and poor galaxy groups. They also showed that it is effective in identifying members both in the virial and infall regions with high efficiency.

The GalWeight technique works by assigning a weight to a galaxy i according to its position ($R_{p,i}$,$v_{z,i}$) in phase-space diagram. This weight is the product of two separate two-dimensional weights which we refer to as the **dynamical** and **phase-space** weights:

1. The dynamical weight is calculated from the surface number density $\Sigma(R_p)$, velocity dispersion $\sigma_{v_z}(R_p)$, and standard deviation $\sigma_{R_p}(v_z)$ profiles of the cluster as follows. We introduce the function

$$\mathcal{D}_{R_p}(R_p) = \frac{\Sigma(R_p)\sigma_{v_z}(R_p)}{R_p^{\nu}}, \tag{3.2}$$

with the normalization

$$\mathcal{N}_{R_p} = \int_0^{R_{p,max}} \mathcal{D}_{R_p}(R_p) dR_p, \tag{3.3}$$

where $R_{p,max}$ is the maximum projected radius in phase-space and ν is a free parameter in the range $-1 \lesssim \nu \lesssim 1$ which is introduced to adjust the effect of the distortion of FOG in the core and the distortion of the random motion in the outer region. It is defined as $\nu = \frac{\sigma_{FOG}(R \leq 0.25)}{\sigma_{rand}(0.25 < R \leq 4))} - 1$, where σ_{FOG} is the velocity dispersion of the core galaxies and σ_{rand}

is the velocity dispersion of the galaxies outside the core. Then, Equation 3.2 is fitted with the following analytical function

$$\mathcal{W}_{R_p}(R_p) = \mathcal{A}_0 \left(1 + \frac{R_p^2}{a^2}\right)^{\gamma} + \mathcal{A}_{bg}, \tag{3.4}$$

where a is a scale radius ($0 < a \lesssim 1$), γ is a slope of the power law ($-2 \lesssim \gamma < 0$), and $\mathcal{A}_0$ and $\mathcal{A}_{bg}$ are the central and background weights along the R_p-direction. Also, we define the function

$$\mathcal{D}_{v_z}(v_z) = \sigma_{R_p}(v_z), \tag{3.5}$$

with the normalization

$$\mathcal{N}_{v_z} = \int_{-v_{z,max}}^{v_{z,max}} \mathcal{D}_{v_z}(v_z) dv_z, \tag{3.6}$$

where $v_{z,max}$ is the maximum line-of-sight velocity of phase-space. Then, Equation 3.5 is fitted with the following exponential model

$$\mathcal{W}_{v_z}(v_z) = \mathcal{B}_0 \exp\left(b\ v_z\right) + \mathcal{B}_{bg}, \tag{3.7}$$

where $\mathcal{B}_0$ is the central weight, $\mathcal{B}_{bg}$ is the background weight along v_z and b is scale parameter ($-0.01 \lesssim b < 0$). Then, the two-dimensional dynamical weight is calculated as

$$\mathcal{W}_{dy}(R_p, v_z) = \mathcal{W}_{R_p}(R_p)\mathcal{W}_{v_z}(v_z), \tag{3.8}$$

2. The phase-space weight is calculated from the two-dimensional adaptive kernel method that estimates the probability density underlying the data and consequently identifies clumps and substructures in the phase-space (Silverman, 1986; Pisani, 1996).

The total weight is then calculated as the product of the dynamical and phase-space weights

$$\mathcal{W}_{tot}(R_p, v_z) = \mathcal{W}_{dy}(R_p, v_z)\mathcal{W}_{ph}(R_p, v_z), \tag{3.9}$$

The optimal total weight value (the optimal contour line) is determined by utilizing the Number Density Method (Abdullah et al., 2013) in order to separate members and interlopers. Then, we calculate the virial radius r_v (which is the boundary of the virialized region) and the turnaround radius r_t (which is the boundary of the cluster infall region) using the virial mass and NFW mass estimators (§3.3). Finally, the cluster membership are those enclosed by the optimal contour line and within the turnaround radius. The viral radius r_v is the radius within which the cluster is in hydrostatic equilibrium. It is approximately equal to the radius at which the density $\rho = \Delta_{200}\rho_c$, where ρ_c is the critical density of the Universe and $\Delta_{200} = 200$ (e.g., Carlberg et al., 1997). Therefore, we assume here that $r_v = r_{200}$. The turnaround radius r_t is the radius at which a galaxy's peculiar velocity (v_{pec}) is canceled out by the global Hubble expansion. In other words, it is the radius at which the infall velocity vanishes ($v_{inf} = v_{pec} - H\ r = 0$), which can be calculated as the radius at which $\rho = 5.55\rho_c$ (e.g., Nagamine & Loeb, 2003; Busha et al., 2005; Dünner et al., 2006).

3.3 Dynamics of galaxy clusters

For each cluster, we calculate dynamical parameters i.e., mass, virial and turnaround radii, velocity dispersion, number of spectroscopic members, and concentration as described below.

The cluster mass is estimated from the virial mass estimator (e.g., Limber & Mathews, 1960; Binney & Tremaine, 1987; Rines et al., 2003) and NFW mass profile (Navarro et al., 1996, 1997) as follows. The viral mass estimator is given by

$$M(< r) = \frac{3\pi N \sum_i v_{z,i}(< r)^2}{2G \sum_{i \neq j} \frac{1}{R_{ij}}} \tag{3.10}$$

where $v_{z,i}$ is the galaxy line-of-sight velocity and R_{ij} is the projected distance between two galaxies.

If a system extends beyond the virial radius, Equation (3.10) will overestimate the mass due to external pressure from matter outside the virialized region (The & White, 1986; Carlberg et al., 1997; Girardi et al., 1998b). The corrected virial mass is determined using the following expression:

$$M_v(< r) = M(< r)[1 - S(r)], \tag{3.11}$$

where $S(r)$ is a term introduced to correct for surface pressure. For an NFW density profile and for isotropic orbits (i.e. the projected, σ_v, and angular, σ_θ, velocity dispersion components of a galaxy in the cluster frame are the same, or equivalently the anisotropy parameter $\beta = 1 - \frac{\sigma_\theta^2}{\sigma_r^2} = 0$), $S(r)$ is calculated by

$$S(r) = \left(\frac{x}{1+x}\right)^2 \left[\ln(1+x) - \frac{x}{1+x}\right]^{-1} \left[\frac{\sigma_v(r)}{\sigma(<r)}\right]^2, \tag{3.12}$$

where $x = r/r_s$, r_s is the scale radius, $\sigma(<r)$ is the integrated three-dimensional velocity dispersion within r, and $\sigma_v(r)$ is a projected velocity dispersion (e.g., Koranyi & Geller, 2000; Abdullah et al., 2011).

The mass density within a sphere of radius r introduced by NFW is given by

$$\rho(r) = \frac{\rho_s}{x\,(1+x)^2}, \tag{3.13}$$

and its corresponding mass is given by

$$M(<r) = \frac{M_s}{\ln(2) - (1/2)} \left[\ln(1+x) - \frac{x}{1+x}\right], \tag{3.14}$$

where $M_s = 4\pi\rho_s r_s^3[\ln(2) - (1/2)]$ is the mass within r_s, $\rho_s = \delta_s\rho_c$ is the characteristic density within r_s and $\delta_s = (\Delta_v/3)c^3 \left[\ln(1+c) - \frac{c}{1+c}\right]^{-1}$, and the concentration $c = r_v/r_s$ (e.g., Navarro et al., 1997; Rines et al., 2003; Mamon et al., 2013).

The projected surface number density of galaxies is given by

$$\Sigma(<R) = 2\rho_s r_s f(x) = \frac{N_s}{\ln(2) - (1/2)} f(x), \tag{3.15}$$

where N_s is the number of galaxies within r_s that has the same formula as M_s, and $f(x)$ is given by (e.g., Golse & Kneib, 2002; Mamon & Boué, 2010)

$$f(x) = \begin{cases} \frac{1}{x^2-1}\left[1 - \frac{\cosh^{-1}(1/x)}{\sqrt{1-x^2}}\right] & \text{if } x < 1 \\ \frac{1}{3} & \text{if } x = 1 \\ \frac{1}{x^2-2}\left[1 - \frac{\cos^{-1}(1/x)}{\sqrt{x^2-1}}\right] & \text{if } x > 1 \end{cases} \tag{3.16}$$

The projected number of galaxies within a cylinder of radius R is given by integrating the NFW profile (Equation (3.13)) along the line of sight (e.g., Bartelmann, 1996; Zenteno et al., 2016)

$$N(< R) = \frac{N_s}{\ln(2) - (1/2)} g(x), \tag{3.17}$$

where $g(x)$ is given by (e.g., Golse & Kneib, 2002; Mamon & Boué, 2010)

$$g(x) = \begin{cases} \ln(x/2) + \frac{\cosh^{-1}(1/x)}{\sqrt{1-x^2}} & \text{if } x < 1 \\ 1 - \ln(2) & \text{if } x = 1 \\ \ln(x/2) + \frac{\cos^{-1}(1/x)}{\sqrt{x^2-1}} & \text{if } x > 1 \end{cases} \tag{3.18}$$

Given the projected radii of galaxies in each cluster, we fit r_s with a maximum-likelihood estimation (MLE) by finding the value of r_s that minimizes the probability

$$-\ln L = -\sum_i \ln \frac{x_i \Sigma(x_i)}{\int_0^{x_{max}} x_i \Sigma(x_i) dx} \tag{3.19}$$

where $x_{max} = R_{max}/r_s$ and R_{max} is a maximum projected radius. In practice, we search for the best value of r_s that gives minimum likelihood within $R_{max} \lesssim 3R_{200}$, where R_{200} is initially calculated from the uncorrected virial mass estimator (Equation 3.10). We

determine the uncertainty of 1σ confidence interval by $-\ln L = -\ln L_{ML} + 0.5$, where $\ln L_{ML}$ is the maximum likelihood (see e.g., Koranyi & Geller, 2000; Mamon & Boué, 2010; Mamon et al., 2013).

To summarize the procedure described above to calculate the corrected virial mass and NFW mass profile for each cluster: we first fit r_s for each cluster to get $S(r)$ (Equation 3.12); we then calculate the corrected virial mass $M_v(< r_{200})$ (Equation 3.11) at the virial radius r_{200}[3], at which $\rho = 200\rho_c$; we then calculate the NFW mass profile from Equation 3.14; finally, we determine the dynamical parameters (radius, number of members, velocity dispersion and mass) at overdensities of $\Delta = 500, 200, 100, 5.5$.

3.4 Application to Simulations

In §3.4.1 we test the completeness of the FG algorithm (see §3.2.2) using the Bolshoi N-body simulation (Klypin et al., 2016). In §3.4.2 we test the procedure described in §3.3 to recover a cluster mass using two mock catalogs recalled from Old et al. (2015). Note that the efficiency of GalWeight for assigning cluster membership has already been tested on Bolshoi & MDPL2 N-body simulations, and has been found to be $> 98\%$ accurate in correctly assigning cluster membership (see Table 1 in AWK18).

3.4.1 Catlaog Completeness as a Function of Cluster Mass and Redshift

In this section we investigate the completeness of the FG algorithm to identify locations of clusters with at least eight spectroscopic galaxies (see §3.2.2). In order to

[3]Throughout the paper we interchangeably call r_v and r_{200} for the virial radius. In practice, the virial radius at which the cluster is in hydrostatic equilibrium cannot be determined. We follow convention and assume that r_v is at $\rho = 200\rho_c$.

achieve this investigation we apply the FG algorithm to the Bolshoi[4] simulation. The Bolshoi simulation is an N-body simulation of 2048^3 particles in a box of comoving length 250 h^{-1} Mpc, mass resolution of 1.35×10^8 h^{-1} $M_\odot$, and gravitational softening length of 1 h^{-1} kpc (physical) at low redshifts. It was run using the Adaptive Refinement Tree (ART) code (Kravtsov et al., 1997). It assumes a flat ΛCDM cosmology, with cosmological parameters ($\Omega_\Lambda = 0.73$, $\Omega_m = 0.27$, $\Omega_b = 0.047$, $n = 0.95$, $\sigma_8 = 0.82$, and $h = 0.70$. Halos are identified using the Bound Density Maximum (BDM) algorithm (Klypin & Holtzman, 1997; Riebe et al., 2013), that was extensively tested (e.g., Knebe et al., 2011) which identifies local density maxima, determines a spherical cut-off for the halo with overdensity equal to 200 times the critical density of the Universe ($\rho = 200\rho_c$), and removes unbound particles from the halo boundary. Among other parameters, BDM provides a virial masses and radii. The virial mass is defined as $M_v = \frac{4}{3}\pi 200\rho_c r_v^3$ (see Bryan & Norman, 1998; Klypin et al., 2016). The halo catalogs are complete for halos with circular velocity $v_c \geq 100$ km s^{-1} (e.g., Klypin et al., 2011; Busha et al., 2011).

In order to investigate the completeness and purity of FG we construct a light-cone from Bolshoi as follows. We treat all subhalos as galaxies and assume the line-of-sight to be along the z-direction and the projection to be on the x-y plane. We calculate right ascension (α), declination (δ) and radial distance (D_c) in real-space as,

[4] https://www.cosmosim.org

$$\begin{cases} D_c = \sqrt{x^2 + y^2 + z^2} \\ \alpha = \arctan(yx) \\ \delta = \arcsin(x/d), \end{cases} \tag{3.20}$$

where x, y, and z are the co-moving coordinates along the principal axes of the simulation box.

The cosmological redshift z_{cosm} of a galaxy is determined by inverting D_c, using the distance-redshift relation for the given simulation cosmology (see Equation 3.1). The line-of-sight peculiar redshift in a cluster-frame is calculated as

$$z_{pec} = \left(\frac{x}{D_c} v_x + \frac{y}{D_c} v_y + \frac{z}{D_c} v_z \right) / c, \tag{3.21}$$

where v_x, v_y, and v_z are the peculiar velocity components and c is the speed of light.

Finally the observed redshift is calculated as

$$(1 + z_{obs}) = (1 + z_{cosm})(1 + z_{pec}) \tag{3.22}$$

For Bolshoi, we have about 791 clusters with masses $\geq 0.40 \times 10^{14} h^{-1} M_{\odot}$. We triple the number of clusters by operating the same task on the other two line-of-sights (x- and y-directions) and the other two projections (x-z, and y-z planes). We apply the FG algorithm to each light-cone. We then match the detected clusters with the true simulated ones within a radius of 1.5 h^{-1}Mpc and velocity gap of $\pm$1500 km s^{-1} (see §3.5.2).

The completeness and purity of FG are defined as (e.g., Hao et al., 2010)

$$\begin{cases} \mathcal{C}_{bin}(x) = \frac{N_{sim}^{match}(x_1 \leq x < x_2)}{N_{sim}(x_1 \leq x < x_2)} \times 100 \\ \\ \mathcal{C}_{cum}(x) = \frac{N_{sim}^{match}(x \geq x_1)}{N_{sim}(x \geq x_1)} \times 100, \end{cases} \tag{3.23}$$

$$\begin{cases} \mathcal{P}_{bin}(x) = \frac{N_{sim}^{match}(x_1 \leq x < x_2)}{N_{det}(x_1 \leq x < x_2)} \times 100 \\ \\ \mathcal{P}_{cum}(x) = \frac{N_{sim}^{match}(x \geq x_1)}{N_{det}(x \geq x_1)} \times 100, \end{cases} \tag{3.24}$$

where $\mathcal{C}_{bin}$ and $\mathcal{P}_{bin}$ are the completeness and purity between x_1 and x_2, $\mathcal{C}_{cum}$ and $\mathcal{C}_{cum}$ represent the cumulative rates, and x is a parameter that represents cluster mass or richness (number of galaxies). Here, N_{det} is the total number of clusters detected by FG, N_{sim} is the total number of simulated clusters, and N_{sim}^{match} is the number of clusters which are detected by FG and matched with the simulated clusters.

Figure 3.1.a shows the completeness of FG as a function of cluster mass for at least eight galaxies in a cylinder of radius $R_{cy} = 0.5\ h^{-1}$ Mpc and height 3000 km s^{-1} (see §3.2.2). As shown, the cumulative completeness (red line) is $\sim$ 100% for clusters with masses $M_{200} > 2 \times 10^{14}\ h^{-1} M_{\odot}$, while it drops to $\sim$ 85% for clusters with masses $M_{200} > 0.4 \times 10^{14}\ h^{-1} M_{\odot}$. Figure 3.1.b presents the completeness of FG as a function of richness (number of galaxies in the cylinder), and Figure 3.1.c shows the purity of FG.

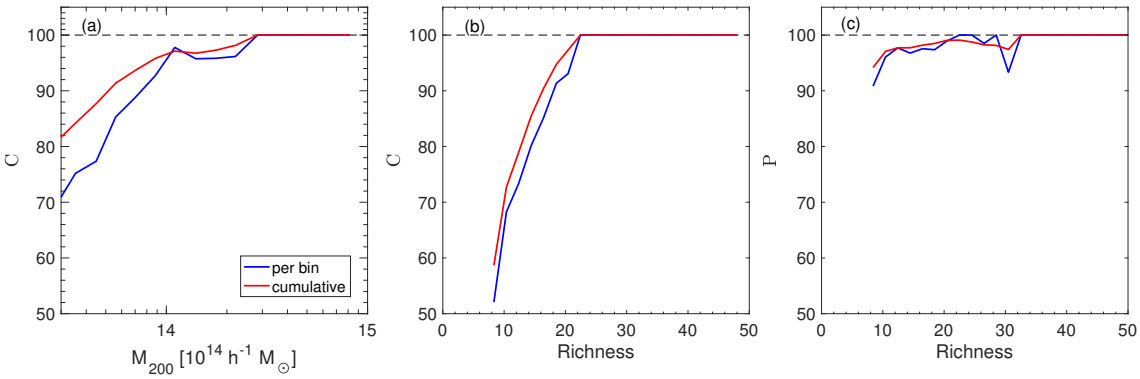

Figure 3.1: Completeness and purity of the FG algorithm. (a): completeness of FG applied to the Bolshoi clusters as a function of cluster mass for at least eight galaxies in a cylinder of radius $R_{cy} = 0.5\ h^{-1}$ Mpc and height 3000 km s^{-1} (see §3.2.2). (b): completeness of FG as a function of richness (number of galaxies in the cylinder). (c): purity of FG as a function of richness. The blue lines represent the rates per bin, and the red lines represent the cumulative rates.

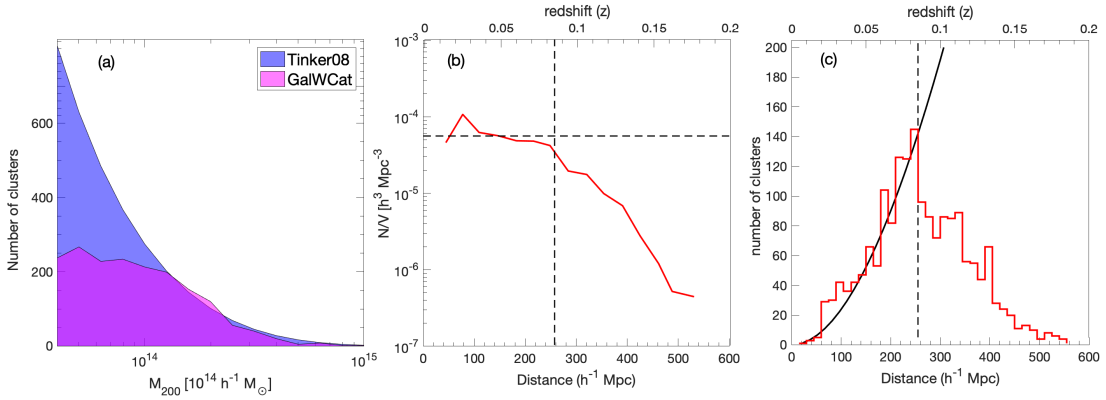

Figure 3.2: Completeness of GalWeight catalog. (a): the abundance of clusters as a function of mass for `GalWCat19` (red area) compared to the abundance of clusters predicted by Tinker et al. (2008) model (blue area). (b): cluster number density as a function of comoving distance for `GalWCat19`. The solid black line shows the number density the sample and the dashed black horizontal line represents the number density of $5.6 \times 10^{-5}\ h^3$ Mpc^{-3} averaged for the overall sample within distance $D \leq 225\ h^{-1}$. (c): number of clusters as a function of comoving distance. The dashed black line shows the expectation for a completed volume-limited sample with a density of $5.6 \times 10^{-5}\ h^3$ Mpc^{-3} for $\Omega_m = 0.3$ and $\Omega_\Lambda = 0.7$.

The completeness in mass of the GalWCat19 catalog can be investigated by calculating the abundance of clusters predicted by a theoretical model and compare it with the abundance of GalWCat19 clusters. The halo mass function (HMF), defined as the number of dark matter halos per unit mass per unit comoving volume of the universe, is given by

$$\frac{dn}{d\ln M} = f(\sigma)\frac{\rho_0}{M}\left|\frac{d\ln\sigma}{d\ln M}\right|; \tag{3.25}$$

here ρ_0 is the mean density of the universe, σ is the rms mass variance on a scale of radius R that contains mass $M = 4\pi\rho_0 R^3/3$, and $f(\sigma)$ represents the functional form that defines a particular HMF fit.

We adopt the functional form of Tinker et al. (2008) (hereafter Tinker08) to calculate the HMF and consequently the predicted abundance of clusters. For more detail about the calculation of the HMF we refer the reader to e.g., Press & Schechter (1974); Sheth et al. (2001); Jenkins et al. (2001); Warren et al. (2006); Tinker & Wetzel (2010); Behroozi et al. (2013b). The HMF is calculated using the publicly available HMFcalc [5] code (Murray et al., 2013a). We adopt the following cosmological parameters: $\Omega_m = 0.307$, $\Omega_\Lambda = 0.693$, $\sigma_8 = 0.823$, CMB temperature $T_{cmb} = 2.725K^\circ$, baryonic density $\Omega_b = 0.0486$, and spectral index $n = 0.967$ (Planck Collaboration et al., 2014), at redshift $z = 0.089$ (the mean redshift of GalWCat19).

Figure 3.2.a shows the abundance of clusters as a function of mass for GalWCat19 (red) compared to the abundance predicted by Tinker08 (blue). As shown, the GalWCat19 is complete in mass for $M_{200} \gtrsim 1 \times 10^{14}\ h^{-1}M_\odot$, while it drops off below this mass.

[5] http://hmf.icrar.org/

We also investigate the completeness of `GalWCat19` as a function of redshift or comoving distance. The left panel of Figure 3.2.b shows the number density of clusters as a function of comoving distance. The number density is almost constant within comoving distance $\sim 225h^{-1}$Mpc ($z \sim 0.088$), except for the nearby regions where the cosmic variance due to the small volume has a large effect. The number density drops catastrophically beyond $\sim 225h^{-1}$Mpc. Figure 3.2.c presents the abundance of clusters as a function of distance. Comparing the data with the expectation of a constant number density (shown as the dashed black line, $5.6 \times 10^{-5}\ h^3$ Mpc $^{-3}$) shows that `GalWCat19` is incomplete beyond $\sim 225h^{-1}$Mpc. The dependence of the number density on both the cluster mass and selection function of `GalWCat19` is investigated in detail in Abdullah et al. (2019b, in prep) which studies the cluster mass function.

3.4.2 Effectiveness of Cluster Mass Estimation

In order to test our procedure to determine cluster masses (see §3.3) we use two distinct mock catalogs utilized in Old et al. (2015, 2018) to investigate the performance of a variety of cluster mass estimation techniques. These two mock catalogs are derived from the Bolshoi DM simulation. The first mock catalog places galaxies onto the Bolshoi DM simulation by a Halo Occupation Distribution (HOD) model. The specific model in this case is referred to as HOD2, and is an updated version of the model described in Skibba et al. (2006); Skibba & Sheth (2009). The second one depends on the Semi-Analytic Galaxy Evolution (SAGE) galaxy formation model (Croton et al., 2016), which is an updated version of that described in (Croton et al., 2006). This mock catalog is referred to as SAM2. We refer the reader to Old et al. (2014, 2015) for details about constructing these catalogs.

Old et al. (2015) performed an extensive comparison of 25 galaxy-based cluster mass estimation methods using the HOD2 and SAM2 catalogs. Following Old et al. (2015), we examine the performance of our procedure to recover cluster mass by calculating the root-mean-square (rms) difference between the recovered and input log mass, defined as

$$rms = \sqrt{\frac{1}{N}\sum_{i}^{N}(\log M_{i,true} - \log M_{i,rec})^2} \tag{3.26}$$

where $M_{i,true}$ is the true mass of the cluster and $M_{i,rec}$ is its recovered or estimated mass.

We also test the performance of the procedure by calculating the scatter in the recovered mass, $\sigma_{M_{rec}}$ (delivers a measure of the intrinsic scatter), the scatter about the true mass, $\sigma_{M_{true}}$, and the bias at the pivot mass, where the pivot mass is taken as the median log mass of the input cluster sample ($\log M_{true} = 14.05$). For these three statistics, we assume a linear relationship between the recovered and true log mass (see section 4.2 in Old et al., 2015 for a full description of these statistics and, e.g., Hogg et al., 2010; Sereno & Ettori, 2015; Andreon et al., 2017).

We apply our procedure (see §3.3) on the HOD2 and SAM2 catalogs to calculate cluster mass. Figure 3.3 shows the recovered versus true cluster mass applied to the HOD2 (left) and the SAM2 (right) catalogs (see Figures 2 and 4 in Old et al., 2015 for comparison). We find that the procedure performs very well in comparison to all of the other 25 methods and results in lower values of the aforementioned statistical quantities than most of these methods for both the HOD2 and SAM2 models. Quantitatively, rms, $\sigma_{M_{rec}}$, $\sigma_{M_{true}}$, and bias are 0.24, 0.23, 0.23, and 0.06 for HOD2 and 0.32, 0.21, 0.23, and 0.24 for SAM2, respectively. These values are amongst the lowest of all the methods which calculate the

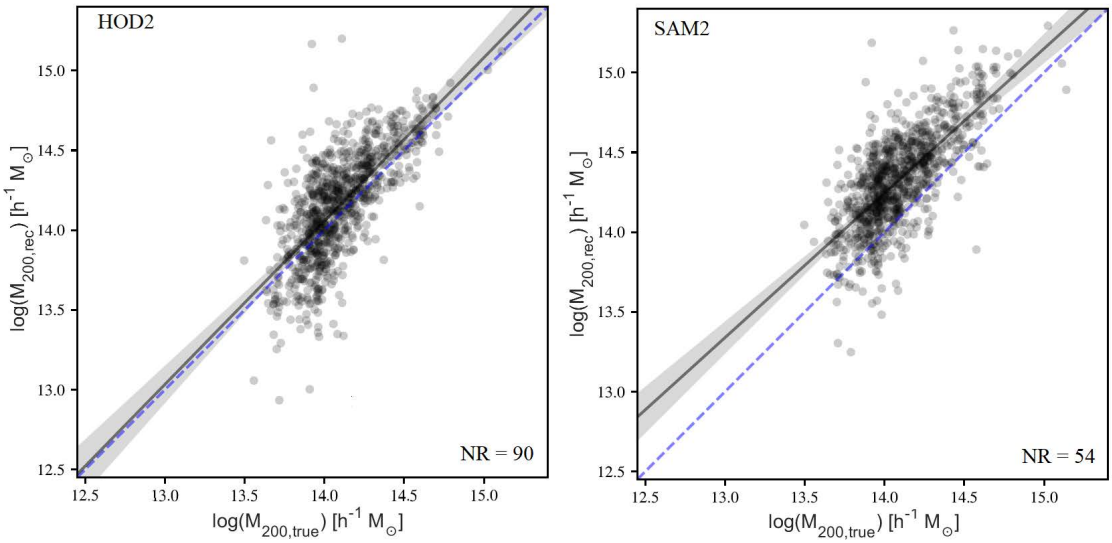

Figure 3.3: Recovered versus true cluster mass applied to the HOD2 (left) and the SAM2 (right) catalogs. The blue dashed lines represent the one-to-one relation. The solid black lines show the linear relationship between the recovered and true log mass. NR in the legend represents the number of missing clusters out of 1000 simulated clusters.

cluster mass from the galaxy velocity dispersion except for the bias calculated for SAM2 which returns a slightly higher value (see Table 2 in Old et al., 2015 for comparison). We use two different mock catalogs that have been constructed in an inherently different in the way for the purpose of observing any potential variation in mass estimation technique assessment due to assumptions made in constructing the mock catalogs.

The scatters and bias calculated above have a number of causes. Specifically, factors that introduce scatter when using the virial mass estimator include: (i) the assumption of hydrostatic equilibrium, projection effect, and possible velocity anisotropies in galaxy orbits, and the assumption that halo mass follows light (or stellar mass); (ii) presence of substructure and/or nearby structure such as cluster, supercluster, to which the cluster belongs, or filament (see e.g., The & White, 1986; Merritt, 1988; den Hartog & Katgert, 1996; Fadda et al., 1996; Girardi et al., 1998b; Abdullah et al., 2013 for more details about these

effects); (iii) presence of interlopers in the cluster frame due to the triple-value problem, for which there are some foreground and background interlopers that appear to be part of the cluster body because of the distortion of phase-space (Tonry & Davis, 1981; Abdullah et al., 2013); (iv) identification of cluster center (e.g., Girardi et al., 1998b; Zhang et al., 2019).

3.5 GalWeight cluster catalog, `GalWCat19`

3.5.1 Dynamical Parameters

As discussed in §3.2.2 we identify the location of a galaxy cluster in a cylinder of radius $R_{cy} = 0.5\ h^{-1}$ Mpc and height 3000 km s^{-1} with the condition that the cylinder has at least eight galaxies. We then apply the GalWeight technique to assign its membership (see §3.2.3). Then, using the virial mass estimator we determine the cluster virial mass assuming that the virial radius is at $\rho = 200\rho_c$ (see §3.3). Finally, we select all galaxy clusters of virial mass $M_{200} \geq 0.4 \times 10^{14}\ h^{-1}$ M$_\odot$. Following this procedure we get a catalog of 1,800 clusters with virial mass in the range $(0.40 - 14) \times 10^{14}\ h^{-1}$ M$_\odot$ and in a redshift range $0.01 \leq z \leq 0.2$. We refer to this 1,800 galaxy cluster sample as `GalWCat19`. We exclude overdensity regions (locations of galaxy clusters) for which the FOG effect is indistinct because of interactions between different clusters in these regions.

The distribution of all galaxies in the sample (black) and the cluster members identified by GalWeight and within r_v (red) and r_t (blue) are shown in Figure 3.4. The distortion of the line-of-sight velocity or the FOG effect is shown clearly for each cluster.

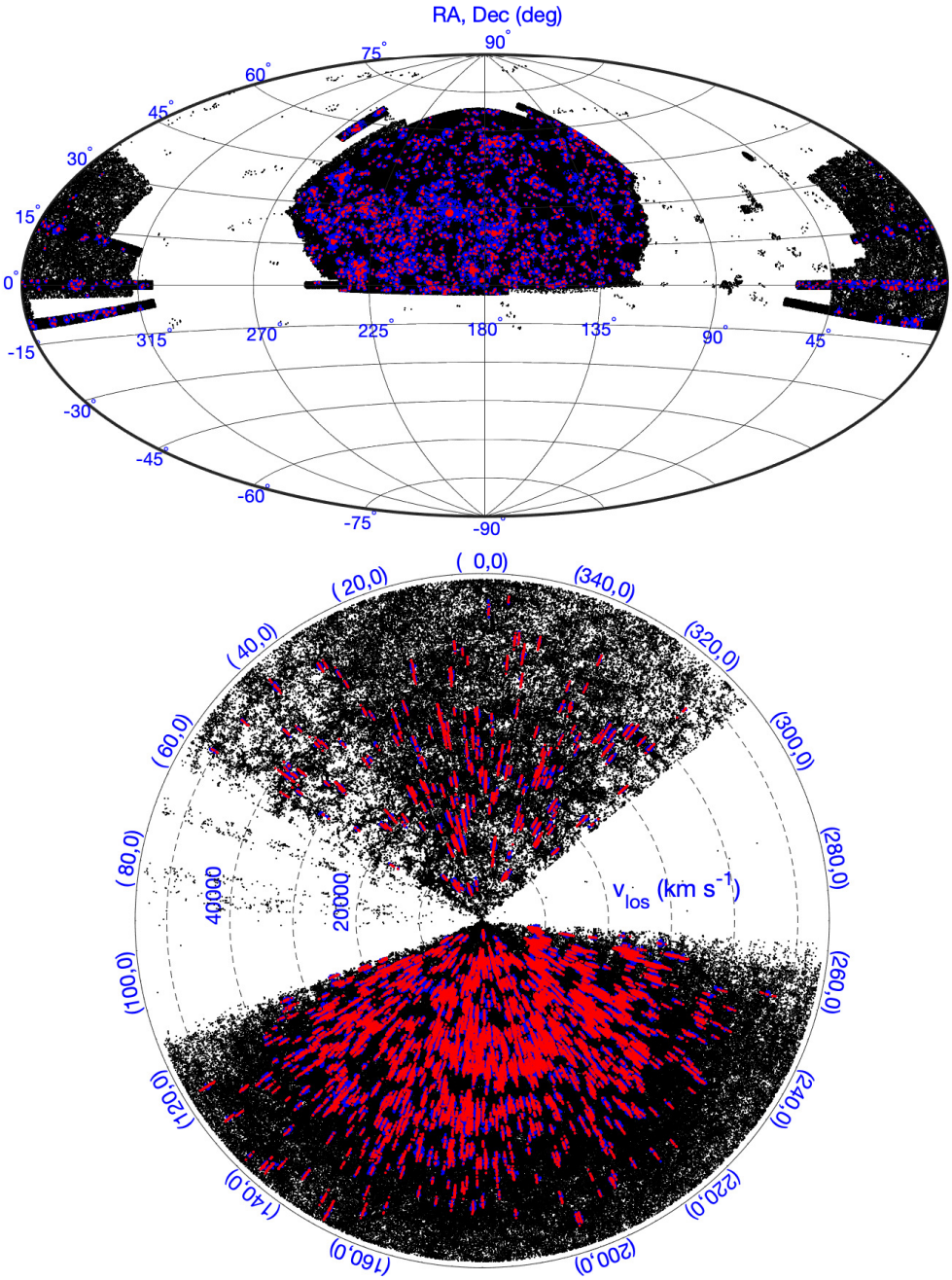

Figure 3.4: Top panel: Aitoff projection in celestial coordinates. Bottom panel: light cone diagram. The black points represent the distribution of all galaxies in the sample, while the blue and red points represent the distribution of 1,800 clusters members identified by GalWeight which are within r_{200} and $r_{5.5}$, respectively (see §3.3).

Table 3.1: Coordinates, dynamical parameters at R_{200}, and NFW parameters for the first 15 clusters in the `GalWCat19` catalog (see Appendix 3.6).

ID	α (deg)	δ (deg)	z_c	r_{200} (h^{-1} Mpc)	N_{200}	σ_{200} (km s^{-1})	M_{200} (10^{14} $h^{-1}\mathrm{M}_\odot$)	r_s (h^{-1} Mpc)	M_s (10^{14} $h^{-1}\mathrm{M}_\odot$)
(1)	(2)	(3)	(4)	(5)	(6)	(7)	(8)	(9)	(10)
01	230.7	27.74	0.0732	1.759	167	$1042^{+100.8}_{-83.23}$	13.55 ± 3.569	0.41 ± 0.108	3.061 ± 0.8063
02	227.6	33.5	0.1139	1.511	63	$926.8^{+118.7}_{-92.04}$	8.947 ± 2.349	0.32 ± 0.084	1.880 ± 0.4935
03	194.9	27.91	0.0234	1.545	672	$932.6^{+55.31}_{-47.76}$	8.757 ± 2.229	0.33 ± 0.084	1.852 ± 0.4715
04	258.2	64.05	0.0810	1.453	155	$881.2^{+82.08}_{-70.22}$	7.702 ± 2.082	0.37 ± 0.1	1.865 ± 0.5039
05	209.8	27.97	0.0751	1.449	77	$842.7^{+96.16}_{-83.23}$	7.589 ± 2.168	0.14 ± 0.04	0.966 ± 0.276
06	227.7	5.823	0.0784	1.431	128	$886.5^{+86.03}_{-71.71}$	7.332 ± 0.4412	1.13 ± 0.068	5.459 ± 0.3285
07	255.7	33.50	0.0878	1.423	84	$887.6^{+130.6}_{-95.31}$	7.281 ± 2.118	0.22 ± 0.064	1.229 ± 0.3574
08	231.0	29.89	0.1138	1.390	80	$860.2^{+99.22}_{-87.6}$	6.952 ± 1.106	0.93 ± 0.148	4.265 ± 0.6787
09	239.6	27.22	0.0898	1.379	150	$838.2^{+92.67}_{-77.16}$	6.632 ± 1.404	0.85 ± 0.18	3.709 ± 0.7855
10	240.5	15.92	0.0370	1.401	299	$771.3^{+62.73}_{-52.71}$	6.618 ± 1.655	0.16 ± 0.04	0.926 ± 0.2315
11	257.4	34.47	0.0849	1.378	93	$846.6^{+117.8}_{-92.73}$	6.583 ± 2.088	0.29 ± 0.092	1.377 ± 0.437
12	255.7	34.05	0.1002	1.340	72	$833.3^{+99.68}_{-80.46}$	6.154 ± 1.783	0.29 ± 0.084	1.314 ± 0.3807
13	2.939	32.42	0.1017	1.322	35	$861.5^{+159.5}_{-119.3}$	5.915 ± 1.577	0.15 ± 0.04	0.8245 ± 0.2199
14	53.59	-1.166	0.1381	1.272	28	$878.4^{+301.3}_{-176.4}$	5.462 ± 1.923	0.25 ± 0.088	1.087 ± 0.3827
15	358.5	-10.39	0.0766	1.284	109	$753.3^{+88.64}_{-75.14}$	5.287 ± 1.41	0.36 ± 0.096	1.384 ± 0.3691

Columns: (1) cluster ID; (2) right ascension; (3) declination; (4) redshift, (5-8) radius and its corresponding number of members, velocity dispersion and mass at overdensity of $\Delta = 200$; (9-10) scale radius and its corresponding mass of NFW model.

As discussed in §3.3 we use the virial mass estimator to determine the virial mass at the virial radius r_{200} of each cluster. Then, using NFW mass profile we determine the dynamical parameters of each cluster at overdensities of $\Delta = [500, 200, 100, 5.5]$. Note that we assume the virial radius is at $\Delta = 200$ and turnaround radius is at $\Delta = 5.5$ (see §3.3). The derived parameters for each cluster are radius, number of members, velocity dispersion and mass at each of the different overdensities, plus the NFW parameters: scale radius, mass at scale radius, and concentration $c = r_{200}/r_s$ (see Appendix 3.6). Table 3.1 shows the coordinates, dynamical parameters at at R_{200}, and NFW parameters for the first 15 clusters in the `GalWCat19` catalog.

The `GalWCat19` release consists of two catalogs. The first catalog is for the coordinates and the dynamical parameters of each galaxy cluster and the second one is for the coordinates of member galaxies belonging to each cluster. The two catalogs are described in Appendix A, and made available in their entirety at the link[6]. The uncertainty of the virial mass estimator is calculated using the limiting fractional uncertainty $\pi^{-1}(2\ \ln\ N)^{1/2}N^{-1/2}$ (Bahcall & Tremaine, 1981). Note that throughout the paper the velocity dispersion is calculated using the classical standard deviation $\sigma_v = [(n-1)]^{-1}\sum_i v_z^2$, where v_z is the line-of-sight velocity of a galaxy in the cluster frame (e.g., Munari et al., 2013; Tempel et al., 2014; Ruel et al., 2014). The uncertainty of the velocity dispersion is calculated via performing bootstrap resampling (with 1000 resamples).

[6] `https://mohamed-elhashash-94.webself.net/galwcat`

3.5.2 GalWeight Catalog Matching

Matching optical catalogs with each other depends on the cluster finding method used to extract a catalog, the kind of dataset used, the redshift range, and the identification of the cluster center. In this section we compare the `GalWCat19` catalog with previous cluster catalogs by matching them in a traditional way as performed in the literature (see e.g., Wen et al., 2012; Banerjee et al., 2018). This task is accomplished by searching within a given radius and velocity gap (or redshift) from each GalWeight cluster center. We adopt a search radius of 1.5 h^{-1}Mpc ($\sim$ twice the mean value of R_{200} in our catalog). Also, we adopt the velocity gap of $\pm$1500 km s^{-1} ($\sim$ redshift difference of 0.01). We compare `GalWCat19` with previous catalogs, including Yoon (Yoon et al., 2008), GMBCG (Hao et al., 2010), WHL (Wen et al., 2012), redMaPPer (Rykoff et al., 2014), Tempel (Tempel et al., 2014), and AMF (Banerjee et al., 2018) catalogs. Note that some catalogs provided both spectroscopic and photometric redshifts for clusters. In that case we match our catalog with each of these redshifts as shown in Table 3.2.

The procedure used to compare `GalWCat19` with other catalogs is as follows.

1. In an overlapping redshift range (z_{over}) between `GalWCat19` and the reference catalog we determine the number of clusters in `GalWCat19` (Ngw) and the corresponding number of clusters in the reference catalog ($Ncat$).

2. We calculate how many clusters match ($Nmat$) in a radius of 1.5 h^{-1} Mpc and velocity gap of $\pm$1500 km s^{-1} relative to `GalWCat19` cluster center.

3. We determine the number of clusters which are included in `GalWCat19` and are not identified by the reference catalog (Ngw_o).

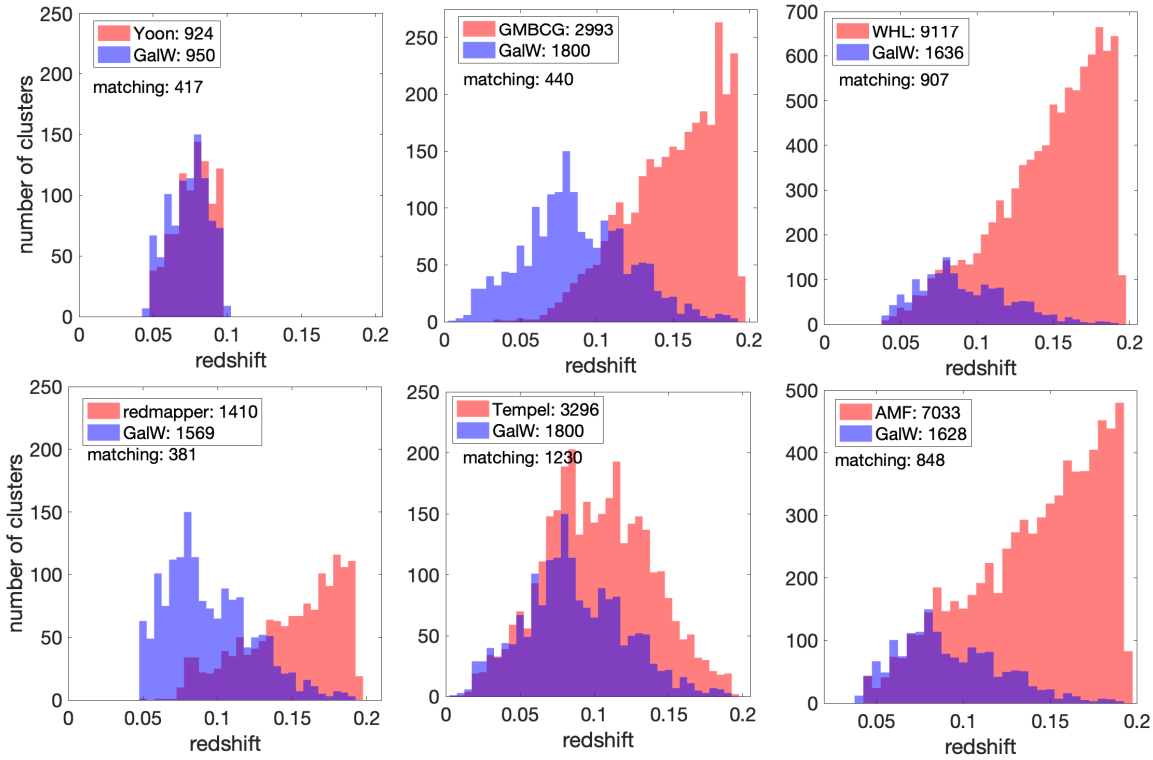

Figure 3.5: Matching `GalWCat19` (blue histograms) with six optical catalogs (red histograms). The histograms of Yoon, GMBCG, WHL, redMaPPer, and Tempel are derived from spectroscopic redshifts provided by each catalog, while the histogram of AMF is derived from photometric redshift that does not provide spectroscopic data.

4. We calculate the number of clusters which are not identified by `GalWCat19` but included in the reference catalog ($Ncat_o$).

5. We determine the number of clusters not identified by `GalWCat19` but included in the reference catalog for which there are at least 8 galaxies in a projected distance of R_p = 0.5 h^{-1} Mpc and velocity range = $\pm$1500 km s^{-1} from the cluster center ($Ncat_{o,FG}$) (the cutoff condition of our catalog).

6. Finally, the ratios $Rmat = Nmat/Ngw$, and $Rcat_{o,FG} = Ncat_{o,FG}/Ngw$ are calculated (see Table 3.2).

Table 3.2: Matches with other catalogs.

		numbers						ratios			
Catalog	z_{over}	Ngw	$Ncat$	$Nmat$	Ngw_o	$Ncat_o$	$Ncat_{o,FG}$	$Rmat$	$Rcat_{o,FG}$	z-type	reference
(1)	(2)	(3)	(4)	(5)	(6)	(7)	(8)	(9)	(10)	(11)	(12)
Yoon	0.049-0.101	950	924	417	533	507	266	**0.439**	0.280	[1]	
GMBCG	0.099-0.196	650	3677	182	468	3495	11	**0.280**	0.017	photo	[2]
GMBCG	0.007-0.196	1800	2993	440	1360	2553	97	**0.244**	0.054	spect	[2]
WHL	0.049-0.196	1580	15601	726	854	14875	82	**0.459**	0.052	photo	[3]
WHL	0.043-0.196	1636	9117	907	729	8210	294	**0.554**	0.180	spect	[3]
redMaPPer	0.079-0.196	1073	2248	429	644	1819	25	**0.400**	0.023	photo	[4]
redMaPPer	0.050-0.196	1569	1410	381	1188	1029	24	**0.243**	0.015	spect	[4]
Tempel	0.007-0.196	1800	3296	1230	570	2066	482	**0.683**	0.268	spect	[5]
AMF	0.044-0.196	1628	7033	848	780	6185	184	**0.521**	0.113	photo	[6]

Columns: (1) catalog name; (2) intersecting redshift range; (3) number of clusters in the redshift range of the catalog; (4) number of clusters in the redshift range of the GalWeight catalog; (5) number of clusters that matches with GalWeight catalog; (6) number of clusters that is included in GalWeight catalog and missed by the other catalog; (7) number of clusters that is missed by GalWeight catalog and included in the other catalog; (8) same as column (7) but for clusters that only satisfy the cutoff condition of our catalog; (9-10) the ratios $Rmat = Nmat/Ngw$, and $Rcat_{o,FG} = Ncat_{o,FG}/Ngw$; (11) the redshift type; (12) the reference of the catalog.

Reference: [1]=Yoon et al. (2008), [2]=Hao et al. (2010), [3]=Wen et al. (2012), [4]=Rykoff et al. (2014), [5]=Tempel et al. (2014), [6]= Banerjee et al. (2018).

A summary of each catalog, cluster finding method, and redshift range is descried below. We refer the reader to the reference of each catalog for more details.

1. The Yoon catalog:-

Yoon catalog is a local density cluster finder catalog (Yoon et al., 2008) applied on SDSS-DR5 using the spectroscopic and photometric redshift dataset. The catalog identified 924 clusters in a spectroscopic redshift range of $z_{sp} = [0.049, 0.101]$. The number of matched clusters is 417 out of 950 `GalWCat19` clusters in the overlapping redshift range.

2. The GMBCG catalog:-

GMBCG is a red-sequence plus brightest cluster galaxy cluster finder catalog (Hao et al., 2010) applied on SDSS-DR7 using the photometric redshift dataset. The catalog identified $\sim$ 50,000 clusters in a photometric redshift range of $z_{ph} = [0.1, 0.55]$. The catalog also provided spectroscopic redshift for 2,993 clusters in a range of $z_{sp} = [0.007, 0.196]$. There are 440 matched clusters out of 1,800 in the overlapping spectroscopic redshift range.

3. The WHL catalog:-

WHL is a red-sequence cluster finder catalog (Wen et al., 2012) applied on SDSS-DR8 using the photometric redshift (z_{ph}) dataset. The catalog identified 132,684 clusters in a photometric redshift range of $z_{ph} = [0.05, 0.785]$. The catalog provided spectroscopic redshift for 9,117 clusters in a range of $z_{sp} = [0.043, 0.196]$. The number of matched clusters is 912 out of 1695 in the overlapping spectroscopic redshift range.

4. The redMaPPer catalog:-

redMaPPer is a red-sequence cluster finder catalog (Rykoff et al., 2014) applied on SDSS-DR8 using the photometric redshift dataset. The catalog identified 25,325 clusters in a

photometric redshift range of $z_{ph} = [0.08, 0.55]$. The catalog also provided spectroscopic redshift for 1,410 clusters in a range of $z_{sp} = [0.050, 0.196]$. The number of matched clusters are 381 out of 1,569 in the overlapping spectroscopic redshift range.

5. The Tempel catalog:-

Tempel catalog is based on a modified friends-of-friends method (Tempel et al., 2014), and is applied on the spectroscopic sample of galaxies of SDSS-DR10. The catalog identified 82,458 clusters in a spectroscopic redshift range of $z_{sp} = [0.08, 0.2]$. There are 3296 clusters in the catalog with masses $\geq 0.4 \times 10^{14}\ h^{-1} M_{\odot}$ (the cutoff mass of `GalWCat19`) and number of galaxy members = 4 in R_{200}. The number of matched clusters is 1,230 out of 1800 in the spectroscopic overlapping redshift range.

6. The AMF catalog:-

AMF catalog (Banerjee et al., 2018) is based on an adaptive matched filter technique applied to SDSS-DR9. The catalog identified 46,479 galaxy clusters in a photometric redshift range of $z_{ph} = [0.045, 0.641]$. There are 7,033 clusters in the overlapping redshift $z_{ph} = [0.045, 0.196]$. The number of matched clusters is 848 out of 1,628 in the overlapping photometric redshift range.

As shown in Table 3.2, the matching rate, $Rmat = Nmat/Ngw$ varies from 0.24 to 0.68 depending on the cluster finding method used to extract a catalog, the dataset used, redshift range, and the identification of the cluster center. These are the main factors that explain why the `GalWCat19` miss clusters relative to other catalogs and vice versa. Also, we expect that our catalog miss poor or low-mass clusters. This is because we cut the catalog at cluster masses of $M_{200} \geq 0.4 \times 10^{14}\ h^{-1} M_{\odot}$ and with the condition that the

number of galaxies within a cylinder of $R_p = 0.5h^{-1}$ Mpc and velocity range = $\pm$1500 km s^{-1} is at least 8 galaxies. Moreover, for the catalogs extracted from photometric redshifts (GMBCG, WHL, redMaPPar, and AMF) the number of clusters at high redshift (~ 0.2) is huge relative to `GalWCat19` which is extracted from spectroscopic redshifts. This is because the number of galaxies (and consequently the number of clusters) that have photometric redshifts is very large relative to the spectroscopic ones. Figure 3.5 shows histograms for matching `GalWCat19` with the aforementioned six optical catalogs.

3.5.3 Velocity dispersion vs. Mass relation

Estimating cluster masses accurately is a significant challenge in astronomy, since it is not a directly observable quantity. The use of velocity dispersion as a proxy for cluster mass has been shown to be particularly effective at low redshift compared to other techniques. Sereno & Ettori (2015) showed that the intrinsic scatter in the $\sigma - M_{WL}$ relation was $\sim 14\%$ as opposed to $\sim 30\%$, $\sim 25\%$, and $\sim 40\%$ for X-ray luminosity, SZ flux, and optical richness, respectively. Also, since galaxies are nearly collisionless tracers of the gravitational potential, one expects velocity dispersion to be more robust than X-ray and SZ mass proxies.

Evrard et al. (2008) (Evrard+08) found that the $\sigma - M$ relation for dark matter particles was close to the expected virial scaling relation of $\sigma \propto M^{1/3}$, with a minimal scatter of $\sim 5\%$, and was insensitive to cosmological parameters. Munari et al. (2013) (Munari+13), Saro et al. (2013) (Saro+13), and Armitage et al. (2018) (Armitage+18) investigated the $\sigma - M$ relation using hydrodynamical and semi-analytic simulations in order to understand how

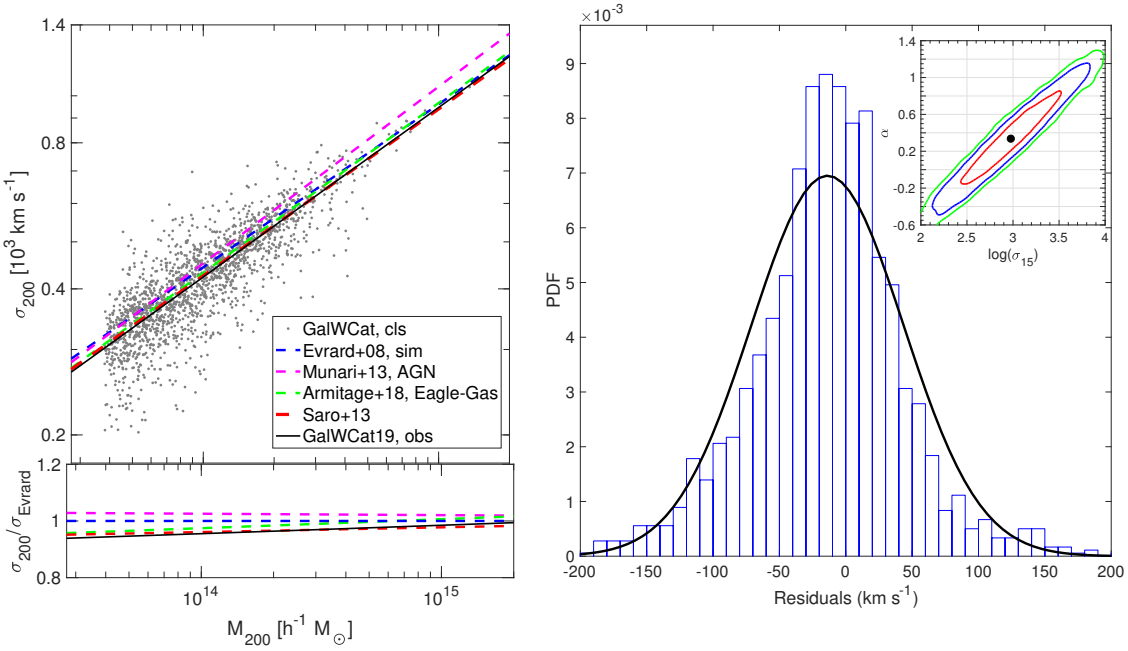

Figure 3.6: Top left panel: Velocity dispersion σ_{200} vs. virial mass M_{200} for 1,800 clusters in the `GalWCat19` catalog. The gray points show the `GalWCat19` clusters and the solid black line represents the best-fit relation from Equation 3.27. The blue, purple, green, and red dashed lines show the relations for Evrard et al. (2008), Munari et al. (2013) Saro et al. (2013), and Armitage et al. (2018) derived from cosmological simulations, respectively. As shown, the GalWeight relation matches the models remarkably well, indicating the accuracy of the GalWeight to constrain cluster membership, and consequently determine cluster masses. Bottom left panel: best-fit relations relative to the Evrard et al. (2008) result. Right panel: The distribution of residual of velocity dispersion of clusters from the best-fit line, along with best-fit the Gaussian curve. The inner right panel shows the best-fit parameters of Equation 3.27 with $1, 2, 3\sigma$ confidence intervals.

including baryonic physics in simulations affected the relation. Compared to the relation derived purely from N-body simulations (Evrard+08), the relations found by Munari+13, Saro+13 Armitage+18 suggested that galaxies introduce a bias in velocity relative to the DM particles (see Figure 3.6). This bias can be either positive (a larger σ for a given M than what the DM particles have) or negative (a smaller σ for a given M than what the DM particles have), depending on the halo mass, redshift and physics implemented in the simulation (e.g., Saro et al., 2013; Old et al., 2013; Wu et al., 2013). Also, Saro+13 concluded that the effect of the presence of interlopers on the estimated velocity dispersion could be the dominant source of uncertainty (up to $\sim 49\%$). However, the more sophisticated interloper rejection techniques, such as caustic Diaferio (1999) and GalWeight techniques Abdullah et al. (2018) could result in a reduced uncertainty when calculating the velocity dispersion.

Following Evrard et al. (2008), the $\sigma_{200} - M_{200}$ relation can be expressed as

$$\sigma_{200} = \sigma_{15} \left[\frac{h(z)\ M_{200}}{10^{15} M_{\odot}} \right]^{\alpha} \tag{3.27}$$

where σ_{15} is the normalization at mass $10^{15}\ h^{-1} M_{\odot}$, and α is the logarithmic slope. We follow Kelly (2007) and Mantz (2016) to determine these two parameters in the log-log space of σ_{200} and M_{200}.

The scatter, $\delta_{\log \sigma}$, in the $\sigma_{200} - M_{200}$ relation, defined as the standard deviation of $\log(\sigma)$ about the best-fit relation (see e.g., Evrard et al., 2008; Lau et al., 2010), is given by

$$\delta_{\log \sigma} = \sqrt{\frac{1}{N} \sum_{i=1}^{N} \log(\sigma_i / \sigma_{fit})^2} \tag{3.28}$$

where σ_i is the velocity dispersion of the i^{th} cluster and σ_{fit} is the best-fit value. For σ_{200} and M_{200} determined by the virial mass estimator we get $\sigma_{15} = 946 \pm 52$ km s^{-1}, and $\alpha = 0.349 \pm 0.142$ with a scatter of $\delta_{\log\sigma} = 0.06 \pm 0.04$ for all clusters with mass $M_{200} \geq 0.4 \times 10^{14} h^{-1} M_{\odot}$.

Figure 3.6 shows the $\sigma_{200} - M_{200}$ relation for the 1,800 clusters in the `GalWCat19` catalog. The gray points represent the `GalWCat19` clusters and the solid black line is the best-fit relation from Equation 3.27. The blue, purple, green, and red dashed lines show the relations from Evrard+08, Munari+13, Saro+13, and Armitage+18 which were derived from cosmological simulations. Generally speaking, the `GalWCat19` line matches the models remarkably well, indicating the effectiveness of the GalWeight technique in constraining cluster membership, and consequently in determining cluster mass. However, we cannot make a quantitative comparison between the observed line and the other three models of Evrard+08, Munari+13 and Armitage+18. This is because Evrard+08 derived this relation for purely dark matter particles without taking into account the effect of baryons and it is well-known that galaxies are biased tracers of dark matter particles. Moreover, even though Munari+13 and Armitage+18 included baryonic physics, their relations were derived from the true members, while our sample is contaminated by interlopers (projection effects). The only relation that took into account the baryonic physics and the projection effect (i.e., presence of interlopers) is Saro+13. As shown in the Figure 3.6, Saro+13 model is the closest to our observed line.

Finally, we stress that the calculated velocity dispersion and consequently the cluster mass are scattered by the presence of interlopers as well as other factors which were

discussed above in §3.4.2. In order to study this scaling relation in detail one should take into consideration all of these factors and utilize both hydrodynamical and semi-analytic models to digest the different sources of scatter and uncertainties. This is certainly out of the scope of this paper and we defer this investigation to a later paper.

3.6 Conclusion

In this paper we used the SDSS-DR13 spectroscopic dataset to identify and analyze a catalog of 1,800 galaxy clusters (`GalWCat19`). The cluster sample has a mass range of $(0.40-14)\times10^{14}\ h^{-1}\ \mathrm{M}_{\odot}$ and a redshift range $0.01 \leq z \leq 0.2$ with a total of 34,471 galaxy members identified within the virial radii of the 1,800 clusters.

The clusters were identified by a simple algorithm that looks for the Finger-of-God effect (the distortion of the peculiar velocities of its core members along line-of-sight). The FOG effect was detected by assuming a cylinder of radius $R_{cy} = 0.5h^{-1}$ Mpc ($\sim$ the width of FOG), and height 3000 km s^{-1} ($\sim$ the length of FOG) centered at each galaxy in our sample. We selected all overdensity regions with the condition that the cylinder has at least eight galaxies. The completeness of our sample identified by the FG algorithm, was tested by the Bolshoi simulation. The completeness to identify locations of clusters with at least eight galaxies was approximately 100% for clusters with masses $M_{200} > 2\times10^{14}\ h^{-1}M_{\odot}$, while it dropped to $\approx 92\%$ for clusters with masses $M_{200} > 0.4\times10^{14}\ h^{-1}M_{\odot}$.

The membership of each detected cluster was assigned by the GalWeight technique. Then, we used the virial theorem and NFW mass profile in order to determine dynamical parameters for each cluster from its galaxy members. This integrated procedure was applied

to HOD2 and SAM2 mock catalogs recalled from Old et al., 2015 to test its efficiency in recovering cluster mass. GalWeight performs well in comparison to most other mass estimators described in Old et al., 2015 for both the HOD2 and SAM2 models. In particular, the rms differences of the recovered mass by GalWeight relative to the fiducial cluster mass are 0.26 and 0.28 for the HOD2 and SAM2, respectively. Furthermore, the rms error produced by GalWeight was among the lowest of all other methods that depend on the phase-space and velocity dispersion to calculate mass.

Using the virial mass estimator we determined the virial radius and its corresponding virial mass for each cluster. We then used NFW mass profile to determine the dynamical parameters of each cluster at density $\rho = \Delta\rho_c$, for overdensities $\Delta = [500, 200, 100, 5.5]$. We assumed that the virial radius is at $\Delta = 200$ and turnaround radius is at $\Delta = 5.5$. We introduced a cluster catalog for the dynamical parameters derived by virial mass estimator and NFW model. The derived parameters for each cluster are radius, number of members, velocity dispersion and mass at different overdensities, plus the NFW parameters: scale radius, mass at scale radius, and concentration. We also introduced a membership catalog that correspond to the cluster catalog. The description of the catalogs are introduced in appendix 3.6.

Finally, we showed that the cluster velocity dispersion scales with total mass for `GalWCat19` as $\log(\sigma_{200}) = \log(946 \pm 52 \text{ km s}^{-1}) + (0.349 \pm 0.142) \log\left[h(z)\ M_{200}/10^{15} M_{\odot}\right]$ with scatter $\delta_{\log\sigma} = 0.06$. This relation was well-fitted with the theoretical relations derived from the N-body simulations.

FUTURE WORK

In future work, we aim to: (i) study the halo-mass, stellar mass, and luminosity functions of `GalWCat19` to constrain the matter density of the universe, Ω_m, and the normalization of the linear power spectrum, σ_8; (ii) investigate the stellar mass and luminosity function of member galaxies of their hosting clusters; (iii) study the shape of velocity dispersion profiles of `GalWCat19` and compare with Multi-dark simulations in order to recover cluster mass. (iv) study the connection between stellar mass (or luminosity) and dark matter halo; (v) investigate the effect of environment on the properties of member galaxies such as size, and quenching of star formation and segregation of star forming and quiescent galaxies on a small scale; (vi) investigate the adaptation of the GalWeight technique to recover cluster mass and cluster mass profile; (vii)) study the correlation function of galaxy clusters and the signature of Acoustic Baryonic Oscillation (BAO) to constrain cosmological parameters using the `GalWCat19`.

ACKNOWLEDGMENTS

We thank Gary Mamon for the useful discussion to fit NFW model using maximum likelihood technique. We also thank Steven Murray for the publicly available code `HMFcalc` and his guideline to run the code. We also thank Stefano Andreon for his useful comments. Finally, we appreciate the comments and suggestions of the reviewer which improved this paper. This work is supported by the National Science Foundation through grant AST-1517863, by HST program number GO-15294, and by grant number 80NSSC17K0019 issued through the NASA Astrophysics Data Analysis Program (ADAP). Support for program

number GO-15294 was provided by NASA through a grant from the Space Telescope Science Institute, which is operated by the Association of Universities for Research in Astronomy, Incorporated, under NASA contract NAS5-26555. Lyndsay Old acknowledges the European Space Agency (ESA) Research Fellowship.

Description of the Catalogs in the `GalWCat19` release

The `GalWCat19` release consists of two catalogs. The first catalog lists the coordinates and the dynamical parameters of each galaxy cluster. The second catalog lists the coordinates of the member galaxies belonging to each cluster. The two catalogs are publicly-available at the website[7].

Description of the Cluster Catalog

The cluster catalog contains the following information (column numbers are given in square brackets):

[1] `clsid` – our unique identification number for clusters;

[2 – 3] `raj2000, dej2000` – right ascension and declination of the cluster center in deg;

[4] z_{cls} – cluster redshift, calculated as an average over all cluster members;

[5] v_{cls} – radial velocity of the cluster in units of km s^{-1};

[6] D_{cls} – comoving distance of the cluster in units of h^{-1} Mpc;

[7] R_{500} – the radius from the cluster center at which the density $\rho = \Delta_{500}\rho_c$ in units of h^{-1} Mpc;

[8] N_{500} – number of members of the cluster within R_{500};

[7] https://mohamed-elhashash-94.webself.net/

[9] σ_{500} – velocity dispersion in km s^{-1} of the cluster within R_{500};

[$10-11$] $\sigma\_Err(-)_{500}$, $\sigma\_Err(+)_{500}$ – lower and upper errors of σ_{500} in km s^{-1}, obtained via 1000 bootstrap resampling;

[12] M_{500} – mass of the cluster at R_{500} in units of $10^{14}\ h^{-1}M_{\odot}$;

[13] M_Err_{500} – error in M_{500} in units of $10^{14}\ h^{-1}M_{\odot}$;

[14] R_{200} – the radius from the cluster center at which the density $\rho = \Delta_{200}\rho_c$ in units of h^{-1} Mpc;

[15] N_{200} – number of members of the cluster within R_{200};

[16] σ_{200} – velocity dispersion in km s^{-1} of the cluster within R_{200};

[$17-18$] $\sigma\_Err(-)_{200}$, $\sigma\_Err(+)_{200}$ – lower and upper error of σ_{200} in km s^{-1}, obtained via 1000 bootstrap resampling;

[19] M_{200} – mass of the cluster at R_{200} in units of $10^{14}\ h^{-1}M_{\odot}$;

[20] M_Err_{200} – error in M_{200} in units of $10^{14}\ h^{-1}M_{\odot}$;

[21] R_{100} – the radius from the cluster center at which the density $\rho = \Delta_{100}\rho_c$ in units of h^{-1} Mpc;

[22] N_{100} – number of members of the cluster within R_{100};

[23] σ_{100} – velocity dispersion in km s^{-1} of the cluster within R_{100};

[$24-25$] $\sigma\_Err(-)_{100}$, $\sigma\_Err(+)_{100}$ – lower and upper errors of σ_{100} in km s^{-1}, obtained via 1000 bootstrap resampling;

[26] M_{100} – mass of the cluster at R_{100} in units of $10^{14}\ h^{-1}M_{\odot}$;

[27] M_Err_{100} – error in M_{100} in units of $10^{14}\ h^{-1}M_{\odot}$; [28] $R_{5.5}$ – the radius from the cluster center at which the density $\rho = \Delta_{5.5}\rho_c$ in units of h^{-1} Mpc;

[29] $N_{5.5}$ – number of members of the cluster within $R_{5.5}$;

[30] $\sigma_{5.5}$ – velocity dispersion in km s^{-1} of the cluster within $R_{5.5}$;

[31 − 32] $\sigma\_Err(-)_{5.5}$, $\sigma\_Err(+)_{5.5}$ – lower and upper errors of $\sigma_{5.5}$ in km s^{-1}, obtained via 1000 bootstrap resampling;

[33] $M_{5.5}$ – mass of the cluster at $R_{5.5}$ in units of $10^{14}\ h^{-1}M_{\odot}$;

[34] $M\_Err_{5.5}$ – error in $M_{5.5}$ in units of $10^{14}\ h^{-1}M_{\odot}$;

[35] R_s – scale radius of NFW model in units of h^{-1} Mpc;

[36] R_s_Err – error in scale radius of NFW model in units of h^{-1} Mpc;

[37] M_s – scale mass of the cluster at R_s in units of $10^{14}\ h^{-1}M_{\odot}$;

[38] M_s_Err – error in M_s in units of $10^{14}\ h^{-1}M_{\odot}$;

[39] c – cluster concentration of NFW model

Description of the Galaxy Catalog

The catalog of the member galaxies correspond to the cluster catalog:

[1] `clsid` – our unique identification number for clusters that member galaxies belong to;

[2 − 3] `raj2000, dej2000` – right ascension and declination of the galaxy in deg;

[4] z_g – observed redshift of the galaxy as given in the SDSS-DR-13;

Chapter 4

Cosmological Constraints on Ω_m and σ_8 from Cluster Abundances using the GalWCat19 Optical-Spectroscopic SDSS Catalog

We derive cosmological constraints on the matter density, Ω_m, and the amplitude of fluctuations, σ_8, using GalWCat19, a catalog of 1800 galaxy clusters we identified in the Sloan Digital Sky Survey-DR13 spectroscopic data set using our GalWeight technique to determine cluster membership (Abdullah et al., 2018, 2020b). By analyzing a subsample of 756 clusters in a redshift range of $0.045 \leq z \leq 0.125$ and virial masses of $M \geq 0.8 \times 10^{14}\ h^{-1}\ M_{\odot}$ with

mean redshift of $z = 0.085$, we obtain $\Omega_m = 0.310^{+0.023}_{-0.027} \pm 0.041$ (systematic) and $\sigma_8 = 0.810^{+0.031}_{-0.036} \pm 0.035$ (systematic), with a cluster normalization relation of $\sigma_8 = 0.43\Omega_m^{-0.55}$. There are several unique aspects to our approach: we use the largest spectroscopic data set currently available, and we assign membership using the GalWeight technique which we have shown to be very effective at simultaneously maximizing the number of *bona fide* cluster members while minimizing the number of contaminating interlopers. Moreover, rather than employing scaling relations, we calculate cluster masses individually using the virial mass estimator. Since `GalWCat19` is a low-redshift cluster catalog we do not need to make any assumptions about evolution either in cosmological parameters or in the properties of the clusters themselves. Our constraints on Ω_m and σ_8 are consistent and very competitive with those obtained from non-cluster abundance cosmological probes such as Cosmic Microwave Background (CMB), Baryonic Acoustic Oscillation (BAO), and supernovae (SNe). The joint analysis of our cluster data with Planck18+BAO+Pantheon gives $\Omega_m = 0.315^{+0.013}_{-0.011}$ and $\sigma_8 = 0.810^{+0.011}_{-0.010}$.

4.1 Introduction

In the current picture of structure formation, galaxy clusters arise from rare high peaks of the initial density fluctuation field. These peaks grow in a hierarchical fashion through the dissipationless mechanism of gravitational instability with more massive halos growing via continued accretion and merging of low-mass halos (White & Frenk, 1991; Kauffmann et al., 1999, 2003). Galaxy clusters are the most massive virialized systems in the universe and are uniquely powerful cosmological probes. The cluster mass function

(CMF), or the abundance of galaxy clusters, is particularly sensitive to the matter density of the universe Ω_m and σ_8, the root-mean-square (rms) mass fluctuation on the scale of 8 h^{-1} Mpc at z = 0 (e.g., Wang & Steinhardt, 1998; Battye & Weller, 2003; Dahle, 2006; Wen et al., 2010b).

Cosmological analyses have been performed using samples of galaxy cluster constructed from galaxy surveys (e.g., Rozo et al., 2010; Kirby et al., 2019; DES Collaboration et al., 2020), X-ray emission (e.g., Vikhlinin et al., 2009b; Mantz et al., 2015), and thermal Sunyaev-Zel'dovich (SZ) signal (e.g., Bocquet et al., 2019; Zubeldia & Challinor, 2019). These cluster abundance studies showed that Ω_m varies from $\sim$ 0.2 to 0.4 and σ_8 varies from $\sim$ 0.6 to 1.0. The discrepancies or tensions among these various studies is basically dependent on the accuracy of cluster mass estimation. Cluster mass can be calculated from cluster dynamics using, for example, the virial mass estimator (e.g., Binney & Tremaine, 1987), the weak gravitational lensing (Wilson et al., 1996; Holhjem et al., 2009), and the application of Jeans equation for the gas density calculated from the x-ray analysis of galaxy cluster (Sarazin, 1988). It can be also estimated from other observables, the so-called mass proxies, which scale tightly with cluster mass, such as X-ray luminosity (e.g., Pratt et al., 2009), optical luminosity or richness (e.g. Yee & Ellingson, 2003; Simet et al., 2017), and the velocity dispersion of member galaxies (e.g., Biviano et al., 2006; Bocquet et al., 2015). Generally, most of these methods introduce large systematic uncertainties which limits the accuracy of estimating cluster masses (e.g., Wojtak & Łokas, 2007; Mantz et al., 2016).

Cosmological analyses of galaxy cluster abundance introduce a degeneracy between Ω_m and σ_8. Large ongoing and upcoming wide and deep-field imaging and spectroscopic

surveys at different redshifts, such as DES (Abbott et al., 2018a), eROSITA (Merloni et al., 2012), LSST (LSST Science Collaboration et al., 2009), and WFIRST (Akeson et al., 2019), will simultaneously increase the precision of measuring the cosmological parameters and break the degeneracy between them. This is because Ω_m evolves slowly while σ_8 evolves strongly with redshift. Also, these galaxy surveys at different redshifts are significant to study the evolution of the CMF which is critical to measuring structure growth, and therefore can be used to constrain properties of dark energy (e.g, Haiman et al., 2001; Mantz et al., 2008). Introducing advanced methods is essential to analyze these surveys. One of these methods is the GalWeight technique (Abdullah et al., 2018, hereafter Abdullah+18) which can by applied to the available and upcoming spectroscopic database of eBOSS (Raichoor et al., 2017), DESI (Levi et al., 2019), and Euclid (Euclid Collaboration et al., 2019) to construct cluster catalogs. These catalogs provide an unlimited data source for a wide range of astrophysical and cosmological applications.

In addition, there are independent cosmological probes to constraining the cosmological parameters that can be applied alongside or in combination with galaxy cluster abundance. The anisotropies in the cosmic microwave background (CMB) are an independent probe of cosmological parameters (e.g., Hinshaw et al., 2013; Planck Collaboration et al., 2016). The likelihoods of the Ω_m-σ_8 confidence levels introduced by the CMF and CMB are almost orthogonal to each other, which means combining these measurements will eliminate the degeneracy between Ω_m and σ_8 and shrink the uncertainties. Other independent cosmological probes that are used to constrain Ω_m and σ_8 include cosmic shear, galaxy-galaxy lensing, and angular clustering (e.g, Abbott et al., 2018b; van Uitert et al.,

2018). The likelihoods of the Ω_m-σ_8 confidence levels introduced by these probes are almost parallel to those introduced by the CMF. Moreover, the two cosmological probes of baryon acoustic oscillations (BAO, e.g., Eisenstein et al., 2005) and supernovae (SNe, e.g., Perlmutter et al., 1999) can be used to constrain Ω_m only (independent of σ_8).

In this paper, we aim to derive the CMF and the cosmological parameters Ω_m and σ_8 using a subsample of 756 clusters (`SelFMC`) obtained from the `GalWCat19` cluster catalog as we discuss below in detail. The `GalWCat19` (Abdullah et al., 2020b, hereafter Abdullah+20) catalog was derived from the Sloan Digital Sky Survey-Data Release 13 spectroscopic data set (hereafter SDSS-DR13[1], Albareti et al., 2017). The clusters were first identified by looking for the Finger-of-God effect (see, Jackson, 1972; Kaiser, 1987; Abdullah et al., 2013). The cluster membership was constructed by applying our own GalWeight technique which was specifically designed to simultaneously maximize the number of *bona fide* cluster members while minimizing the number of contaminating interlopers (Abdullah+18). In Abdullah+18, we applied our GalWeight technique to MDPL2 and Bolshoi N-body simulations and showed that it was $> 98\%$ accurate in correctly assigning cluster membership. The `GalWCat19` catalog is at low-redshift for which the effects of cluster evolution and cosmology are minimal. Finally, the cluster masses were calculated individually from the dynamics of the member galaxies via the virial theorem (e.g., Limber & Mathews, 1960; Abdullah et al., 2011), and corrected for the surface pressure term (e.g., The & White, 1986; Carlberg et al., 1997). A huge advantage of our approach relative to mass proxy methods is that it returns an estimate of the total cluster mass (dark matter and baryons) without making any assumptions about the internal complicated physical pro-

[1] `https://www.sdss.org/dr13/`

cesses associated with the baryons (gas and galaxies). The publicly available `GalWCat19`[2], contains 1800 clusters at redshift $z \leq 0.2$, which is one of the largest available samples that used a high-quality spectroscopic data set.

The paper is organized as follows. In § 4.2, we describe in more detail how we created the `GalWCat19` cluster catalog. In § 4.3, we investigate the volume and mass incompleteness of `GalWCat19` to obtain a mass-complete local subsample of 756 clusters (`SelFMC`) used to constrain Ω_m and σ_8. In § 4.4, we compare our complete sample with theoretical models to constrain the cosmological parameters Ω_m and σ_8. We investigate how systematics affect the recovered cosmological constraints and compare our results with recent results constrained from some cosmological probes and summarize our conclusions in § 4.5. Throughout the paper we adopt ΛCDM with $\Omega_m = 1 - \Omega_\Lambda$, and $H_0 = 100\ h$ km s^{-1} Mpc^{-1}.

4.2 The `GalWCat19` Cluster Catalog

In this section, we summarize how we created the `GalWCat19` cluster catalog. Full details may be found in Abdullah+20. Using photometric and spectroscopic databases from SDSS- DR13, we extracted data for 704,200 galaxies. These galaxies satisfied the following set of criteria: spectroscopic detection, photometric and spectroscopic classification as galaxy (by the automatic pipeline), spectroscopic redshift between 0.001 and 0.2 (with a redshift completeness > 0.7, Yang et al., 2007; Tempel et al., 2014), r-band magnitude (reddening-corrected) < 18, and the flag SpecObj.zWarning is zero indicating a well-measured redshift.

[2] https://mohamed-elhashash-94.webself.net/galwcat

Galaxy clusters were identified by the well-known Finger-of-God effect (Jackson, 1972; Kaiser, 1987; Abdullah et al., 2013). The Finger-of-God effect causes a distortion of line-of-sight velocities of galaxies in the redshift-phase space due to the cluster potential well. As described in Abdullah+20, we calculated the membership of each cluster as follows. We firstly calculated the galaxy number density within a cylinder of radius 0.5 h^{-1} Mpc, and height 3000 km s^{-1} centered on a galaxy, i. Secondly, we sorted all galaxies descending from highest to lowest number densities with the condition that the cylinder has at least 8 galaxies. Thirdly, starting with the galaxy with the highest number density, we applied the binary tree algorithm (e.g., Serra et al., 2011) to accurately determine a cluster center ($\alpha_c,\ \delta_c, z_c$) and a phase-space diagram. Fourthly, we applied the GalWeight technique (Abdullah+18) to galaxies in the phase-space diagram out to a maximum projected radius of 10 h^{-1} Mpc and a maximum line-of-sight velocity range of $\pm$3000 km s^{-1} to identify cluster membership. In Abdullah+18, we showed that the cumulative completeness of the FOG algorithm which we tested using the Bolshoi simulation Klypin et al. (2016) was approximately 100% for clusters with masses $M_{200} > 2 \times 10^{14}\ h^{-1} M_{\odot}$, and $\sim$ 85% for clusters with masses $M_{200} > 0.4 \times 10^{14}\ h^{-1} M_{\odot}$.

The virial mass of each cluster was estimated by applying the virial theorem to the cluster members, under the assumption that the mass distribution follows the galaxy distribution (e.g., Giuricin et al., 1982; Merritt, 1988). The estimated mass was corrected for the surface pressure term which, otherwise, would overestimate the fiducial cluster mass (e.g., The & White, 1986; Binney & Tremaine, 1987; Carlberg et al., 1997). The cluster virial mass was calculated at the viral radius within which the cluster is in hydrostatic equilibrium.

The virial radius is approximately equal to the radius at which the density $\rho = \Delta_{200}\rho_c$, where ρ_c is the critical density of the universe and $\Delta_{200} = 200$ (e.g., Carlberg et al., 1997; Klypin et al., 2016). Abdullah+20 showed that the cluster mass estimates returned by the virial theorem after utilizing the GalWeight technique (Abdullah+18) performed very well in comparison to most of other mass estimation techniques described in Old et al., 2015. In particular, our procedure was applied to two mock catalogs (HOD2 and SAM2) recalled from Old et al. (2015). We found that the root mean square differences of the recovered mass by GalWeight relative to the fiducial cluster mass were 0.24 and 0.32 for HOD2 and SAM2, respectively. Also, the intrinsic scatter in the recovered mass was ~ 0.23 dex for both catalogs. Moreover, the uncertainty of the virial mass estimator is calculated using the limiting fractional uncertainty $\pi^{-1}\sqrt{2\ln N/N}$ (Bahcall & Tremaine, 1981).

The scatter and bias in the recovered mass using the virial mass estimator are caused by some factors including: (i) the assumption of hydrostatic equilibrium, projection effect, and possible velocity anisotropies in galaxy orbits, and the assumption that halo mass follows light (or stellar mass); (ii) the presence of substructure and/or nearby structure such as cluster, supercluster, to which the cluster belongs, or filament (e.g., Merritt, 1988; Fadda et al., 1996); (iii) the presence of interlopers in the cluster frame due to the triple-value problem, for which there are some foreground and background interlopers that appear to be part of the cluster body because of the distortion of phase space (Tonry & Davis, 1981; Abdullah et al., 2013); and (iv) the identification of cluster center (e.g., Girardi et al., 1998b; Zhang et al., 2019).

The 1800 `GalWCat19` clusters range in redshift between $0.01 - 0.2$ and in mass

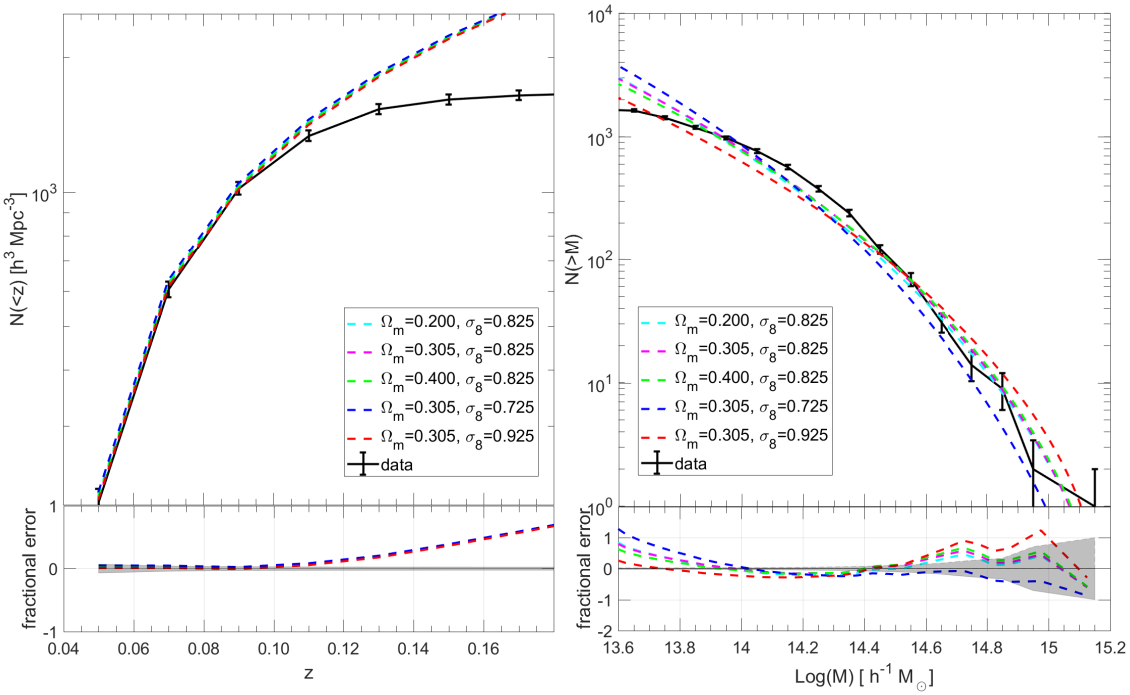

Figure 4.1: `GalWCat19` completeness. **Left**: The black line shows the integrated abundance of clusters as a function of redshift for the `GalWCat19` catalog. The dashed color lines present the expectation of complete samples estimated by Tinker08 for five different cosmologies as shown in the legend. **Right**: The black line shows the integrated abundance of clusters as a function of cluster mass. The dashed color lines present the expectation of complete samples estimated by Tinker08 for five different cosmologies as shown in the legend. The fractional error $(N(<z)_{obs} - N(<z)_{model})/N(<z)_{model}$ is shown in the lower panels. The gray shaded areas represent the expected Poisson noise.

between $(0.4 - 14) \times 10^{14} h^{-1} M_{\odot}$. The `GalWCat19` catalog contains a large number of cluster parameters including sky position, redshift, membership, velocity dispersion, and mass at overdensities $\Delta = 500, 200, 100, 5.5$. The 34,471 member galaxies were identified within the radius at which the density is 200 times the critical density of the universe. The galaxy catalog provided the coordinates of each galaxy and the ID of the cluster that the galaxy belongs to. The catalogs was publicly available at the following website `https://mohamed-elhashash-94.webself.net/galwcat/`.

4.3 Cluster mass function

The `GalWCat19` catalog is not complete in either volume or mass. In § 4.3.1, we analyze `GalWCat19` to develop an appropriate selection function of our sample which is used to correct for the volume incompleteness. Also, in § 4.3.2, we compute the CMF derived from `GalWCat19` and compare it with the CMF calculated from the MDPL2 [3] simulation (described in the next paragraph) to obtain a mass-complete subsample (`SelGMC`) used to constrain the cosmological parameters Ω_m and σ_8.

The MDPL2 is an N-body simulation of 3840^3 particles in a box of comoving length 1 h^{-1} Gpc, mass resolution of 1.51×10^9 h^{-1} $M_{\odot}$, and gravitational softening length of 5 h^{-1} kpc (physical) at low redshifts from the suite of MultiDark simulations (see Table 1 in Klypin et al., 2016). It was run using the L-GADGET-2 code, a version of the publicly available cosmological code GADGET-2 (Springel, 2005). It assumes a flat ΛCDM cosmology, with cosmological parameters $\Omega_{\Lambda} = 0.693$, $\Omega_m = 0.307$, $\Omega_b = 0.048$, $n = 0.967$, $\sigma_8 = 0.823$, and h

[3] `https://www.cosmosim.org/cms/simulations/mdpl2/`

$= 0.678$ (Planck Collaboration et al., 2014). Haloes and subhaloes have been identified with ROCKSTAR (Behroozi et al., 2013b) and merger trees constructed with CONSISTENT TREES (Behroozi et al., 2013c). The catalogs are split into 126 snapshots between redshifts $z = 17$ and $z = 0$. We downloaded the snapshot (hlist_0.91520.list[4]) with $z \sim 0.09$ which is consistent with the mean redshift of `GalWCat19` sample.

4.3.1 `GalWCat19` Completeness

The `GalWCat19` catalog is incomplete in the distribution of clusters with respect to comoving distance (redshift), and in the distribution of clusters with respect to mass. In this section, we discuss such incompleteness and how to make corrections.

The completeness in comoving volume (redshift) of the `GalWCat19` catalog can be investigated by calculating the abundance of clusters predicted by a theoretical model and comparing it with the abundance of `GalWCat19` clusters. We adopt the functional form of Tinker et al. (2008) (hereafter Tinker08) to calculate the halo mass function (HMF[5], see § 4.4.1 for more details) and consequently the predicted abundance of clusters.

The integrated abundance of clusters as a function of redshift for the `GalWCat19` sample, $N(< z)$, is presented in the upper left panel of Figure 4.1. Note that $N(< z)$ is calculated for the clusters with redshift $z \geq 0.04$ to remove the effect of nearby regions where the cosmic variance has a large effect due to the small volume. The plot shows that the catalog is matched with the prediction of Tinker08 for $z \lesssim 0.09$. Also, the fractional error of $N(< z)$ relative to the expectation of Tinker08, $(N(< z)_{obs} - N(< z)_{model})/N(< z)_{model}$,

[4] https://www.cosmosim.org/data/catalogs/NewMD_3840_Planck1/ROCKSTAR/trees/hlists/

[5] We use CMF for mass functions derived from observations and HMF for mass functions computed by theoretical models

for each model and the expected Poisson noise (gray shaded area) are presented in the lower left panel. The plot shows that the scatter relative to each model is nearly constant (around zero) for $z \lesssim 0.09$ before it blows up after this redshift limit. This indicates that `GalWCat19` is approximately complete in volume for $z \lesssim 0.09$ (or equivalently comoving distance of $D \lesssim 265\ h^{-1}\,\mathrm{Mpc}$ for the ΛCMD universe with $\Omega_m = 0.3$). We call this volume-complete subsample as `NoSelFVC`.

Similarly, the integrated abundance of clusters as a function of cluster mass, $N(>M)$, is presented in the upper right panel of Figure 4.1 in comparison to five Tinker08 models and the scatter is presented in the lower right panel. The plot shows that the data is matched with the models of $\Omega_m = [0.20, 0.305, 0.40]$ with $\sigma_8 = 0.825$ better than the models of $\Omega_m = 0.305$ and $\sigma_8 = [0.725, 0.925]$. Even though it is not an easy task to specifically determine the mass threshold at which the catalog is complete, the three matched models indicate that `GalWCat19` is approximately complete for $\log(M) \gtrsim 13.9\ h^{-1}\ M_\odot$. We discuss the systematics of adapting this mass threshold on our analysis in § 4.5.1. The large scatter at the high mass end is due to the small number of massive clusters, while the large scatter at the low mass end comes from the incompleteness of `GalWCat19`.

In order to correct for the incompleteness in volume of `GalWCat19` each cluster should be weighed by $\mathcal{S}(D)$, where $\mathcal{S}$ is the selection function at a distance D. Figure 4.2 introduces the normalized number density $\mathcal{N}_n(D)$, defined as the cluster number density normalized by the average number density calculated for clusters within comoving distance $D < 265\ h^{-1}\,\mathrm{Mpc}$, for all clusters and for five mass bins as described in Table 4.1. The distribution of points in Figure 4.2 can be described by an exponential function that represents

the selection function $\mathcal{S}(D)$. It has the form

$$\mathcal{S}(D) = a \exp\left[-\left(\frac{D}{b}\right)^{\gamma}\right] \tag{4.1}$$

The parameters a, b and γ are determined by applying the chi-squared algorithm using the Curve Fitting MatLab Toolbox. The best fit values of these parameters are, $a = 1.07 \pm 0.12$, $b = 293.4 \pm 20.7\ h^{-1}\,\mathrm{Mpc}$ and $\gamma = 2.97 \pm 0.90$ with root mean square error of 0.15. Note that the normalization a is greater than unity because of the scatter and the effect of the cosmic variance. But, we apply the selection function with the condition that $\mathcal{S}(D) \leq 1$.

We should be cautious in using $\mathcal{S}(D)$ at large distances. This is because $S(D \gtrsim 500)\ h^{-1}\,\mathrm{Mpc}$ drops to $\gtrsim 0.01$ as demonstrated in Figure 4.2 which means that a distant cluster would be weighted as at least 100 times as a nearby cluster. This will overestimate or overcorrect the number of clusters at large distances, and consequently the estimated CMF will be noisy. Thus, in order to avoid the overcorrection and the noisiness of CMF we restrict our sample to a maximum comoving distance of $D \leq 365$ (or $z \leq 0.125$) for which $\mathcal{S}(D) \lesssim 0.2$.

It is well-known that the cluster number density of a given mass decreases with redshift for a 100% complete sample because of the HMF evolution effect. Thus, the CMF should be scaled or corrected by an evolution function, $\mathcal{S}_{evo}(D)$. For a sample with a broad range of redshifts, the only way to take the evolution into account is to calculate this function. However, the disadvantage of this approach is that the correction is model dependent: the measured HMF (i.e., CMF) is a convolution of the true HMF and theoretical estimate of $\mathcal{S}_{evo}(D)$. However, for a sample with a narrow range of redshifts (as in our case)

Table 4.1: The cluster average number density for different mass bins.

Mass bin $[h^{-1}\ M_{\odot}]$	number of clusters	average number density $[10^{-5}\ h^3\ \mathrm{Mpc}^{-3}]$	color
13.6 - 15.2	1800	5.6	black
13.6 - 13.8	527	2.2	blue
13.8 - 14.0	461	1.5	green
14.0 - 14.2	411	1.0	red
14.2 - 14.5	326	0.7	cyan
14.5 - 15.2	75	0.2	magenta

Columns: (1) the mass bin in units of $\log \mathrm{M}\ [h^{-1}\ M_{\odot}]$; (2) the number of clusters in each mass bin; (3) the average number density calculated for clusters within comoving distance $D < 265\ h^{-1}\,\mathrm{Mpc}$ in each mass bin; (4) the color of number density profile as shown in the right panel of Figure 4.1.

we show in appendix 4.5.4 that the evolution effect is less than 3% for clusters in the redshift range of $0.045 \leq z \leq 0.125$. In appendix 4.5.4, we discuss the effect of adopting this redshift interval on our results.

4.3.2 Estimating the Mass Function

In this section, we compute the CMF, $\mathrm{d}n(M)/\mathrm{dlog}(M)$, and its corresponding cumulative mass function, $n(>M)$, which are estimated for a ΛCDM cosmology with Ω_m= 0.3 and $\Omega_\Lambda = 0.7$. The CMF is defined as the number density of clusters per logarithmic cluster mass interval. Also, the cumulative CMF is defined as the number density of clusters more massive than a given mass M.

Mathematically, the CMF, weighted by the selection function $\mathcal{S}$, is given by

$$\frac{dn(M)}{d\log M} = \frac{1}{d\log M}\sum_i \frac{1}{V}\frac{1}{\mathcal{S}(D_i)} \tag{4.2}$$

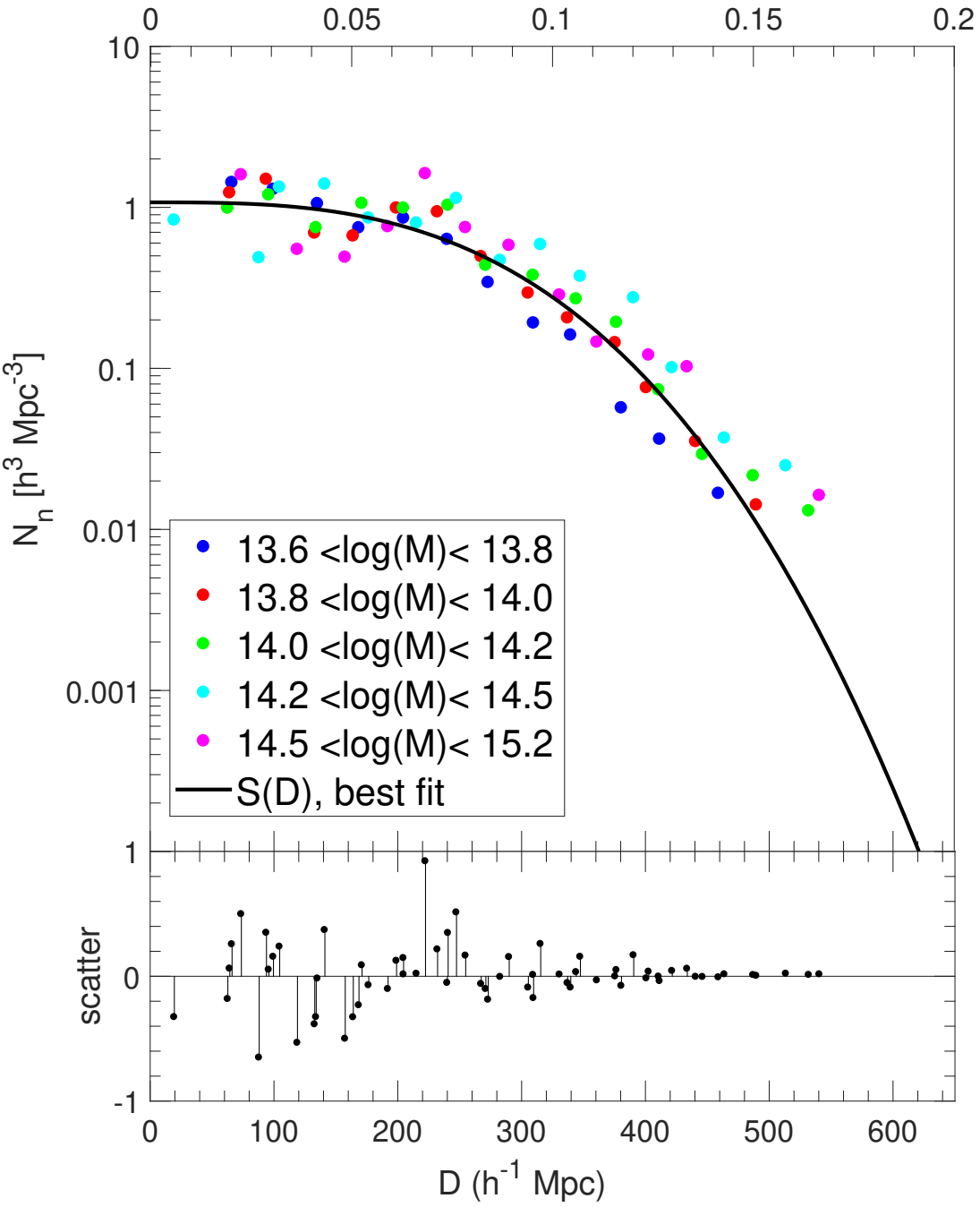

Figure 4.2: Selection function of `GalWCat19` cluster sample. Colored points show the normalized number density of the five mass bins described in Figure 4.1. The black line shows an exponential form describing the selection function $\mathcal{S}(D)$ which is fitted with the data. The scatter of data relative to the exponential form is presented in the lower panel.

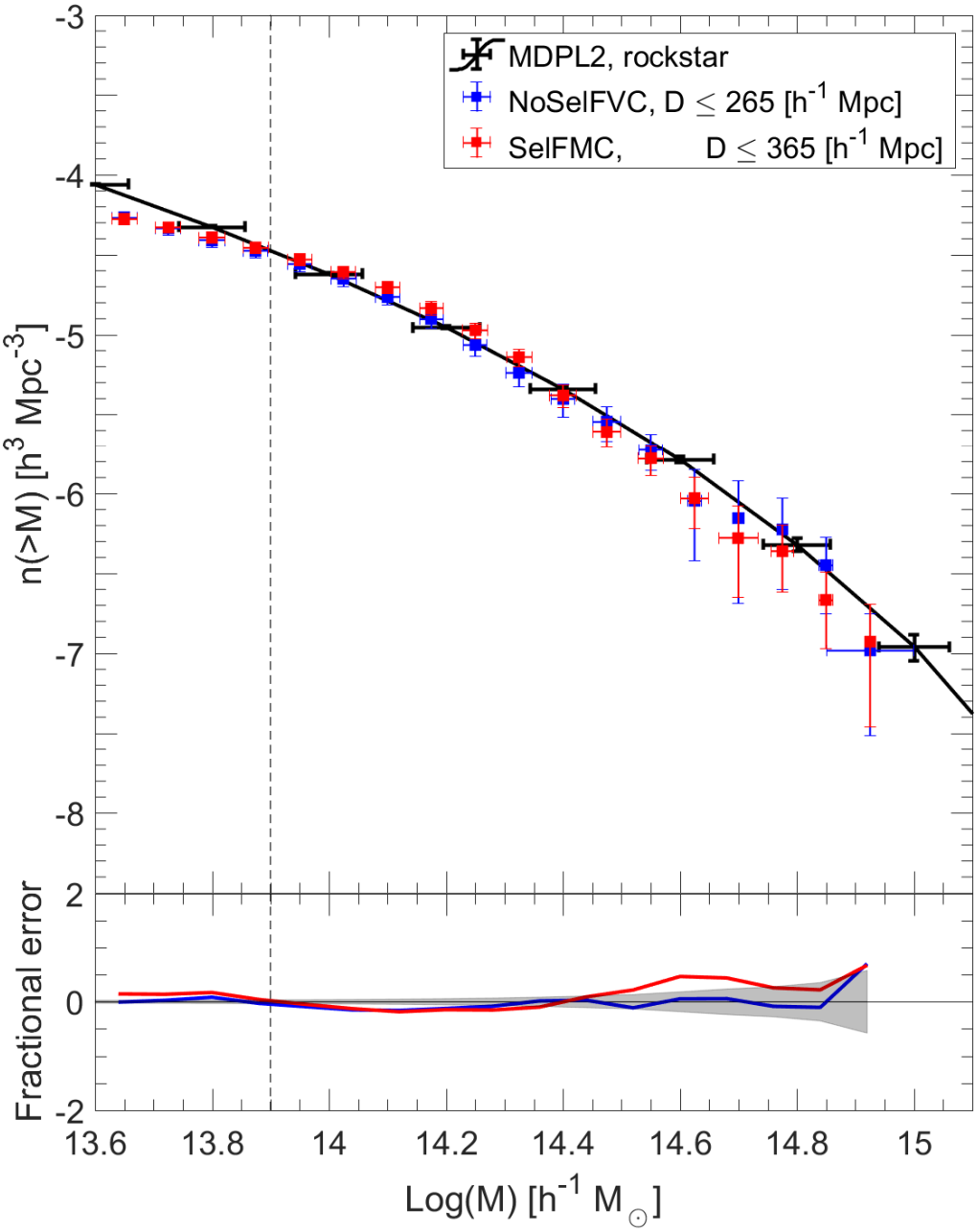

Figure 4.3: The cumulative CMF derived from the `GalWCat19` cluster sample. The black line shows the mass function computed from the MDPL2 simulation (for the snapshot hlist_0.91520.list at $z \sim 0.9$ or $D \sim 260$) (Klypin et al., 2016). The blue points present the CMF for the volume-complete subsample with $D \leq 265\ h^{-1}\,\mathrm{Mpc}$ ($z \sim 0.09$) without the correction of $\mathcal{S}(D)$ (`NoSelFVC`). The red points show the CMF corrected by $\mathcal{S}(D)$ for $D \leq 365\ h^{-1}\,\mathrm{Mpc}$($z \sim 0.125$, `SelFMC`). The vertical dashed line shows the low-mass limit ($\log(M) = 13.9\ h^{-1}\ M_{\odot}$) used to constrain Ω_m and σ_8. The error bars on the vertical axis are calculated by Poisson statistics. The fractional errors between the CMF of MDPL2 and both `NoSelFVC` and `SelFMC` are shown in the lower panels. The gray shaded areas represent the expected Poisson noise.

where D_i is the comoving distance of a cluster i, and V is the comoving volume which is given by

$$V = \frac{4\pi}{3}\frac{\Omega_{survey}}{\Omega_{sky}}(D_2^3 - D_1^3) \tag{4.3}$$

where $\Omega_{sky} = 41,253$ deg^2 is the area of the sky, $\Omega_{sur} \simeq 11,000$ deg^2 is the area covered by `GalWCat19`, and D_1 and D_2 are the minimum and maximum comoving distances of the cluster sample.

Figure 4.3 introduces the cumulative CMF computed from `GalWCat19`. The black line is the CMF computed from the MDPL2 simulation (for the snapshot hlist_0.91520.list at $z \sim 0.09$ or $D \sim 265$, Klypin et al., 2016). The blue points introduces the CMF for `NoSelFVC` without the correction of $\mathcal{S}(D)$, since this sample is already complete in volume (see, § 4.3.1 and Figure 4.1). The red points represents our CMF corrected by $\mathcal{S}(D)$ for $D \leq 365\ h^{-1}$ Mpc ($z \sim 0.125$). Comparing the CMF estimated by the `NoSelFVC` subsample with that derived from the MDPL2 simulation indicates that the sample is approximately complete in mass for $\log(M) \gtrsim 13.9\ h^{-1}\ M_\odot$, while it drops lower than the CMF of MDPL2 at low-mass end. Also, our CMF, corrected by $\mathcal{S}(D \leq 365)$, is in good agreement with the CMF derived from `NoSelFVC` with a scatter of 0.026 dex. The mass completeness of `GalWCat19` is discussed in § 4.3.1 and Figure 4.1. In appendix 4.5.4, we show that the results of deriving the cosmological parameters from `NoSelFVC` is consistent with that derived from `SelFMC`. This indicates that weighting each cluster in our sample by $S(D \leq 365)$ introduced in § 4.3.1 and Equation 4.1 is sufficient to correct for the volume incompleteness of `GalWCat19`.

Therefore, our final subsample, corrected by $S(D)$ is restricted by $\log(M) \geq 13.9$ h^{-1} $M_{\odot}$ and $0.045 \leq z \leq 0.125$. The number of clusters of this subsample is 756, which represents $\sim 42\%$ of the `GalWCat19` sample. We use this subsample to constrain Ω_m and σ_8 and call it as fiducial `SelFMC` sample.

4.4 Implications for Cosmological Models

In § 4.4.1, we discuss the prediction of HMF from the theoretical framework. In § 4.4 we derive the constrains on the cosmological parameters Ω_m and σ_8, and discuss the degeneracy between these two parameters.

4.4.1 Prediction of Halo Mass Function

The number of dark matter halos per unit mass per unit comoving volume of the universe, HMF, is given by

$$\frac{dn}{d\ln M} = f(\sigma)\frac{\rho_0}{M}\left|\frac{d\ln\sigma}{d\ln M}\right|; \tag{4.4}$$

here ρ_0 is the mean density of the universe, σ is the rms mass variance on a scale of radius R that contains mass $M = 4\pi\rho_0 R^3/3$, and $f(\sigma)$ represents the functional form that defines a particular HMF fit.

Assuming a Gaussian distribution of mass fluctuation, Press & Schechter (1974) used a linear theory to derive the first theoretical model (hereafter PS) of HMF. While fairly successful in matching the results of N-body simulations, the PS formalism tends to

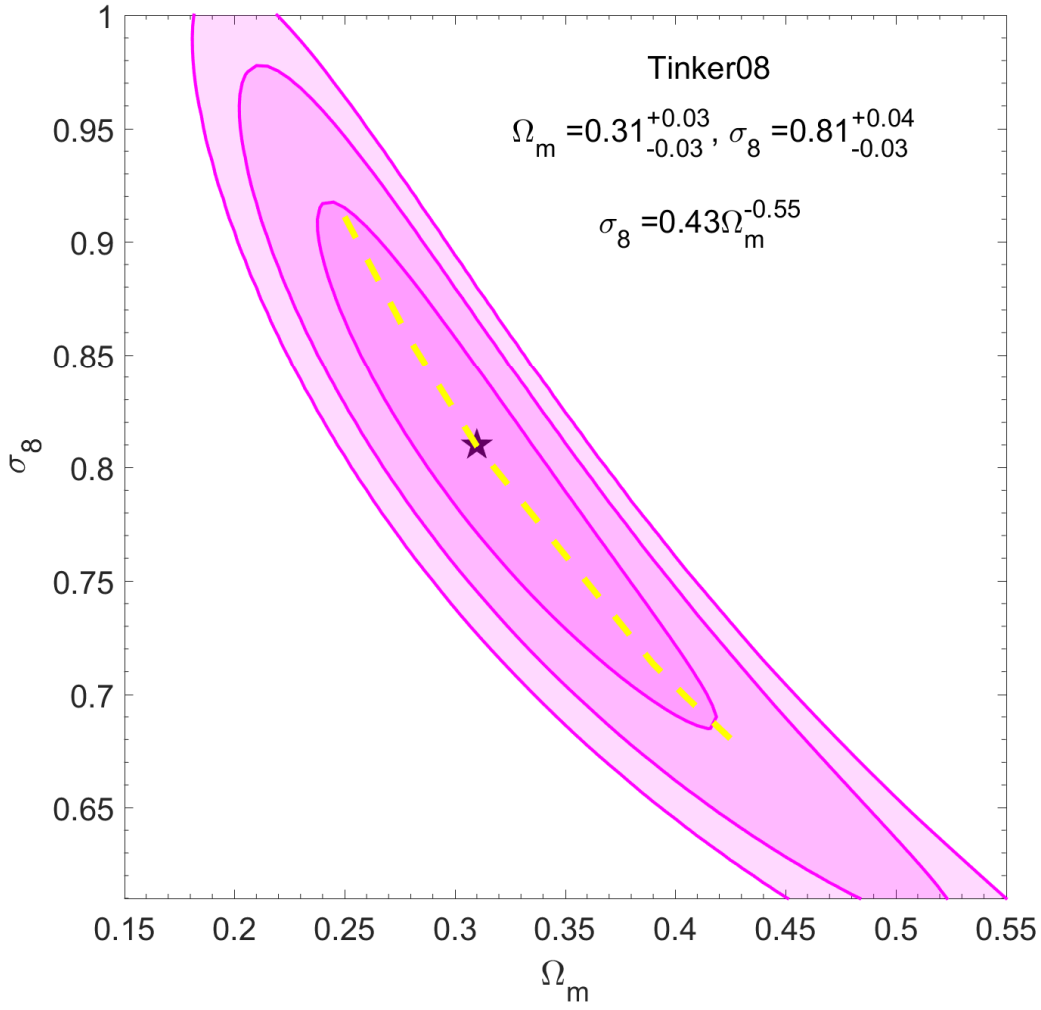

Figure 4.4: Likelihood contour map of χ^2 in σ_8-Ω_m plane derived from the `SelFMC` cluster catalog. The black star represents the best-fit point for Ω_m and σ_8 which minimizes χ^2 value. Ellipses show 1σ, 2σ, and 3σ confidence levels, respectively. The dashed yellow line represents the best-fit σ_8-Ω_m relation as shown in the legend.

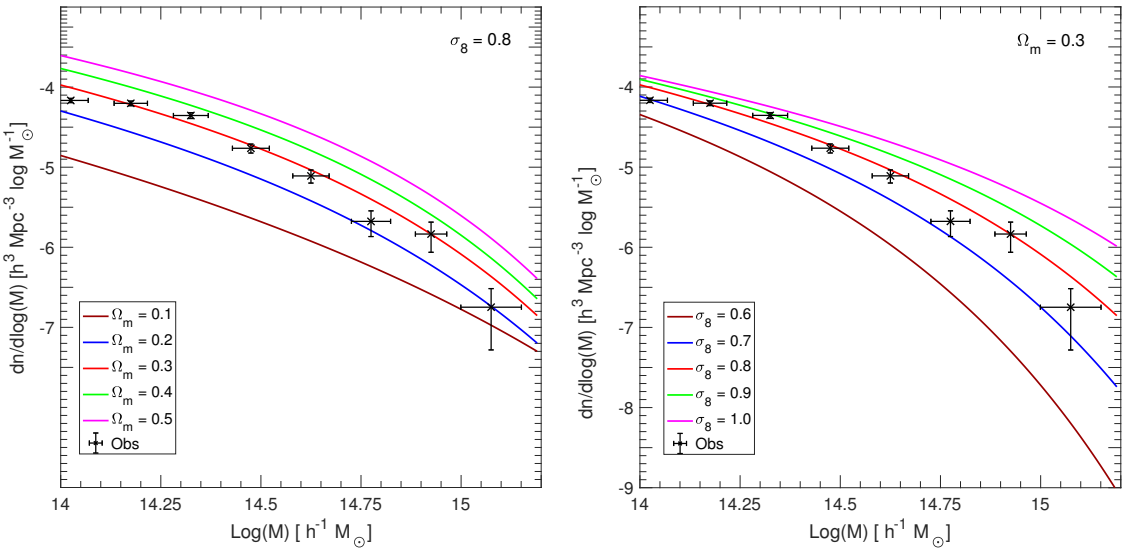

Figure 4.5: Effect of varying Ω_m and σ_8 on the HMF. The left panel shows the HMF calculated from Tinker08 for five different values of Ω_m= [0.1 0.2 0.3 0.4 0.5] while fixing σ_8= 0.3 (solid colored lines as shown in the legend). The right panel shows the HMF calculated from Tinker08 for five different values of σ_8= [0.6 0.7 0.8 0.9 1.0] while fixing Ω_m= 0.3 (solid colored lines as shown in the legend). Our derived CMF corrected by $\mathcal{S}(D)$ for $D \leq 365\ h^{-1}\,\mathrm{Mpc}(z \sim 0.125)$ is shown by black points.

predict too many low-mass clusters and too few high-mass clusters. More recently proposed theoretical models provide better approximations to the output from N-body simulations (e.g., Sheth et al., 2001; Jenkins et al., 2001; Warren et al., 2006; Tinker & Wetzel, 2010; Bhattacharya et al., 2011; Behroozi et al., 2013b).

In this paper, we adopt the functional form proposed by Tinker et al. (2008) (hereafter Tinker08) as our form of the HMF. This approach assumes universality of the HMF across the cosmological parameter space considered in this work, and uses a fitting function that was calibrated against N-body simulations. The Tinker08 model is formally accurate to better than 5% for the cosmologies close to the ΛCDM cosmology and for the mass and redshift range of interest in our study (e.g., Vikhlinin et al., 2009b). Although

the formula has been calibrated using dissipationless N-body simulations (i.e., without the effect of baryons), hydrodynamic simulations suggest that these have negligible impact for clusters with masses as high as those considered here (e.g., Rudd et al., 2008; Velliscig et al., 2014; Bocquet et al., 2016). Finally, note that the Tinker08 model is defined in spherical apertures enclosing overdensities similar to the mass we derive for the `GalWCat19` observed clusters.

$$f(\sigma, z) = A \left[\left(\frac{\sigma}{b} \right)^{-a} + 1 \right] \exp\left(-c/\sigma^2\right) \tag{4.5}$$

where $A = 0.186\,(1+z)^{-0.14}$, $a = 1.47\,(1+z)^{-0.06}$, $b = 2.57\,(1+z)^{-\alpha}$, $c = 1.19$, and $\ln \alpha(\Delta_{vir}) = [75/\left(\ln\left(\Delta_{vir}/75\right)\right)]^{1.2}$, and σ^2 is the mass variance defined as

$$\sigma^2(M, z) = \frac{g(z)}{2\pi} \int P(k) W^2(kR) k^2 dk \tag{4.6}$$

$P(k)$ is the current linear matter power spectrum (at $z = 0$) as a function of wavenumber k, $W(kR) = 3\left[\sin(kR) - kR\cos(kR)\right])/(kR)^3$ is the Fourier transform of the real-space top-hat window function of radius R, and $g(z) = \sigma_8(z)/\sigma_8(0)$ is the growth factor of linear perturbations at scales of $8h^{-1}$ Mpc, normalized to unity at $z = 0$.

The current linear power spectrum $P(k)$ is defined as $P(k) = Bk^n T^2(k)$, where $T(k)$ is the transfer function, B is the normalization constant and n is the spectral index. Usually the normalization B is calculated from the cosmological parameter σ_8, (e.g., Reiprich & Böhringer, 2002; Murray et al., 2013a). The function k^n imprints the primordial power spectrum during the epoch of inflation. The transfer function $T(k)$ quantifies how

this primordial form is evolved with time to the current linear power spectrum on different scales. The transfer function $T(k)$ is calculated using the public *Code for Anisotropies in the Microwave Background* (CAMB[6], Lewis et al., 2000). The quantities Ω_m and σ_8 are the main cosmological parameters that define the HMF. The other parameters do not strongly affect the HMF and thus we fix them during the calculation of the HMF as described below (e.g., Reiprich & Böhringer, 2002; Bahcall et al., 2003; Wen et al., 2010b).

4.4.2 Constraining Ω_m and σ_8

The HMF is calculated using the publicly available `HMFcalc` [7] code (Murray et al., 2013a). The code provides about 20 fitting functions that can be used to calculate the HMF. In this paper, in order to constrain Ω_m and σ_8, we use Tinker08 (Equation 4.5) as discussed above. We calculate the HMF by allowing Ω_m to range between [0.1, 0.6] and σ_8 between [0.6, 1.2], both in steps of 0.005. We keep the following cosmological parameters fixed: the CMB temperature $T_{cmb} = 2.725K^{\circ}$, baryonic density $\Omega_b = 0.0486$, and spectral index $n = 0.967$ (Planck Collaboration et al., 2014), at redshift $z = 0.089$ (the mean redshift of `GalWCat19`).

In order to determine the best-fit mass function and constrain Ω_m and σ_8 we use a standard χ^2 procedure

$$\chi^2 = \sum_{i=1}^{N} \left(\frac{[y_{o,i} - y_{m,i}]^2}{\sigma_i^2} \right) \tag{4.7}$$

where the likelihood, $\mathcal{L}(y|\sigma_8, \Omega_m)$, of a data (CMF) given a model (HMF) is

[6] https://camb.info/
[7] http://hmf.icrar.org/

$$\mathcal{L}(y|\sigma_8, \Omega_m) \propto \exp\left(\frac{-\chi^2(y|\sigma_8, \Omega_m)}{2}\right) \tag{4.8}$$

y_o and y_m are the data and model cumulative mass functions at a given mass and σ is the statistical uncertainty of the data.

Using the fiducial `SelFMC` sample of 756 clusters with $\log(M) \geq 13.9$ and $0.045 \leq z \leq 0.125$, the best-fit parameters for the minimum value of χ^2 are $\Omega_m = 0.310^{+0.025}_{-0.029}$ and $\sigma_8 = 0.810^{+0.039}_{-0.034}$ for Tinker08 at redshift $z = 0.085$. In § 4.5.1 we discuss the systematics of cluster mass uncertainty, mass threshold, and selection function.

The banana shape in Figure 4.4 shows the well-known degeneracy between σ_8 and Ω_m. The relationship between σ_8 and Ω_m is often expressed as

$$\sigma_8 = \alpha\ \Omega_m^{\beta} \tag{4.9}$$

The parameters α, β, and δ are determined by applying the χ^2 algorithm using the Curve Fitting MatLab. The best fit values of these parameters are $\alpha = 0.425 \pm 0.006$ and $\beta = -0.550 \pm 0.007$ with root mean square error of 0.005 for the Tinker08 model.

We now ask the question - how do Ω_m and σ_8 contribute individually to the HMF? In other words, why do cluster abundance studies introduce a degeneracy between Ω_m and σ_8? The degeneracy occurs because a low abundance of massive clusters could be caused either by a small amount of matter in the universe (a low value of Ω_m) or small fluctuations in the density field (a low value of σ_8). Similarly, a high abundance of massive clusters could be caused either by a large amount of matter in the universe (a high value of Ω_m) or

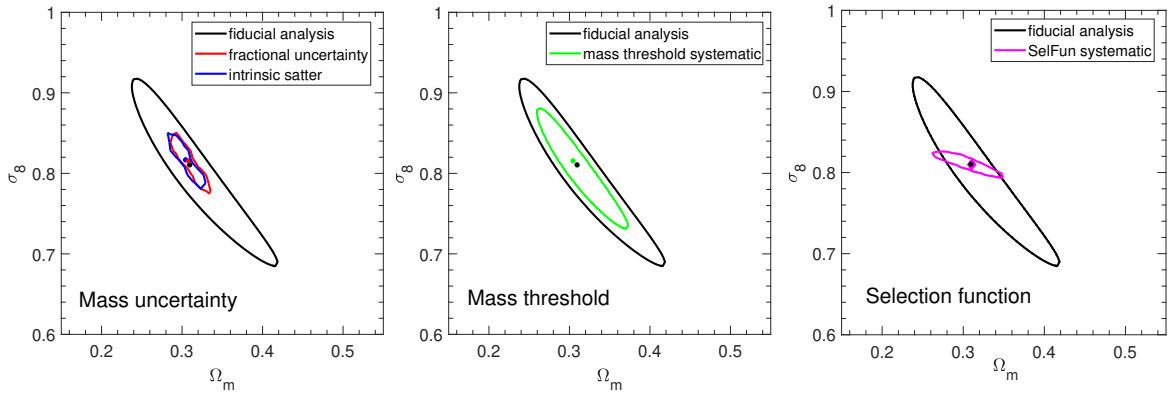

Figure 4.6: Effects of cluster mass uncertainty (left), mass threshold (middle), and selection function (right) on our constraints on Ω_m and σ_8. **Left**: the 68% CLs of our fiducial sample (black), fractional mass uncertainty (blue), and intrinsic scatter of 0.23 (red). **Middle**: the 68% CLs (green) for varying mass threshold $\log M$ from 13.8 to 14 $h^{-1}\ M_{\odot}$. **Right**: the 68% CLs (magenta) due to systematic of the selection function.

large fluctuations in the density field (a high value of σ_8). Therefore, it is possible to obtain the same abundance of massive clusters by fixing one parameter and varying the other one. Figure 4.5 introduces two sets of HMFs calculated by Tinker08. The first set is shown on the left panel for five different values of $\Omega_m = [0.1\ 0.2\ 0.3\ 0.4\ 0.5]$ while fixing $\sigma_8 = 0.8$. The second set is shown on the right panel for five different values of $\sigma_8 = [0.6\ 0.7\ 0.8\ 0.9\ 1.0]$ while fixing $\Omega_m = 0.3$. As expected, increasing the matter density of the universe increases the number of clusters of all masses. But increasing the rms mass fluctuation increases the number of high-mass clusters more dramatically than number the low-mass clusters. In other words, σ_8 is very sensitive to the high-mass end of the HMF.

4.5 Discussion and Conclusion

In this section, we investigate how systematics affect the recovered cosmological constraints from our analysis (§ 4.5.1). We compare our constraints on the cosmological

parameters Ω_m and σ_8 with those obtained from cluster abundance studies (§ 4.5.2). We also compare our constraints with those obtained from other cosmological probes which we refer to as non-cluster cosmological probes (§ 4.5.3).

4.5.1 Systematics

In constraining Ω_m and σ_8 in § 4.4.2, we only account for the statistical uncertainty of the estimated cumulative CMF using the fiducial `SelFMC` sample. In this section, we discuss the systematics due to mass uncertainty, mass threshold, and parameterization of the selection function.

Mass Uncertainty

The first uncertainty comes from the difficulty of calculating cluster masses accurately. Generally, masses which are estimated using scaling relations, such as luminosity, richness, temperature, and dispersion velocity-mass relations, introduce large scatter and consequently large systematic uncertainties (e.g., Mantz et al., 2016; Mulroy et al., 2019). Masses which are computed by dynamical estimators are subject to systematic uncertainties (e.g., Wojtak & Łokas, 2007; Rozo et al., 2010; Old et al., 2018). However, using the virial theorem, corrected for the surface pressure term, provides a relatively unbiased estimation of cluster masses (e.g., Rines et al., 2010; Ruel et al., 2014), particularly when using a sophisticated interloper rejection technique such as GalWeight (Abdullah+18). Also, the virial mass estimator calculates the total cluster mass including baryonic (gas and galaxies) and dark matter regardless the internal complex physical processes associated with the baryonic component in clusters. However, the virial mass estimator still introduces scatter

in estimating cluster masses (see § 4.2). Abdullah+20 showed that the application of the virial mass estimator on two mock catalogs (HOD2 and SAM2) recalled from Old et al. (2015) returned intrinsic scatter of ~ 0.23 dex in the recovered mass relative to the fiducial cluster mass. Also, the `GalWCat19` catalog introduced the fractional uncertainty (see § 4.2) of each cluster mass.

Assuming a normal distribution, we investigate the systematics of the mass uncertainty by generating $\sim$ 8000 estimate for each cluster mass using both the fractional uncertainty for each cluster and the intrinsic scatter for the entire sample. In other words, we reanalyze `SelFMC` ~ 8000 times and refit for Ω_m and σ_8 for each time. The left panel of Figure 4.6 introduces the effect of cluster mass uncertainty on the constraints on Ω_m and σ_8. Using the fractional uncertainty, we obtain $\Omega_m = 0.305 \pm 0.014$ and $\sigma_8 = 0.816 \pm 0.021$, where the red ellipse represents 68% CL for the disribution of the reestimated 8000 pairs of Ω_m and σ_8. Using the intrinsic scatter (blue ellipse), we find $\Omega_m = 0.309 \pm 0.014$ and $\sigma_8 = 0.815 \pm 0.022$. Both results indicate that the cluster mass uncertainty (fractional or intrinsic) does not affect our constraints on Ω_m and σ_8 using `SelFMC`.

Mass Threshold

The second systematic uncertainty comes from the difficulty of determining accurately the mass threshold at which the sample is mass complete. As discussed in § 4.3.1 and Figure 4.1 the catalog is approximately complete around $\log M \gtrsim 13.9$ $[h^{-1}\ M_\odot]$. However, the mass threshold at which the sample is mass-complete is not accurately specified. Therefore, we investigate the effect of varying the mass threshold $\log M$ between 13.8 and 14.0 $[h^{-1}\ M_\odot]$ in steps of 0.05 dex on the recovered cosmological constraints from our analysis.

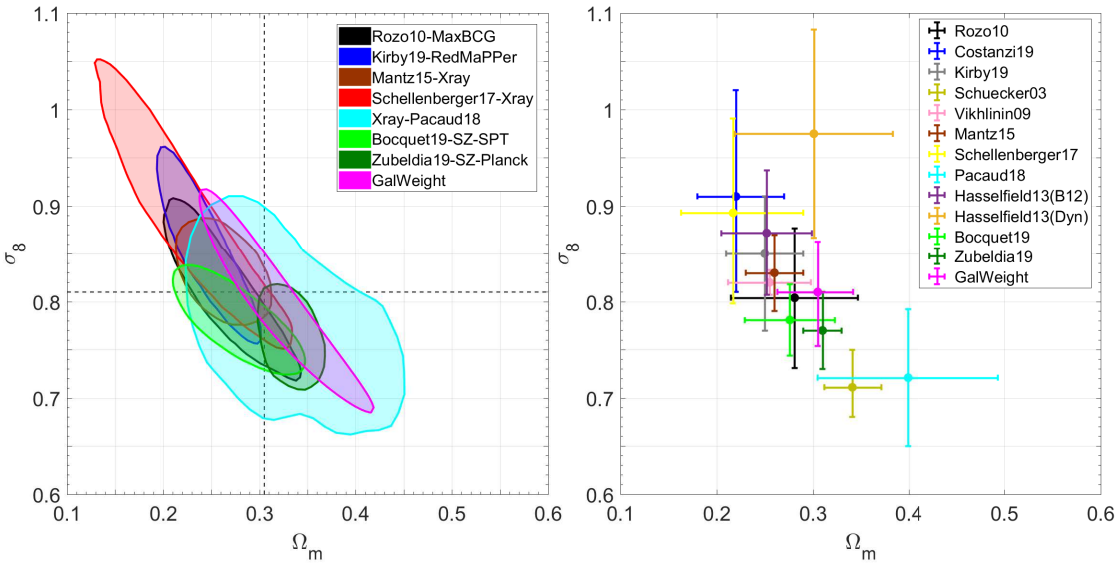

Figure 4.7: Constraints on Ω_m and σ_8 obtained from cluster abundance studies (cluster mass function; CMF). Left: 68% confidence levels (CLs) derived from `SelFMC` (magenta) plus select other optical, X-ray or SZ-detected cluster catalogs as shown in the legend and summarized in the first three sections of Table 4.2. The two dashed lines show the best-fit values derived in this work. Right: Uncertainties on Ω_m and σ_8 for each of the cluster abundance studies listed in Table 4.2 (Note: For clarity, not all studies in Table 4.2 are shown in the left panel). While in agreement with the other cluster abundance studies within 1σ uncertainties, the value of Ω_m determined from our work is slightly higher and the value of σ_8 slightly lower than most of the other studies. As shown in Fig 4.8 and discussed in § 4.5.3, we note that our values are in better agreement with Ω_m and σ_8 obtained from non-cluster determinations as shown in Fig 4.8.

For each mass threshold we calculate the χ^2 likelihood and then we obtain the joint 68% CL of all χ^2 distributions as shown in the middle panel of Figure 4.6. The plot shows that the best fit values of Ω_m and σ_8 deviate very slightly from the results of the fiducial sample with $\Omega_m = 0.300^{+0.015}_{-0.017}$ and $\sigma_8 = 0.820^{+0.020}_{-0.023}$.

Table 4.2: Comparison of constraints on cosmological parameters Ω_m and σ_8 derived from Clusters Abundances (CMF) and from Other Cosmological Probes, including cosmic shear, galaxy-galaxy lensing, angular clustering, BAO, supernovae, and CMB

Sample	Mass estimation	Ω_m	σ_8	S_8 [(a)]	Δ_{pl} [(b)]	ref
spectroscopically-selected catalogs — cluster abundance						
`GalWCat19`	virial theorem	$0.305^{+0.037}_{-0.042}$	$0.810^{+0.053}_{-0.056}$	0.817	0.032	
optical photometrically-selected catalogs — cluster abundance						
MaxBCG	rich-mass	$0.281^{+0.066}_{-0.066}$	$0.804^{+0.073}_{-0.073}$	0.779	0.108	[1]
RedMaPPer	rich-mass	$0.220^{+0.050}_{-0.040}$	$0.910^{+0.110}_{-0.100}$	0.778	0.325	[2]
RedMaPPer	rich-mass	$0.250^{+0.040}_{-0.040}$	$0.850^{+0.06}_{-0.08}$	0.776	0.212	[3]
x-rays catalogs — cluster abundance						
REFLEX	lum-mass	$0.341^{+0.030}_{-0.029}$	$0.711^{+0.039}_{-0.031}$	0.758	0.148	[4]
Chandra	lum-mass	$0.255^{+0.043}_{-0.043}$	$0.820^{+0.013}_{-0.013}$	0.757	0.191	[5]
WtG [(c)]	lum-mass	$0.260^{+0.030}_{-0.030}$	$0.830^{+0.04}_{-0.04}$	0.773	0.176	[6]
HIFLUGCS	lum-mass	$0.217^{+0.073}_{-0.054}$	$0.893^{+0.098}_{-0.095}$	0.760	0.327	[7]
XMM-XXL	temp-mass	$0.399^{+0.094}_{-0.094}$	$0.721^{+0.071}_{-0.071}$	0.832	0.289	[8]
SZ catalogs — cluster abundance						
ACT, [B12]	SZ-mass	$0.252^{+0.047}_{-0.047}$	$0.872^{+0.065}_{-0.065}$	0.799	0.214	[9]
ACT, [Dyn]	SZ-mass	$0.301^{+0.082}_{-0.082}$	$0.975^{+0.108}_{-0.108}$	0.977	0.207	[10]
SPT	SZ-mass	$0.276^{+0.047}_{-0.047}$	$0.781^{+0.037}_{-0.037}$	0.776	0.129	[11]
HECS-SZ	SZ-mass	–	–	0.751	–	[12]
Planck18	SZ-mass	$0.310^{+0.020}_{-0.020}$	$0.770^{+0.040}_{-0.040}$	0.783	0.138	[13]
other cosmological probes						
DES-Y1	CS+GL+AC [(d)]	$0.270^{+0.041}_{-0.040}$	$0.820^{+0.038}_{-0.036}$	0.778	0.143	[14]
KiDS+GAMA	CS+GGL+AC	$0.315^{+0.068}_{-0.092}$	$0.785^{+0.111}_{-0.117}$	0.804	0.032	[15]
Pantheon	SNe	$0.307^{+0.012}_{-0.012}$	—	—	—	[16]
6dF+DR7+BOSS [(e)]	BAO	$0.346^{+0.045}_{-0.045}$	—	—	—	[17]
WMAP9	CMB only	$0.280^{+0.041}_{-0.040}$	$0.820^{+0.038}_{-0.036}$	0.792	0.112	[18]
Planck18	CMB only	$0.315^{+0.007}_{-0.007}$	$0.811^{+0.006}_{-0.006}$	0.832	0.000	[19]

(a) The cluster normalization condition parameter, S_8, is defined as $S_8 = \sigma_8(\Omega_m/0.3)^{0.5}$ as used in the literature. (b) $\Delta_{pl} = \sqrt{\left[(\Omega_{m,ref} - \Omega_{m,pl})/\Omega_{m,pl}\right]^2 + \left[(\sigma_{8,ref} - \sigma_{8,pl})/\sigma_{8,pl}\right]^2}$ is the scatter of Ω_m and σ_8 obtained from each method listed the table relative to that obtained from Planck18 (Planck Collaboration et al., 2018). (c) Mantz et al. (2015) used the combination of luminosity, temperature, gas mass, and lensing mass to estimate cluster mass which were refereed to as Weighting the Giant (WtG) (d) CC = cosmic shear, GL = galaxy-galaxy lensing, AC = angular clustering. (e) 6dF = Six Degree Field Galaxy Survey (Beutler et al., 2011), DR7 = SDSS data release 7 (Ross et al., 2015), BOSS = Baryon Oscillation Spectroscopic Survey (Alam et al., 2017). Reference: [1]=Rozo et al., 2010, [2]=Costanzi et al., 2019, [3]=Kirby et al., 2019, [4]=Schuecker et al., 2003, [5]=Vikhlinin et al., 2009b, [6]=Mantz et al., 2015, [7]=Schellenberger & Reiprich, 2017, [8]=Pacaud et al., 2018, [9]=Hasselfield et al., 2013, [10]= Hasselfield et al., 2013, [11]= Bocquet et al., 2019, [12]=Ntampaka et al., 2019, [13]=Zubeldia & Challinor, 2019, [14]=Abbott et al., 2018b, [15]=van Uitert et al., 2018, [16]=Scolnic et al., 2018, [17]=Alam et al., 2017, [18]=Hinshaw et al., 2013, [19]=Planck Collaboration et al., 2018.

Selection Function Parameterization

The constraints on Ω_m and σ_8 is affected by parameterization of the selection function. Our selection function depends on three parameters a, b, and γ. The normalization a is already fixed to unity. Assuming a normal distribution, the systematic of the selection function is investigated by generating $\sim$ 8000 pairs of b and γ, using the uncertainty in b and γ (see § 4.3.1). For each pair we estimate the best fit values of Ω_m and σ_8. Figure 4.6 shows the 68% CL for the systematic of the selection function. This analysis rotates the error ellipses slightly compared to our fiducial analysis, but does not affect our results. We obtain $\Omega_m = 0.313 \pm 0.035$ and $\sigma_8 = 0.809 \pm 0.012$, which is consistent with our result of the fiducial sample.

4.5.2 Comparison with external data from cluster abundance

The left panel of Figure 4.7 introduces the 68% confidence level (CL) derived from `SelFMC` in comparison to the results obtained from other cluster abundance studies. Samples of galaxy cluster constructed from galaxy surveys include optical photometric (e.g., Kirby et al., 2019), X-ray (e.g., Mantz et al., 2015), and SZ (e.g., Zubeldia & Challinor, 2019) catalogs as listed in Table 4.2. The figure shows that the CLs of all cluster abundance studies introduce a degeneracy between Ω_m and σ_8 as we discussed in § 4.4.2. Also, the CL derived from `SelFMC` overlaps the CLs obtained from all other results as shown in the figure. Regardless of this overlapping, the right panel of Figure 4.7 shows that the constraints on Ω_m and σ_8 from cluster abundance studies are in tension with each other, even for the studies that use the same type of cluster sample. Specifically, the X-ray independent studies listed

in Table 4.2 introduce different values of Ω_m and σ_8, which vary from ~ 0.22 to 0.40 and 0.71 to 0.89, respectively. Also, the independent studies that use SZ-cluster samples show that Ω_m and σ_8 vary from ~ 0.25 to 0.31 and 0.77 to 0.98, respectively.

The question is now, why are the cosmological constraints derived from many of the cluster abundance techniques in tension with each other? All cluster samples constructed from photometric surveys or detected by SZ effect do not return an estimate of each cluster's mass directly. For such samples the cluster mass has to be inferred indirectly from other observables, which scale tightly with cluster mass. Among these mass proxies are X-ray luminosity, temperature, the product of X-ray temperature and gas mass (e.g., Vikhlinin et al., 2009b; Mantz et al., 2016), richness (e.g., Yee & Ellingson, 2003; Simet et al., 2017), and SZ signal (e.g., Bocquet et al., 2019). To estimate cluster masses for the clusters in these samples it is necessary to follow up a subset of clusters and calculate their masses using, e.g., weak lensing or x-ray observations. Then, an observable-mass relation can be calibrated for these subsamples. Finally, the mass of each cluster in the sample can be estimated from this scaling relation. However, this reliance on observable-mass proxies introduces significant systematic uncertainties which is the dominant source of error (e.g., Henry et al., 2009; Mantz et al., 2015) for the reasons explained in the next paragraph.

Firstly, the masses obtained for the follow-up subsample of clusters are often biased. For example, it is known that X-ray mass estimates are typically biased low and so a mass bias factor, (1-β), needs to be introduced and calibrated. Secondly, the size of the subsample used for calibration is usually small (tens of clusters) which introduces large uncertainties in both the slope and the normalization of the scaling relation. Thirdly,

many cluster catalogs span a large redshift range so evolution (due to both the evolution of the universe and the physical processes of baryons in clusters) in the the scaling-relations used to estimate the masses needs to be carefully handled, introducing another source of uncertainty. All of the aforementioned assumptions can introduce large uncertainties in the estimates of cluster mass and consequently the constraints on cosmological parameters. For instance, σ_8 is specifically very sensitive to the high-mass end of the CMF and any offset of cluster true masses leads to biased estimation of σ_8. Other observational systematics that introduce additional uncertainties are photometric redshift errors and cluster miscentering.

By using the `GalWCat19` cluster catalog and deriving cluster masses using the virial theorem, we were able to avoid most of the complexities described above. Firstly, we were able to identify clusters, assign membership, and determine cluster centers and redshifts with high accuracy from the high-quality SDSS spectroscopic data set. Secondly, cluster membership was determined by the GalWeight technique which has been shown to be $\sim$ 98% accurate in assigning cluster membership (Abdullah+18). Thirdly, a mass for each cluster was determined directly using the virial theorem. Therefore, we were able to recover a total (dark plus baryonic) mass for each cluster and circumvent having to make any assumptions about the complicated physical processes associated with the baryons. It has been suggested that cluster masses estimated via the virial theorem are overestimated by 20%. But we note that we have applied a correction for the surface pressure term which we believe decreases this bias, especially when applied in combination with our GalWeight membership technique (Abdullah+18). Abdullah+20 showed that the virial mass estimator performed well in comparison to the other mass estimators described in Old et al., 2015, and

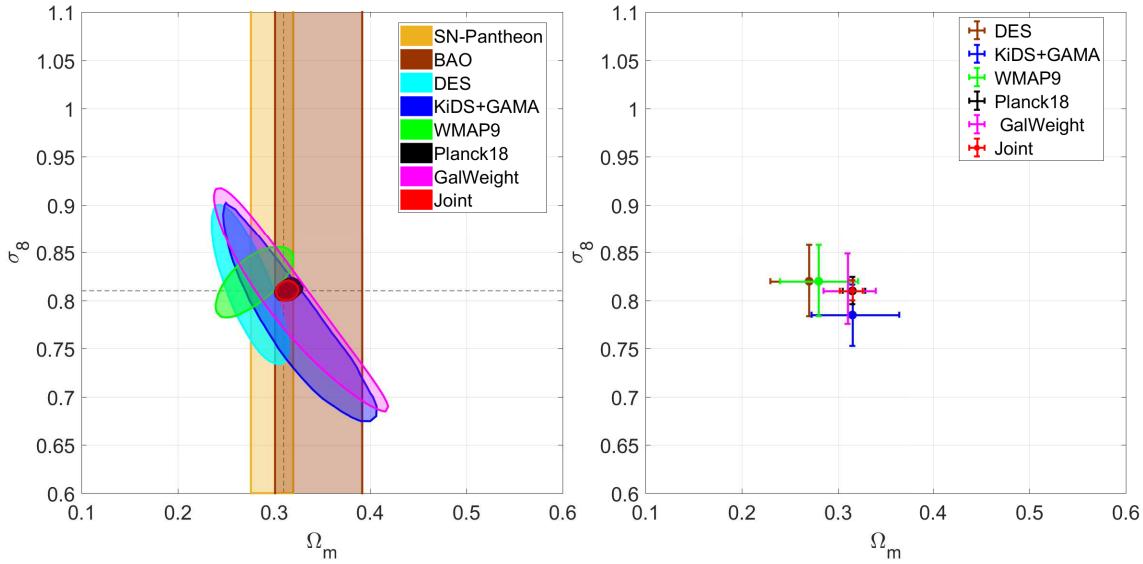

Figure 4.8: Constraints on Ω_m and σ_8 obtained from cluster abundance (`SelFMC`; magenta) and non-cluster cosmological constraint methods. Left: 68% confidence levels (CLs) derived from `SelFMC`, WMAP9 (CMB; Hinshaw et al., 2013), Planck18 (CMB; Planck Collaboration et al., 2018), BAO data (Beutler et al., 2011; Ross et al., 2015; Alam et al., 2017), Pantheon sample (SNe; Scolnic et al., 2018), and the surveys KiDS+GAMA (van Uitert et al., 2018) and DES Y1 (Abbott et al., 2018b) which both use the cosmological probes of cosmic shear, galaxy-galaxy lensing, and angular clustering. As in Figure 4.7, the two dashed lines show the best-fit values derived in this work. The constraints on Ω_m and σ_8 derived from `SelFMC` are consistent with those derived from the non-cluster methods. Joint analysis between our constraints and the results of Planck18+BAO+Pantheon is represented by the red contour line. Right: uncertainties of Ω_m and σ_8 estimated for the aforementioned probes except for the BAO and SNe probes which constrain Ω_m only.

resulted in a relatively low bias and scatter when applied to two semi-analytical simulations (see Figure 3 in Abdullah+20). Fourthly, since `GalWCat19` is a low-redshift cluster catalog it eliminates the need to make any assumptions about evolution in clusters themselves and evolution in cosmological parameters. Finally, because of the large size of the `GalWCat19` we are able to determining the CMF well and consequently constrain the cosmological parameters Ω_m and σ_8 with high precision.

4.5.3 Comparison with external data from non-cluster cosmological probes

Cosmological parameters can be estimated from different cosmological probes rather than cluster abundance studies. We use measurements of primary CMB anisotropies from both WMAP (9-year data; Hinshaw et al., 2013) and Planck satellites focused on the TT+lowTEB data combination from the 2018 analyses (Planck Collaboration et al., 2018). We also use angular diameter distances as probed by Baryon Acoustic Oscillations (BAO) including the 6dF Galaxy Survey (Beutler et al., 2011), the SDSS Data Release 7 (Ross et al., 2015), and the BOSS Data Release 12 (Alam et al., 2017). Furthermore, we use measurements of luminosity distances from Type Ia supernovae from the Pantheon sample (Scolnic et al., 2018). Finally, we use the measurements from a joint analysis of three cosmological probes: cosmic shear, galaxy-galaxy lensing, and angular clustering, including the results of the Kilo Degree Survey and the Galaxies And Mass Assembly survey (KiDS+GAMA; van Uitert et al., 2018) and the first year of the Dark Energy Survey (DES Y1; Abbott et al., 2018b) (see Table 4.2). The left panel of Figure 4.8 introduces the 68% CL derived from `SelFMC` in comparison to the those obtained from the aforementioned cosmological probes. As shown, the CL derived from `SelFMC` overlaps the CLs obtained from

all non-cluster abundance probes.

We define the scatter

$$\Delta_{pl} = \sqrt{\left(\frac{\Omega_{m,ref} - \Omega_{m,pl}}{\Omega_{m,pl}}\right)^2 + \left(\frac{\sigma_{8,ref} - \sigma_{8,pl}}{\sigma_{8,pl}}\right)^2}, \tag{4.10}$$

to compare the constraints on Ω_m and σ_8 obtained from all cosmological probes which are listed in Table 4.2 with that obtained from Planck18 (Planck Collaboration et al., 2018). Note that the constraints on Ω_m and σ_8 derived from most of the cluster abundance studies independently introduce a relatively large scatter compared to the CMB experiment of Planck18. However, our constraints on Ω_m and σ_8 are very comparable and competitive with Planck18 with a minimum value of $\Delta_{pl} = 0.018$. Moreover, our constraint on Ω_m is in excellent agreement with the results of the BAO and Pantheon, separately. This remarkable consistency demonstrates that our derived cluster catalog at low redshift and calculating cluster masses using spectroscopic database of galaxy surveys is essential to obtain robust cosmological parameters. These results also emphasize the necessarily need to construct accurate cluster catalogs at high redshifts using the ongoing and upcoming galaxy surveys and perform similar analyses as introduced in this work.

As discussed above there is a degeneracy between Ω_m and σ_8 derived from the CMF at low redshift. We combine our 68% CL with those obtained from Planck18+BAO+Pantheon, to eliminate the degeneracy of the our likelihood and to remarkably shrink the uncertainties of the cosmological parameters. The joint analysis gives $\Omega_m = 0.315^{+0.013}_{-0.011}$ and $\sigma_8 = 0.810^{+0.011}_{-0.01}$.

4.5.4 Conclusion

In this paper, we derived the CMF and the cosmological parameters Ω_m and σ_8 using a mass-complete subsample of 756 clusters (`SelFMC`) obtained from the `GalWCat19` cluster catalog which was constructed from SDSS-DR13 spectroscopic data set. The advantages of using this catalogs are: i) we were able to identify clusters, assign membership, and determine cluster centers and redshifts with high accuracy from the high-quality SDSS spectroscopic data set; ii) cluster membership was determined by the GalWeight technique which has been shown to be $\sim$ 98% accurate in assigning cluster membership (Abdullah+18); iii) the cluster masses were calculated individually using the virial theorem, and corrected for the surface pressure term; iv) `GalWCat19` is a low-redshift cluster catalog which eliminates the need to make any assumptions about evolution in clusters themselves and evolution in cosmological parameters; v) the size of `GalWCat19` is one of the largest available spectroscopic samples to be a fair representation of the cluster population.

Our CMF closely matches predictions from MultiDark Planck N-body simulations (snapshot hlist_0.91520.list[8], with $z \sim 0.09$) for $\log(M) \gtrsim 13.9\ h^{-1}\ M_{\odot}$. Assuming a flat ΛCDM cosmology, we used the publicly available `HMFcalc` [9] code (Murray et al., 2013a) to estimate HMFs for the Tinker08 model (Equation 4.5). Then, using a standard χ^2 procedure, we compared our cumulative mass function to HMFs to determine the best-fit mass function and constrain Ω_m and σ_8. We measured Ω_m and σ_8 to be $\Omega_m = 0.310^{+0.023}_{-0.027} \pm 0.041$ (systematic) and $\sigma_8 = 0.810^{+0.031}_{-0.036} \pm 0.035$ (systematic), with a cluster normalization relation of $\sigma_8 = 0.43\Omega_m^{-0.55}$.

[8] https://www.cosmosim.org/data/catalogs/NewMD_3840_Planck1/ROCKSTAR/trees/hlists/
[9] http://hmf.icrar.org/

The cosmological constraints we derived are very competitive with those recently derived using both cluster abundance studies and other cosmological probes. In particular, our constraint on Ω_m and σ_8 are consistent with Planck18+BAO+Pantheon constraints. This remarkable consistency highlights the potential of using `GalWCat19` and its subsample `SelFMC` which are derived from SDSS-DR13 spectroscopic data set utilizing the application of GalWeight to produce precision constraints on cosmological parameters. The joint analysis of our cluster data with Planck18+BAO+Pantheon gives $\Omega_m = 0.315^{+0.011}_{-0.013}$ and $\sigma_8 = 0.810^{+0.011}_{-0.010}$.

ACKNOWLEDGMENTS

We would like to thank Steven Murray for making his `HMFcalc` calculator publicly available, and also for his guidance in running it. We also would like to thank Jeremy Tinker, Brian Siana, and Benjamin Forrest for their useful comments and help and Shadab Alam for providing us with the chain of BOSS-DR12 BAO data. Finally, we appreciate the comments and suggestions of the reviewer, which improved this paper. This work is supported by the National Science Foundation through grant AST-1517863, by HST program number GO-15294, and by grant number 80NSSC17K0019 issued through the NASA Astrophysics Data Analysis Program (ADAP). Support for program number GO-15294 was provided by NASA through a grant from the Space Telescope Science Institute, which is operated by the Association of Universities for Research in Astronomy, Incorporated, under NASA contract NAS5-26555.

Evolution

In this section, we discuss the evolution effect for a sample of clusters with a narrow redshift range between z_1 and z_2 with an average of $\langle z \rangle$. The HMF depends on the mass and redshift and is given by $\int_{z_1}^{z_2} n(M,z)dz/(z_2 - z_1)$. We test the effect of evolution assuming an analytical model for the evolution of HMF and cosmological model with reasonable parameters. We then take the integral $\int_{z_1}^{z_2} n(M,z)dz/(z_2 - z_1)$ and compare the results with $n(M,z)$ at $z = 0.085$.

Figure 4.9 shows the evolution of the cluster number density expected by Tinker08 for cosmological parameters Ω_m= 0.305 and σ_8= 0.825. In the left panel, we plot the HMF times M/ρ_c, ρ_c is the critical density of the universe, to clarify the differences between the models at different redshifts. The right panel shows the scatter of models relative to the expectation at $z = 0.085$ (black line). As expected, the evolution of clusters with $z < 0.085$ is less than unity relative to that at $z = 0.085$ and the evolution of clusters with $z > 0.085$ is larger than unity relative to that at $z = 0.085$. The two dashed lines shows the expectation $[\int_{z_1}^{z_2} n(M,z)dz/(z_2 - z_1)]$ in the redshift intervals of $0.0 \leq z \leq 0.125$ (brown) and $0.045 \leq z \leq 0.125$ (red). The plot indicates that the evolution is $> 15\%$ for $0.0 \leq z \leq 0.125$ for massive clusters, while it drops to $< 3\%$ for $0.045 \leq z \leq 0.125$.

Note that we do not neglect the effects of evolution. In other words, we do not assume that the HMF at z_1 is (nearly) the same as at z_2 (admittedly, there is 10-20% difference in the most massive M). Because we use ratios of these quantities, most of the cosmological parameters (e.g., σ_8) are canceled for sensible range (e.g., σ_8= 0.75-0.85). We also test other HMF approximations such as Despali HMF (**?**) and obtain the same

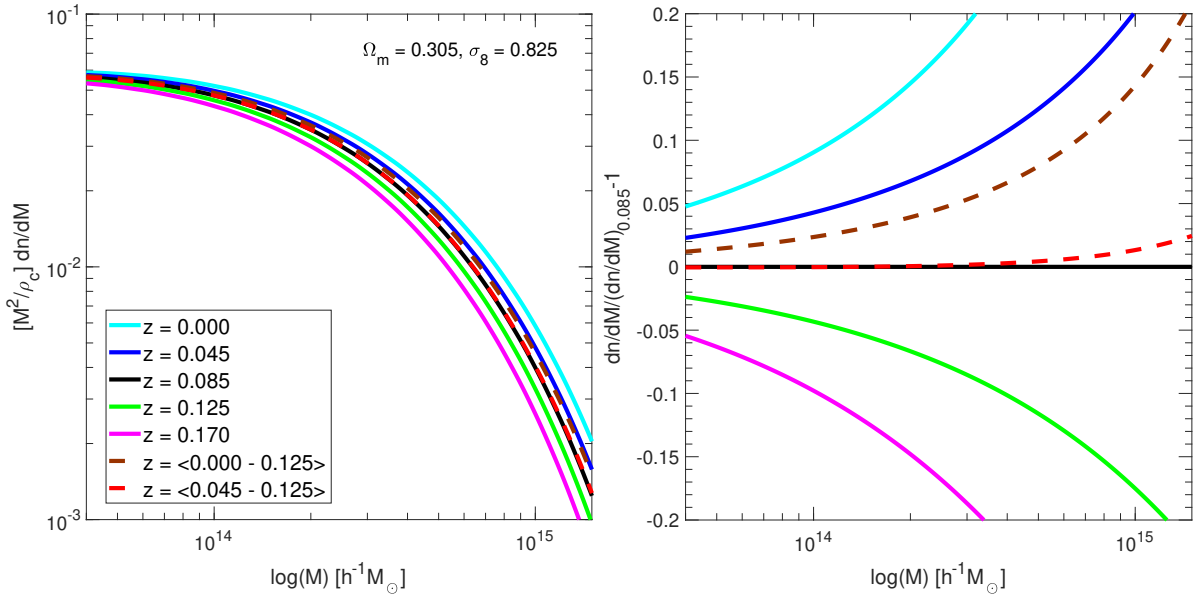

Figure 4.9: The effect of cluster number density evolution. **Left**: Tinker08 HMF times M^2/ρ_c at different redshifts as well as the average HMF for $0.0 \leq z \leq 0.125$ (brawn) and $0.045 \leq z \leq 0.125$ (red) as shown in the legend. **Right**: The scatter of each HMF relative to that at $z = 0.085$ (the mean redshift of the sample).

conclusion. Therefore, we restrict our data (observed clusters) to $0.045 \leq z \leq 0.125$ for which the evolution effect of the number density of clusters is minimal.

Redshift Threshold

In this section we investigate the choice of the redshift interval and the application on the selection function of our results of the fiducial analysis as shown in Figure 4.6. In the left panel, we fix the upper redshift threshold to 0.125 and decrease the lower redshift threshold from 0.075 to 0.045. The plots indicates that decreasing the lower redshift threshold does not affect our result of the fiducial sample (black ellipse). It also demonstrates that the evolution effect is unremarkable in this small redshift interval. The left panel also

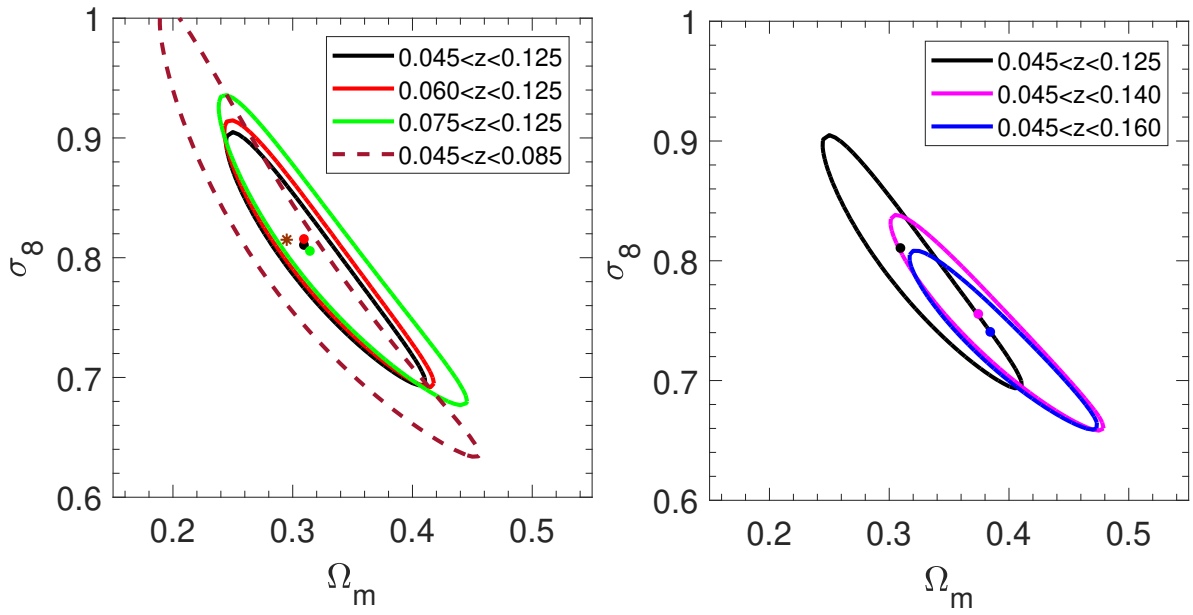

Figure 4.10: The effect of adopting the redshift threshold. **Left**: 68% CLs for three subsamples with fixing the upper redshift threshold to 0.125 and decreasing the lower redshift threshold from 0.075 to 0.045. The dashed brown ellipse represents the 68% CL of the `NoSelFVC` sample. **Right**: 68% CLs for three subsamples with fixing the lower redshift threshold to 0.045 and increasing the upper redshift threshold from 0.125 to 0.16.

introduces the 68% CL of the `NoSelFVC` sample (dashed brown ellipse) which gives $\Omega_m = 0.295^{+0.033}_{-0.034}$ (5% less than the fiducial value) and $\sigma_8 = 0.815^{+0.049}_{-0.050}$ (1% greater than the fiducial value). The consistency between the results of `SelFMC` and `NoSelFVC` demonstrates that applying the selection function for $z \leq 0.125$ does not affect the results of the fiducial analysis and is sufficient to correct for the volume incompleteness of `GalWCat19`. In the right panel, we fix the lower redshift threshold to 0.045 and increase the upper redshift threshold from 0.125 to 0.16. The plots indicates that increasing the upper redshift threshold significantly affects our constraints on Ω_m and σ_8 because applying the selection function to higher redshift (> 0.125) affects the shape of the CMF by increasing the scatter and noise and overcorrecting the number of clusters at high redshifts.

Chapter 5

Conclusions and Future Work

5.1 Conclusions

The dissertation included three publications which were discussed in chapters two, three, and four. In chapter two, we introduced a new technique (GalWeight) for assigning galaxy cluster membership. We showed that the technique can be applied to both massive galaxy clusters and poor galaxy groups. It also can be used to identify members in both the virial and infall regions with high efficiency. We applied the GalWeight technique to MDPL2 & Bolshoi N-body simulations, and found that it is $> 98\%$ accurate in correctly assigning cluster membership.

In chapter three, we applied the GalWeight technique to the SDSS-DR13 spectroscopic data set to create a new publicly-available catalog of 1800 galaxy clusters (GalWeight cluster catalog, `GalWCat19`) and a corresponding catalog of 34471 identified member galaxies. The clusters were identified from overdensities in redshift-phase space by looking for the Finger-of-God effect. The cluster masses were calculated using the virial theorem, corrected

for the surface pressure term and NFW model. The 1800 `GalWCat19` clusters range in redshift between $0.01 - 0.2$ and in mass between $(0.4 - 14) \times 10^{14} h^{-1} M_{\odot}$. The cluster catalog provides a large number of cluster parameters including sky position, redshift, membership, velocity dispersion, and mass at overdensities $\Delta = 500, 200, 100, 5.5$. The 34471 member galaxies are identified within the radius at which the density is 200 times the critical density of the Universe. The galaxy catalog provides the coordinates of each galaxy and the ID of the cluster that the galaxy belongs to.

In chapter four, we derived cosmological constraints on Ω_m and σ_8 using `GalWCat19`. By analyzing the `SelFMC` sample, we obtained $\Omega_m = 0.310^{+0.023}_{-0.027} \pm 0.041$ (systematic) and $\sigma_8 = 0.810^{+0.031}_{-0.036} \pm 0.035$ (systematic), with a cluster normalization relation of $\sigma_8 = 0.43\Omega_m^{-0.55}$. Our constraints on Ω_m and σ_8 are consistent and very competitive with those obtained from non-cluster abundance cosmological probes such as CMB, BAO, and SNe. The joint analysis of our cluster data with Planck18+BAO+Pantheon gave $\Omega_m = 0.315^{+0.013}_{-0.011}$ and $\sigma_8 = 0.810^{+0.011}_{-0.010}$.

5.2 Ongoing Work

5.2.1 Cluster Richness-Mass Relation

I am studying the evolution of the richness-mass relation by identifying clusters from the GOGREEN galaxy survey at redshift z $\sim$ 1 utilizing the GalWeight technique and using the RedMaPPer (Rykoff et al., 2014, 2016) and the `GalWeight19` cluster catalogs. The project aims to introducing this relationship to estimate cluster masses of the RedMaPPer catalog to constrain cosmological parameters from RedMaPPer.

5.2.2 Galaxy Stellar Mass Function of numerical simulations

I am conducting a study of the galaxy stellar mass function (SMF) of hydrodynamical simulations (EAGLE, Illustris and TNG) and semi-analytical models (Galacticus) for $0 < z < 3$. The project aims to study the evolution of galaxy stellar mass in different environments and for different galaxy types (quiescent vs. star-forming and central vs. satellite) to understand the mechanisms of how galaxies build their masses and the physical processes that govern galaxy formation and evolution in halos. This project to improve the current models of galaxy evolution and understand the physical processes that govern galaxy evolution in clusters.

5.3 Future Work

5.3.1 Connection between Galaxies and Hosting Clusters

Investigating the evolution of the properties of galaxy clusters sheds light on the physical processes regulating galaxy evolution (e.g., Erfanianfar et al., 2019. The correlations between properties of brightest cluster galaxies (BCGs), usually located at the center of galaxy clusters, and their host galaxy clusters allow us to understand the environmental effect of the host clusters on the formation and evolution of the central galaxies. Using the `GalWeight19` and other cluster catalogs at different redshifts and utilizing numerical simulations, I am interested in studying the BCG stellar mass-halo mass relation, and the fraction of early- and late-type galaxies as a function of radius from the cluster center. These studies shed light on the connection between the galaxies and their hosting clusters, allowing us to test the current models of galaxy formation and evolution with observations.

5.3.2 Velocity Bias between Galaxies and Dark Matter

Studying the velocity bias (the difference in the velocity fields of dark matter and galaxies) is a key tool in understanding the formation mechanisms of galaxies in clusters and their evolution with time. A large uncertainty in estimating dynamical cluster mass and extracting cosmological information from observations is due to the bias between galaxies and dark matter (the systematic of the assumption that galaxies follows dark matter). Comparing the velocity distribution of galaxies in clusters with the expectation of pure nbody simulations allows us to investigate this bias. This bias is due to the effect of baryons on the dynamics of galaxies in clusters. Investigating the hydrodynamical simulations and semi-analytic models allows us to understand the physics behind this effect to improve the current models of galaxy formation and evolution.

Bibliography

Abbott, T. M. C., Abdalla, F. B., Alarcon, A., et al. 2018a, Phys. Rev. D, 98, 043526

Abbott, T. M. C., Abdalla, F. B., Allam, S., et al. 2018b, ApJS, 239, 18

Abdullah, M. H., Ali, G. B., Ismail, H. A., & Rassem, M. A. 2011, MNRAS, 416, 2027

Abdullah, M. H., Klypin, A., & Wilson, G. 2020a, arXiv e-prints, arXiv:2002.11907

Abdullah, M. H., Praton, E. A., & Ali, G. B. 2013, MNRAS, 434, 1989

Abdullah, M. H., Wilson, G., & Klypin, A. 2018, ApJ, 861, 22

Abdullah, M. H., Wilson, G., Klypin, A., et al. 2020b, ApJS, 246, 2

Abell, G. O., Corwin, Jr., H. G., & Olowin, R. P. 1989, ApJS, 70, 1

Adami, C., Mazure, A., Katgert, P., & Biviano, A. 1998, A&A, 336, 63

Aguerri, J. A. L., Sánchez-Janssen, R., & Muñoz-Tuñón, C. 2007, A&A, 471, 17

Akeson, R., Armus, L., Bachelet, E., et al. 2019, arXiv e-prints, arXiv:1902.05569

Alam, S., Albareti, F. D., Allende Prieto, C., et al. 2015, ApJS, 219, 12

Alam, S., Ata, M., Bailey, S., et al. 2017, MNRAS, 470, 2617

Albareti, F. D., Allende Prieto, C., Almeida, A., et al. 2017, ApJS, 233, 25

Alpaslan, M., Robotham, A. S. G., Driver, S., et al. 2012, MNRAS, 426, 2832

Amendola, L., Appleby, S., Bacon, D., et al. 2013, Living Reviews in Relativity, 16, 6

Andreon, S., Trinchieri, G., Moretti, A., & Wang, J. 2017, A&A, 606, A25

Annunziatella, M., Biviano, A., Mercurio, A., et al. 2014, A&A, 571, A80

Armitage, T. J., Barnes, D. J., Kay, S. T., et al. 2018, MNRAS, 474, 3746

Bahcall, J. N., & Tremaine, S. 1981, ApJ, 244, 805

Bahcall, N. A. 1988, ARA&A, 26, 631

Bahcall, N. A., Dong, F., Bode, P., et al. 2003, ApJ, 585, 182

Baldry, I. K., Glazebrook, K., Brinkmann, J., et al. 2004, ApJ, 600, 681

Baldry, I. K., Driver, S. P., Loveday, J., et al. 2012, MNRAS, 421, 621

Balogh, M., Eke, V., Miller, C., et al. 2004, MNRAS, 348, 1355

Balogh, M. L., Navarro, J. F., & Morris, S. L. 2000, ApJ, 540, 113

Banerjee, P., Szabo, T., Pierpaoli, E., et al. 2018, NewA, 58, 61

Bartelmann, M. 1996, A&A, 313, 697

Battye, R. A., & Weller, J. 2003, Phys. Rev. D, 68, 083506

Baugh, C. M. 2006, Reports on Progress in Physics, 69, 3101

Bayliss, M. B., Ruel, J., Stubbs, C. W., et al. 2016, ApJS, 227, 3

Beers, T. C., Flynn, K., & Gebhardt, K. 1990, AJ, 100, 32

Behroozi, P. S., Wechsler, R. H., & Conroy, C. 2013a, ApJ, 770, 57

Behroozi, P. S., Wechsler, R. H., & Wu, H.-Y. 2013b, ApJ, 762, 109

Behroozi, P. S., Wechsler, R. H., Wu, H.-Y., et al. 2013c, ApJ, 763, 18

Bellagamba, F., Roncarelli, M., Maturi, M., & Moscardini, L. 2018, MNRAS, 473, 5221

Benson, A. J., & Bower, R. 2011, MNRAS, 410, 2653

Betoule, M., Kessler, R., Guy, J., et al. 2014, A&A, 568, A22

Beutler, F., Blake, C., Colless, M., et al. 2011, MNRAS, 416, 3017

Bhattacharya, S., Heitmann, K., White, M., et al. 2011, ApJ, 732, 122

Binney, J., & Tremaine, S. 1987

Biviano, A., Murante, G., Borgani, S., et al. 2006, A&A, 456, 23

Blanton, M. R., & Moustakas, J. 2009, ARA&A, 47, 159

Blanton, M. R., Hogg, D. W., Bahcall, N. A., et al. 2003, ApJ, 592, 819

Bocquet, S., Saro, A., Dolag, K., & Mohr, J. J. 2016, MNRAS, 456, 2361

Bocquet, S., Saro, A., Mohr, J. J., et al. 2015, ApJ, 799, 214

Bocquet, S., Dietrich, J. P., Schrabback, T., et al. 2019, ApJ, 878, 55

Brennan, R., Pandya, V., Somerville, R. S., et al. 2015, MNRAS, 451, 2933

Bryan, G. L., & Norman, M. L. 1998, ApJ, 495, 80

Busha, M. T., Evrard, A. E., Adams, F. C., & Wechsler, R. H. 2005, MNRAS, 363, L11

Busha, M. T., Wechsler, R. H., Behroozi, P. S., et al. 2011, ApJ, 743, 117

Butcher, H., & Oemler, Jr., A. 1978, ApJ, 219, 18

Carlberg, R. G., Yee, H. K. C., & Ellingson, E. 1997, ApJ, 478, 462

Carlberg, R. G., Yee, H. K. C., Ellingson, E., et al. 1996, ApJ, 462, 32

Cattaneo, A., Dekel, A., Faber, S. M., & Guiderdoni, B. 2008, MNRAS, 389, 567

Cole, S., Norberg, P., Baugh, C. M., et al. 2001, MNRAS, 326, 255

Cole, S., Percival, W. J., Peacock, J. A., et al. 2005, MNRAS, 362, 505

Cooper, M. C., Newman, J. A., Madgwick, D. S., et al. 2005, ApJ, 634, 833

Costanzi, M., Rozo, E., Simet, M., et al. 2019, MNRAS, 488, 4779

Courtin, J., Alimi, J.-M., Rasera, Y., et al. 2010, in American Institute of Physics Conference Series, Vol. 1241, American Institute of Physics Conference Series, ed. J.-M. Alimi & A. Fuözfa, 804

Crocce, M., Fosalba, P., Castander, F. J., & Gaztañaga, E. 2010, MNRAS, 403, 1353

Croton, D. J., Springel, V., White, S. D. M., et al. 2006, MNRAS, 365, 11

Croton, D. J., Stevens, A. R. H., Tonini, C., et al. 2016, ApJS, 222, 22

Daddi, E., Dickinson, M., Morrison, G., et al. 2007, ApJ, 670, 156

Dahle, H. 2006, ApJ, 653, 954

Danese, L., de Zotti, G., & di Tullio, G. 1980, A&A, 82, 322

Darvish, B., Mobasher, B., Sobral, D., Scoville, N., & Aragon-Calvo, M. 2015, ApJ, 805, 121

Davies, L. J. M., Robotham, A. S. G., Driver, S. P., et al. 2016, MNRAS, 455, 4013

Dekel, A., & Birnboim, Y. 2006, MNRAS, 368, 2

den Hartog, R., & Katgert, P. 1996, MNRAS, 279, 349

DES Collaboration, Abbott, T., Aguena, M., et al. 2020, arXiv e-prints

Diaferio, A. 1999, MNRAS, 309, 610

Diaferio, A., & Geller, M. J. 1997, ApJ, 481, 633

Dickinson, M., Papovich, C., Ferguson, H. C., & Budavári, T. 2003, ApJ, 587, 25

Donahue, M., & Voit, G. M. 1999, ApJL, 523, L137

Dressler, A. 1980, ApJ, 236, 351

Drory, N., Bender, R., Feulner, G., et al. 2004, ApJ, 608, 742

Duarte, M., & Mamon, G. A. 2015, MNRAS, 453, 3848

Dünner, R., Araya, P. A., Meza, A., & Reisenegger, A. 2006, MNRAS, 366, 803

Durret, F., Adami, C., Cappi, A., et al. 2011, A&A, 535, A65

Eisenstein, D. J., Zehavi, I., Hogg, D. W., et al. 2005, ApJ, 633, 560

Eke, V. R., Cole, S., & Frenk, C. S. ????

Eke, V. R., Cole, S., Frenk, C. S., & Patrick Henry, J. 1998, MNRAS, 298, 1145

Elsner, F., Feulner, G., & Hopp, U. 2008, A&A, 477, 503

Erfanianfar, G., Finoguenov, A., Furnell, K., et al. 2019, A&A, 631, A175

Euclid Collaboration, Adam, R., Vannier, M., et al. 2019, A&A, 627, A23

Evrard, A. E., Bialek, J., Busha, M., et al. 2008, ApJ, 672, 122

Fadda, D., Girardi, M., Giuricin, G., Mardirossian, F., & Mezzetti, M. 1996, ApJ, 473, 670

Favole, G., Comparat, J., Prada, F., et al. 2016, MNRAS, 461, 3421

Foltz, R., Wilson, G., Muzzin, A., et al. 2018, ApJ, 866, 136

Gabor, J. M., Davé, R., Finlator, K., & Oppenheimer, B. D. 2010, MNRAS, 407, 749

Gardner, J. P., & JWST Science Working Group. 2009, in American Astronomical Society Meeting Abstracts, Vol. 213, American Astronomical Society Meeting Abstracts #213, 426.02

Geha, M., Blanton, M. R., Yan, R., & Tinker, J. L. 2012, ApJ, 757, 85

Genzel, R., & Cesarsky, C. J. 2000, ARA&A, 38, 761

Girardi, M., Borgani, S., Giuricin, G., Mardirossian, F., & Mezzetti, M. 1998a, ApJ, 506, 45

Girardi, M., Giuricin, G., Mardirossian, F., Mezzetti, M., & Boschin, W. 1998b, ApJ, 505, 74

Girardi, M., Manzato, P., Mezzetti, M., Giuricin, G., & Limboz, F. 2002, ApJ, 569, 720

Giuricin, G., Mardirossian, F., & Mezzetti, M. 1982, ApJ, 255, 361

Gladders, M. D., & Yee, H. K. C. 2005, ApJS, 157, 1

Golse, G., & Kneib, J.-P. 2002, A&A, 390, 821

Goto, T., Yamauchi, C., Fujita, Y., et al. 2003, MNRAS, 346, 601

Gunn, J. E., & Gott, III, J. R. 1972, ApJ, 176, 1

Guo, Q., White, S., Li, C., & Boylan-Kolchin, M. 2010, MNRAS, 404, 1111

Haiman, Z., Mohr, J. J., & Holder, G. P. 2001, ApJ, 553, 545

Hao, J., McKay, T. A., Koester, B. P., et al. 2010, ApJS, 191, 254

Hasselfield, M., Hilton, M., Marriage, T. A., et al. 2013, J. Cosmology Astropart. Phys., 2013, 008

Heisler, J., Tremaine, S., & Bahcall, J. N. 1985, ApJ, 298, 8

Henry, J. P., Evrard, A. E., Hoekstra, H., Babul, A., & Mahdavi, A. 2009, ApJ, 691, 1307

Hinshaw, G., Larson, D., Komatsu, E., et al. 2013, ApJS, 208, 19

Hogg, D. W., Bovy, J., & Lang, D. 2010, arXiv e-prints, arXiv:1008.4686

Hogg, D. W., Blanton, M. R., Brinchmann, J., et al. 2004, ApJL, 601, L29

Holhjem, K., Schirmer, M., & Dahle, H. 2009, A&A, 504, 1

Jackson, J. C. 1972, MNRAS, 156, 1P

Jenkins, A., Frenk, C. S., White, S. D. M., et al. 2001, MNRAS, 321, 372

Kaiser, N. 1987, MNRAS, 227, 1

Kauffmann, G., Colberg, J. M., Diaferio, A., & White, S. D. M. 1999, MNRAS, 303, 188

Kauffmann, G., Heckman, T. M., White, S. D. M., et al. 2003, MNRAS, 341, 33

Kelly, B. C. 2007, ApJ, 665, 1489

Kepner, J., Fan, X., Bahcall, N., et al. 1999, ApJ, 517, 78

King, I. R. 1972, ApJL, 174, L123

Kirby, M., Rozo, E., Morris, R. G., et al. 2019, arXiv e-prints, arXiv:1910.13548

Klypin, A., & Holtzman, J. 1997, ArXiv Astrophysics e-prints, astro-ph/9712217

Klypin, A., Yepes, G., Gottlöber, S., Prada, F., & Heß, S. 2016, MNRAS, 457, 4340

Klypin, A. A., Trujillo-Gomez, S., & Primack, J. 2011, ApJ, 740, 102

Knebe, A., Knollmann, S. R., Muldrew, S. I., et al. 2011, MNRAS, 415, 2293

Koester, B. P., McKay, T. A., Annis, J., et al. 2007, ApJ, 660, 239

Koranyi, D. M., & Geller, M. J. 2000, AJ, 119, 44

Kravtsov, A. V., Klypin, A. A., & Khokhlov, A. M. 1997, ApJS, 111, 73

Kubo, J. M., Stebbins, A., Annis, J., et al. 2007, ApJ, 671, 1466

Kubo, J. M., Annis, J., Hardin, F. M., et al. 2009, ApJL, 702, L110

Laganá, T. F., Zhang, Y.-Y., Reiprich, T. H., & Schneider, P. 2011, ApJ, 743, 13

Lau, E. T., Nagai, D., & Kravtsov, A. V. 2010, ApJ, 708, 1419

Leauthaud, A., Tinker, J., Bundy, K., et al. 2012, ApJ, 744, 159

Levi, M., Allen, L. E., Raichoor, A., et al. 2019, in BAAS, Vol. 51, 57

Lewis, A., Challinor, A., & Lasenby, A. 2000, ApJ, 538, 473

Lima, M., & Hu, W. 2007, Phys. Rev. D, 76, 123013

Limber, D. N., & Mathews, W. G. 1960, ApJ, 132, 286

Łokas, E. L., & Mamon, G. A. 2003, MNRAS, 343, 401

LSST Science Collaboration, Abell, P. A., Allison, J., et al. 2009, arXiv e-prints, arXiv:0912.0201 [astro-ph.IM]

Lukić, Z., Heitmann, K., Habib, S., Bashinsky, S., & Ricker, P. M. 2007, ApJ, 671, 1160

Majumdar, S., & Mohr, J. J. 2004, ApJ, 613, 41

Mamon, G. A., Biviano, A., & Boué, G. 2013, MNRAS, 429, 3079

Mamon, G. A., & Boué, G. 2010, MNRAS, 401, 2433

Manera, M., Sheth, R. K., & Scoccimarro, R. 2010, MNRAS, 402, 589

Mantz, A., Allen, S. W., Ebeling, H., & Rapetti, D. 2008, MNRAS, 387, 1179

Mantz, A. B. 2016, MNRAS, 457, 1279

Mantz, A. B., von der Linden, A., Allen, S. W., et al. 2015, MNRAS, 446, 2205

Mantz, A. B., Allen, S. W., Morris, R. G., et al. 2016, MNRAS, 463, 3582

Merloni, A., Predehl, P., Becker, W., et al. 2012, arXiv e-prints, arXiv:1209.3114

Merritt, D. 1988, in Astronomical Society of the Pacific Conference Series, Vol. 5, The Minnesota lectures on Clusters of Galaxies and Large-Scale Structure, ed. J. M. Dickey, 175

Metzler, C. A., White, M., Norman, M., & Loken, C. 1999, ApJL, 520, L9

Milkeraitis, M., van Waerbeke, L., Heymans, C., et al. 2010, MNRAS, 406, 673

Miller, C. J., Nichol, R. C., Reichart, D., et al. 2005, AJ, 130, 968

Muñoz-Cuartas, J. C., Macciò, A. V., Gottlöber, S., & Dutton, A. A. 2011, MNRAS, 411, 584

Mulroy, S. L., Farahi, A., Evrard, A. E., et al. 2019, MNRAS, 484, 60

Munari, E., Biviano, A., Borgani, S., Murante, G., & Fabjan, D. 2013, MNRAS, 430, 2638

Murray, S. G., Power, C., & Robotham, A. S. G. 2013a, Astronomy and Computing, 3, 23

—. 2013b, MNRAS, 434, L61

Muzzin, A., Wilson, G., Demarco, R., et al. 2013, ApJ, 767, 39

Muzzin, A., Wilson, G., Yee, H. K. C., et al. 2009, ApJ, 698, 1934

Nagamine, K., & Loeb, A. 2003, NewA, 8, 439

Navarro, J. F., Frenk, C. S., & White, S. D. M. 1996, ApJ, 462, 563

—. 1997, ApJ, 490, 493

Nelson, D., Springel, V., Pillepich, A., et al. 2018, arXiv e-prints, arXiv:1812.05609

Noble, A. G., Webb, T. M. A., Muzzin, A., et al. 2013, ApJ, 768, 118

Ntampaka, M., Rines, K., & Trac, H. 2019, ApJ, 880, 154

Ntampaka, M., Trac, H., Cisewski, J., & Price, L. C. 2017, ApJ, 835, 106

Old, L., Gray, M. E., & Pearce, F. R. 2013, MNRAS, 434, 2606

Old, L., Skibba, R. A., Pearce, F. R., et al. 2014, MNRAS, 441, 1513

Old, L., Wojtak, R., Mamon, G. A., et al. 2015, MNRAS, 449, 1897

Old, L., Wojtak, R., Pearce, F. R., et al. 2018, MNRAS, 475, 853

Pacaud, F., Pierre, M., Melin, J. B., et al. 2018, A&A, 620, A10

Pacucci, F., Mesinger, A., & Haiman, Z. 2013, MNRAS, 435, L53

Pearson, D. W., Batiste, M., & Batuski, D. J. 2014, MNRAS, 441, 1601

Perea, J., del Olmo, A., & Moles, M. 1990a, A&A, 237, 319

—. 1990b, Ap&SS, 170, 347

Pereira, S., Campusano, L. E., Hitschfeld-Kahler, N., et al. 2017, ApJ, 838, 109

Perlmutter, S., Aldering, G., Goldhaber, G., et al. 1999, ApJ, 517, 565

Pisani, A. 1993, MNRAS, 265, 706

—. 1996, MNRAS, 278, 697

Planck Collaboration, Ade, P. A. R., Aghanim, N., et al. 2011, A&A, 536, A1

—. 2014, A&A, 571, A1

—. 2016, A&A, 594, A13

Planck Collaboration, Aghanim, N., Akrami, Y., et al. 2018, arXiv e-prints, arXiv:1807.06209

Pointecouteau, E., Arnaud, M., & Pratt, G. W. 2005, A&A, 435, 1

Postman, M., Huchra, J. P., & Geller, M. J. 1992, ApJ, 384, 404

Praton, E. A., & Abdullah, M. 2014, in American Astronomical Society Meeting Abstracts, Vol. 223, American Astronomical Society Meeting Abstracts #223, 457.14

Praton, E. A., & Schneider, S. E. 1994, ApJ, 422, 46

Pratt, G. W., Croston, J. H., Arnaud, M., & Böhringer, H. 2009, A&A, 498, 361

Press, W. H., & Davis, M. 1982, ApJ, 259, 449

Press, W. H., & Schechter, P. 1974, ApJ, 187, 425

Raichoor, A., Comparat, J., Delubac, T., et al. 2017, MNRAS, 471, 3955

Ramella, M., Boschin, W., Fadda, D., & Nonino, M. 2001, A&A, 368, 776

Regos, E., & Geller, M. J. 1989, AJ, 98, 755

Reichardt, C. L., Stalder, B., Bleem, L. E., et al. 2013, ApJ, 763, 127

Reiprich, T. H., & Böhringer, H. 2002, ApJ, 567, 716

Reisenegger, A., Quintana, H., Carrasco, E. R., & Maze, J. 2000, AJ, 120, 523

Riebe, K., Partl, A. M., Enke, H., et al. 2013, Astronomische Nachrichten, 334, 691

Rines, K., & Diaferio, A. 2006, AJ, 132, 1275

Rines, K., Diaferio, A., & Natarajan, P. 2007, ApJ, 657, 183

Rines, K., Geller, M. J., & Diaferio, A. 2010, ApJL, 715, L180

Rines, K., Geller, M. J., Kurtz, M. J., & Diaferio, A. 2003, AJ, 126, 2152

Rines, K. J., Geller, M. J., Diaferio, A., & Hwang, H. S. 2016, ApJ, 819, 63

Ross, A. J., Samushia, L., Howlett, C., et al. 2015, MNRAS, 449, 835

Rozo, E., Wechsler, R. H., Rykoff, E. S., et al. 2010, ApJ, 708, 645

Rudd, D. H., Zentner, A. R., & Kravtsov, A. V. 2008, ApJ, 672, 19

Ruel, J., Bazin, G., Bayliss, M., et al. 2014, ApJ, 792, 45

Rykoff, E. S., Rozo, E., Busha, M. T., et al. 2014, ApJ, 785, 104

Rykoff, E. S., Rozo, E., Hollowood, D., et al. 2016, ApJS, 224, 1

Sarazin, C. L. 1988, X-ray emission from clusters of galaxies

Saro, A., Mohr, J. J., Bazin, G., & Dolag, K. 2013, ApJ, 772, 47

Schellenberger, G., & Reiprich, T. H. 2017, MNRAS, 471, 1370

Schlegel, D. J., Finkbeiner, D. P., & Davis, M. 1998, ApJ, 500, 525

Schmidt, M. 1968, ApJ, 151, 393

Schneider, A., Smith, R. E., & Reed, D. 2013, MNRAS, 433, 1573

Schuecker, P., Böhringer, H., Collins, C. A., & Guzzo, L. 2003, A&A, 398, 867

Scolnic, D. M., Jones, D. O., Rest, A., et al. 2018, ApJ, 859, 101

Sereno, M., & Ettori, S. 2015, MNRAS, 450, 3633

Sereno, M., & Zitrin, A. 2012, MNRAS, 419, 3280

Serra, A. L., & Diaferio, A. 2013, ApJ, 768, 116

Serra, A. L., Diaferio, A., Murante, G., & Borgani, S. 2011, MNRAS, 412, 800

Sheth, R. K., Mo, H. J., & Tormen, G. 2001, MNRAS, 323, 1

Sheth, R. K., & Tormen, G. 2002, MNRAS, 329, 61

Shimazaki, H., & Shinomoto, S. 2010, Journal of Computational Neuroscience, 29, 171

Sifón, C., Hoekstra, H., Cacciato, M., et al. 2015, A&A, 575, A48

Silverman, B. W. 1986, Density estimation for statistics and data analysis

Simet, M., McClintock, T., Mandelbaum, R., et al. 2017, MNRAS, 466, 3103

Skibba, R., Sheth, R. K., Connolly, A. J., & Scranton, R. 2006, MNRAS, 369, 68

Skibba, R. A., & Sheth, R. K. 2009, MNRAS, 392, 1080

Soares-Santos, M., de Carvalho, R. R., Annis, J., et al. 2011, ApJ, 727, 45

Somerville, R. S., & Davé, R. 2015, ARA&A, 53, 51

Springel, V. 2005, MNRAS, 364, 1105

Sunyaev, R. A., & Zeldovich, Y. B. 1972, A&A, 20, 189

Takey, A., Durret, F., Márquez, I., et al. 2019, MNRAS, 486, 4863

Tempel, E., Kruuse, M., Kipper, R., et al. 2018, A&A, 618, A81

Tempel, E., Tamm, A., Gramann, M., et al. 2014, A&A, 566, A1

The, L. S., & White, S. D. M. 1986, AJ, 92, 1248

Tinker, J., Kravtsov, A. V., Klypin, A., et al. 2008, ApJ, 688, 709

Tinker, J. L., & Wetzel, A. R. 2010, ApJ, 719, 88

Tonry, J. L., & Davis, M. 1981, ApJ, 246, 680

Turner, E. L., & Gott, III, J. R. 1976, ApJS, 32, 409

van Haarlem, M., & van de Weygaert, R. 1993, ApJ, 418, 544

van Uitert, E., Joachimi, B., Joudaki, S., et al. 2018, MNRAS, 476, 4662

Velliscig, M., van Daalen, M. P., Schaye, J., et al. 2014, MNRAS, 442, 2641

Viana, P. T. P., & Liddle, A. R. 1996, MNRAS, 281, 323

Viana, P. T. P., Nichol, R. C., & Liddle, A. R. 2002, ApJL, 569, L75

Vikhlinin, A., Burenin, R. A., Ebeling, H., et al. 2009a, ApJ, 692, 1033

Vikhlinin, A., Kravtsov, A. V., Burenin, R. A., et al. 2009b, ApJ, 692, 1060

Wang, L., & Steinhardt, P. J. 1998, ApJ, 508, 483

Warren, M. S., Abazajian, K., Holz, D. E., & Teodoro, L. 2006, ApJ, 646, 881

Watson, W. A., Iliev, I. T., D'Aloisio, A., et al. 2013, MNRAS, 433, 1230

Wechsler, R. H., & Tinker, J. L. 2018, ARA&A, 56, 435

Wen, Z. L., Han, J. L., & Liu, F. S. 2009, ApJS, 183, 197

—. 2010a, ApJS, 187, 272

—. 2010b, MNRAS, 407, 533

—. 2012, ApJS, 199, 34

White, S. D. M., & Frenk, C. S. 1991, ApJ, 379, 52

Wilson, G., Cole, S., & Frenk, C. S. 1996, MNRAS, 280, 199

Wilson, G., Muzzin, A., Yee, H. K. C., et al. 2009, ApJ, 698, 1943

Wojtak, R., & Łokas, E. L. 2007, MNRAS, 377, 843

—. 2010, MNRAS, 408, 2442

Wojtak, R., Old, L., Mamon, G. A., et al. 2018, MNRAS, 481, 324

Wu, H.-Y., Hahn, O., Evrard, A. E., Wechsler, R. H., & Dolag, K. 2013, MNRAS, 436, 460

Wylezalek, D., Vernet, J., De Breuck, C., et al. 2014, ApJ, 786, 17

Yahil, A. 1985, in European Southern Observatory Conference and Workshop Proceedings, Vol. 20, European Southern Observatory Conference and Workshop Proceedings, 359

Yahil, A., & Vidal, N. V. 1977, ApJ, 214, 347

Yang, X., Mo, H. J., van den Bosch, F. C., & Jing, Y. P. 2005, MNRAS, 356, 1293

Yang, X., Mo, H. J., van den Bosch, F. C., et al. 2007, ApJ, 671, 153

Yee, H. K. C., & Ellingson, E. 2003, ApJ, 585, 215

Yoon, J. H., Schawinski, K., Sheen, Y.-K., Ree, C. H., & Yi, S. K. 2008, ApJS, 176, 414

Zabludoff, A. I., Huchra, J. P., & Geller, M. J. 1990, ApJS, 74, 1

Zenteno, A., Mohr, J. J., Desai, S., et al. 2016, MNRAS, 462, 830

Zhang, Y., Jeltema, T., Hollowood, D. L., et al. 2019, arXiv e-prints, arXiv:1901.07119

Zubeldia, Í., & Challinor, A. 2019, MNRAS, 489, 401